Nanomechanical Fracture Testing of Diatoms

Ole Martin Heggem

Task Description

THE NORWEGIAN UNIVERSITY
OF SCIENCE AND TECHNOLOGY
DEPARTMENT OF ENGINEERING DESIGN
AND MATERIALS

MASTER THESIS SPRING 2015
FOR
STUD.TECHN. OLE MARTIN HEGGEM

Nanomechanical Fracture Testing of Diatoms

Nanomekanisk brudd testing diatomer

Diatom is the name of a large group of unicellular algae, which gets their name from the structure of the cell wall. The diatoms make an exoskeleton of silica which consists of two separated valves connected by one or several girdle bands. The diameter of the diatom Coscinodiscussp., the diatom to be focused in this work, is about 200-400 µm, which makes it one of the largest diatom species.
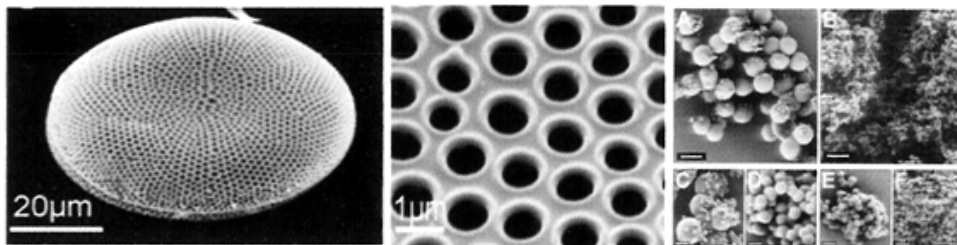

Figure: Diatoms are characterized by regular patterns of voids in a matrix of biosilica. The figure to the right shows the spherical shape of the biosilica.

In spite of increased interest there are rather few experimental data for the mechanical properties of diatom frustules.

In previous tests by Hamm et al [2003] the whole diatom was tested by a glass micro needle to load and break the frustules. Three species were tested and the stress at fracture and modulus of elasticity (E) were calculated by finite element calculations of the species *F. kerguelensis*. The results revealed a low E and high fracture stress compared with fused silica. By loading the FE-model of the girdle band under an assumed Young's modulus, deformation as a function of force could be calculated, and the Young's modulus modified until the test and simulation yielded identical results. With this approach, they determined Young's modulus to be 22.4 GPa. The same procedure was applied to determine the strength resulting in an ultimate strength at about 540 MPa. They also noted the apparent lack of plastic deformation, indicating that diatom bio-silica is a brittle material, in accordance with the sharp-edged and smooth fracture surfaces found in broken frustules.

In order to confirm the above results, and further explore the unique properties of bio-silica, three point bend tests and cantilever beam tests have been performed. Rectangular three point bend specimens were machined from the whole cell wall with FIB, and in addition we also fabricated test specimens from the foramen inner layer of the capsule. In this way we have been able to quantify the mechanical properties of the pure biosilica material. We find that the biosilica is very strong and flexible. The inner layer has a modulus of elasticity of about 35 GPa and fracture strength of more than 2500 MPa.

The goal with the present Thesis is to determine the fracture toughness of the biosilica.

The following tasks shall be performed

1. Present the diatoms and the mechanical properties of the frustule.
2. Determine the fracture toughness of the foramen layer of Cosinodiscus. The testing procedure includes collecting and preparing diatoms, FIB machining and subsequent testing in nanomechanical lab.
3. Detailed examination of the fracture surface in the SEM and AFM
4. FE models might be necessary in order to account for the specimen geometry

Formal requirements:

Three weeks after start of the thesis work, an A3 sheet illustrating the work is to be handed in. A template for this presentation is available on the IPM's web site under the menu "Masteroppgave" (http://www.ntnu.no/ipm/masteroppgave). This sheet should be updated one week before the master's thesis is submitted.

Risk assessment of experimental activities shall always be performed. Experimental work defined in the problem description shall be planed and risk assessed up-front and within 3 weeks after receiving the problem text. Any specific experimental activities which are not properly covered by the general risk assessment shall be particularly assessed before performing the experimental work. Risk assessments should be signed by the supervisor and copies shall be included in the appendix of the thesis.

The thesis should include the signed problem text, and be written as a research report with summary both in English and Norwegian, conclusion, literature references, table of contents, etc. During preparation of the text, the candidate should make efforts to create a well arranged and well written report. To ease the evaluation of the thesis, it is important to cross-reference text, tables and figures. For evaluation of the work a thorough discussion of results is appreciated.

The thesis shall be submitted electronically via DAIM, NTNU's system for Digital Archiving and Submission of Master's theses.

Torgeir Welo
Head of Division

Christian Thaulow
Professor/Supervisor

NTNU
Norges teknisk-
naturvitenskapelige universitet
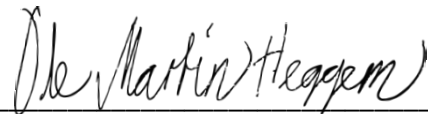Institutt for produktutvikling
og materialer

Preface

This thesis was written as the final requirement for the completion of my Master of Technology education in Mechanical Engineering at the Norwegian University of Science and Technology (NTNU).

Several people have helped my during the thesis work, all of which I am grateful to for their assistance and input.

I would like to thank my supervisor, Professor Christopher Thaulow for introducing me to the diatoms, enabling me to learn even more about materials in general and biosilica in particular. The encouragement and guidance provided were also much needed, especially in times of crisis.

I would also like to thank Anette Brocks Hagen and especially PhD Bjørn Rune Sørås Rogne for assistance and guidance with the scientific instruments. Without their commitment and knowledge, the experiments would be even more time consuming and challenging than they already were.

Last, but not least, I would like to thank my friends and family for supporting me through all this time and giving me advice and help when I needed it most. Additional thanks goes to Thomas Heggem, who enabled this thesis to have illustrations which were not terrible.

Ole Martin Heggem
Trondheim, June 2015

Abstract

Diatoms, a major group of algae, create a silica shell around them to protect themselves against the environment in which they live. While these shells, termed frustules, on a first glance may appear relative unsophisticated, the truth is anything but. Consisting of multiple layers and with different structural properties, the frustule serves as both a mechanical and bacterial protection, while enhancing the diatoms' light harvesting abilities. Bulk silica is normally very brittle, but the diatom material is surprisingly though. Fracture mechanic testing has therefore been performed in order to see if this toughness extends to the resistance to crack growth. A theoretical study of the mechanical properties of the frustule has also been performed.

A way to test the fracture properties of the foramen layer has been developed and tested. Cantilevers made out of the diatom silica were produced with the Focused Ion Beam (FIB). These had notches milled close to the base of the cantilever and were then loaded to fracture using a picoindenter. Challenges and issues during testing have also been discussed in order to assist in any experiments that may continue the described diatom testing.

Unfortunately, only one cantilever yielded usable results. Finite element models were created in order to analyse the result, as well as conventional fracture toughness formulas. However, the cantilever had been sloped upwards during the production because of internal stresses, which had to be taken into account. Two models were made: one of which was based on no internal stresses while the other was based on the internal stresses being nullified when the cantilever was horizontal. These two models resulted in a conservative estimate and an over-idealised estimate of the fracture toughness and thus yielded inconclusive results. The real value should be somewhere between the two extremes, whose values ended up at 0,31 MPa√m and 2,03 MPa√m.

A dimensionless geometry factor for the optimal cantilever shape was also obtained. This was shown to be considerably lower than the values from theory, much due to the smaller vertical sides of the pentagonal cross section.

Sammendrag

Diatomer eller kiselalger danner et eksoskjelett av silisiumdioksid rundt dem som beskyttelse mot miljøet de lever i. Disse skallene, kalt "frustuler" ser relativt usofistikerte ut, spesielt når man ser de ved lave forstørrelsesgrader, men sannheten er en helt annen. Skallene består av flere lag med forskjellige egenskaper og utgjør både mekanisk og bakteriell beskyttelse, samt hjelper diatomene med å absorbere lys. Silisiumdioksid er vanligvis veldig sprøtt, men materialet dannet av diatomene er overraskende sterkt. Bruddmekanisk testing har derfor blitt gjennomført for å se om disse egenskapene også inkluderer motstand mot sprekkvekst. En teoretisk studie av de mekaniske egenskapene har også blitt gjennomført.

En testmetode for å bestemme bruddstyrken til "foramen"-laget har blitt utviklet og testet. Utkragerbjelker lagd av silisiumdioksidet ble produsert ved hjelp av fokusert ionestråling (FIB). Disse ble laget med hakk plassert nærme den innspente enden og ble lastet til brudd ved hjelp av en picoindenter. Utfordringer og problemer som oppstod underveis har også blitt drøftet for å hjelpe med eventuelle arbeid som bygger videre på testingen.

Kun en utkragerbjelke ga brukbare resultater. FEM-modeller ble dannet for å analysere resultatene, i tillegg til at rene utregninger ble foretatt. På grunn indre spenninger, ble denne bjelken bøyd oppover under produksjonsfasen, noe som måtte tas hensyn til under beregningene og modelleringen. To modeller ble derfor laget; en hvor hele lasttesten ble analysert og en hvor de indre spenningene hadde blitt utjevnet, det vil si når bjelken var nedbøyd til den var horisontal. Dette resulterte i en konservativ verdi og en overidealisert verdi, noe som betydde at man ikke kunne dra en endelig konklusjon. Den virkelige størrelsen for bruddstyrken skal dermed være et sted mellom disse to ekstremtilfellene, som ga tallverdiene 0,31 MPa√m og 2,03 MPa√m.

En dimensjonsløs geometrifaktor for den optimale bjelkeutformingen ble også beregnet. Denne ble vist til å være betydelig lavere enn de fra tidligere undersøkelser, mye på grunn av at de vertikale sidene i femkanttverrsnittet er kortere

Nomenclature

a	Crack/notch depth
d	Diameter, spot size
E	Young's modulus
F	Force
f(a/b	Dimensionless geometry factor
H	Distance between the notch and the base of the cantilever
h	Height of the vertical sides of the cantilever
h_{tot}	Height of the vertical sides of the cantilever
I	Current, moment of inertia
J	J-integral
K	Stress intensity factor
K_C	Fracture toughness
K_J	Stress intensity factor/fracture toughness calculated from the J-integral
K_Q	Provisional fracture toughness
L	Loading distance
v	Poisson's ratio
R	Rotational angle
σ	Stress
T	Temperature, tilt angle
u	Deflection
V	Acceleration voltage
w	Width of the cantilever
y	Distance between the neutral plane and a chosen surface

Contents

List of figures

List of tables

1   Introduction

Material properties have always fascinated mankind. In ancient times, timbers were tested to the limits when building ships and smiths always ran the risk of destroying their creations when the metal was tempered.

In newer times, this has been transferred to more technologically advanced structures and while the materials used may not break in the cooling process, they have a whole range of other issues that work against them. One of these problems includes small imperfections, which given enough time strain, will result in larger problems with possible catastrophic consequences. Fortunately, there exist experts who prevent this from happening and can find other solutions when the existing ones no longer are adequate. However, this often results in the need of seemingly impossible materials, especially when there is a need of strong materials that are both lightweight and resistant to imperfections. Maybe the solution is to not reinvent a new class of material, but to look back at what we currently have available?

The oldest recorded diatom fossil dates back 180 million years. Today, diatoms are one of the largest groups of algae and are one of the most common type of phytoplankton.[1] These can be found in nearly all waters, from oceans to freshwater lakes, from low to high temperatures and at locations with different acidity. Diatoms especially play an important role in the oceans since they fix large amount of carbon dioxide and synthesize carbohydrates that serve as food in the marine food chain. In fact, it is believed that the diatoms are responsible for up to 25 % of the world's net primary production of organic carbon while consuming 20 % of the global CO_2 in the process.[2, 3]

Currently, the diatom silica cannot be used in construction due to the small size of algae. If the material could be utilized in a larger scale, it would help tremendously with finding solutions to existing material problems. The material, while low in weight, boast tremendous mechanical properties. Nature has already provided the diatoms with efficient ways to deal with most problems, but how the material withstands fracture is currently unknown.

2 Theory

In this section the theory regarding the diatoms will be explored. The first part starts with an introduction to the diatom species focused on in this work, with following information concerning the hierarchal structure of the frustule. The formation of the frustule is also explored. The next parts concern the scientific instruments that may be applied when studying the algae and previous mechanical experiments of the material. A comparison between the mechanical properties from the various tests has also been made. The next sections contain information about fracture mechanic testing and -parameters and how the cantilevers can be produced. Lastly, fracture toughness values of similar materials are presented. The information regarding the experimental equipment, the diatom structure and the mechanical properties of the diatom has been adapted from the project work leading up to this thesis, with new information added where relevant.[4]

2.1 Coscinodiscus sp.

2.1.1 Diatom composition and properties

With a few exceptions, all diatoms have characteristic perforated and ornamented silica cell walls, called frustules. These walls protect and constrain the protoplast, but must also provide means for nutrition uptake and exchange of gasses and other cellular products.[5] The frustule can be divided into valves and girdle bands. The valves, commonly described as having a Petri dish design, are being held in place by the girdle bands which surround the diatom. This is also the reason for the name diatom, as it comes from the Greek words *dia* and *temnein*, meaning "to cut", which is a reference to the two halves of its shell. The girdle bands consist of multiple overlapping bands that may be entire, split or overlapping, and are flexible enough to allow the cell to expand in the direction normal to the valve plane. Other than that, the valves can vary with regards to pores, straightness, composition, etc..

Based on the shape of the frustule, diatoms have been subdivided into two major groups; the *centrales* for radial symmetrical frustules and the *pennales* for bilateral symmetrical frustules.[6] In the latter group, one can find the diatom Coscinodiscus sp. (sp, indicates that the exact species is unknown). This diatom, with its diameter of 200-400 μm, is one of the largest diatom species and is the one to be focused on in this work.

2.1.2 The frustule

In 2007, Losic et al. studied a Coscinodiscus with an atomic force microscope (AFM) in order to collect more information on the topography of the diatoms, with focus on the frustule.[7] In general, while the frustule being vastly different in shape from species to species, always consists of individual layers with different structures. For the Coscinodiscus, the valves consist of four layers; the cribellum, the cribrum, the areola and the foramen. These layers are illustrated in Figure 2.1. In addition to saving weight, layered structures have a very good stiffness to bending, especially if they have layers that work in different directions, for example like the structural I-beam. Given the diatom's shape, bending stresses are the main result from applied loads and thus the logical response would be to develop bending resistance.

Due to being an unknown species, the exact dimensions listed in this section will probably be different from the ones on the diatoms used in this project work, but the layers and their composition should be the same.
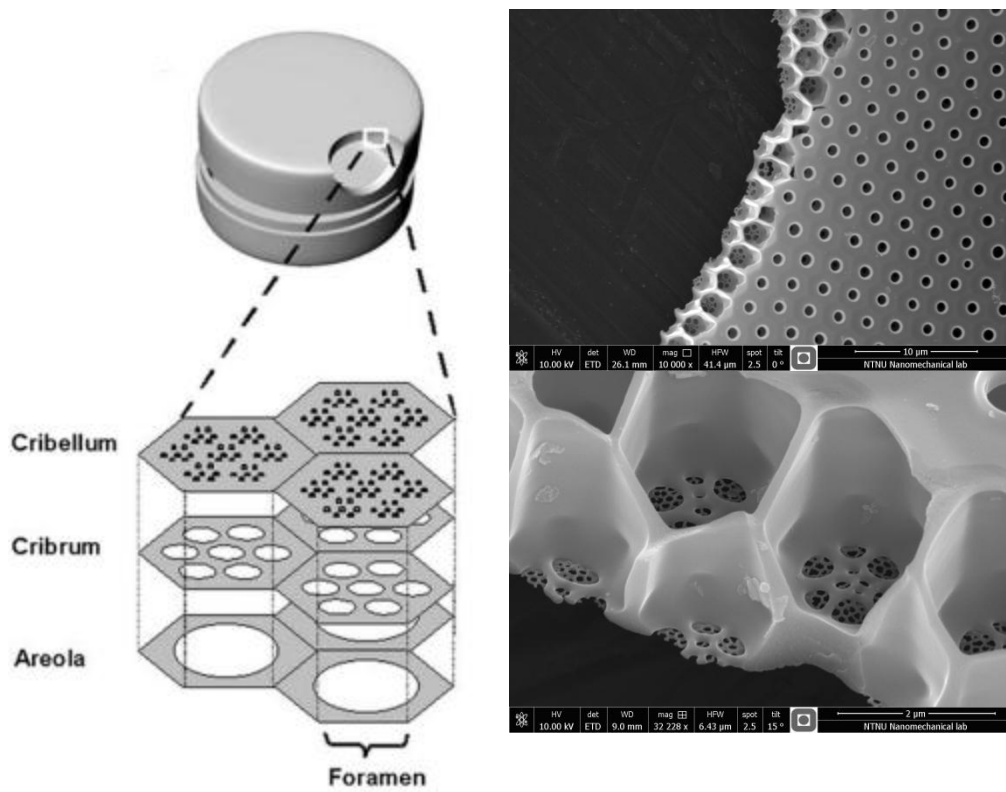
Figure 2.1:
To the left: Composition of the frustule. Illustration is taken from Losic, D., et al., _Atomic force microscopy (AFM)_ _characterisation of the porous silica nanostructure of two centric diatoms_.[7]
To the right: Top picture displays the different layers as seen in an ESEM, while the bottom picture is more zoomed in and provides more detail. Note that the foramen is facing upwards.

The outer layer, the cribellum, was found to consist of very fine pores arranged in a hexagonal manner. The layer was very thin, less than 50 nm in thickness, and the pores had a diameter of about 45 nm. It is believed that the layer is not there for structural reasons, as it is weakly connected to the rest of the frustule, but rather offered protection against virus and bacteria by letting nutrition go through the pores while keeping the bacteria out. It was also observed that this layer contained some organic material

The next layer, the cribrum, was observed to consist of larger pores with a diameter of around 190 nm, arranged in clusters resembling flowers when seen from above. These clusters were also arranged in a hexagonal manner, with each one overlaying the pattern in the next layer. The layer itself was found to be around 200 nm.

The third layer, the areola, was reported to be the main structural component, with thickness ranging from 2-2,5 µm. This layer consists of the classic honeycomb structure, with a wall thickness and honeycomb corner-to-corner distance of 300-400 nm and 2-3 µm, respectively.

Lastly, the frustule is completed by the final layer, the foramen. This layer was found to have a thickness of 360 nm and be covered by lipped holes with a diameter of 1150 nm.[7]

2.1.3 Reproduction

Diatoms in general have a curios life cycle. For months or even years, they create inorganic structures when their cells divide mitotically. This process, when living organisms create inorganic materials, is called biomineralisation and is quite widespread in nature.

For diatoms, this is done in accordance with Figure 2.2. The cell expands in the axial direction (normal to the valves) with additional girdle bands being produced to accommodate the larger volume, as well as to protect the protoplast during the operation. When reaching a desired distance, the cell splits into two entities and start producing new silica walls. The production of silica is performed by a specialised vesicle called the silica deposition vesicle (SDV) which is formed within each cell. The girdle bands are also produced in their own individual vesicles.[1, 8] The SDVs become larger in order to deposit more and more silica until finally the cells are ready to separate.
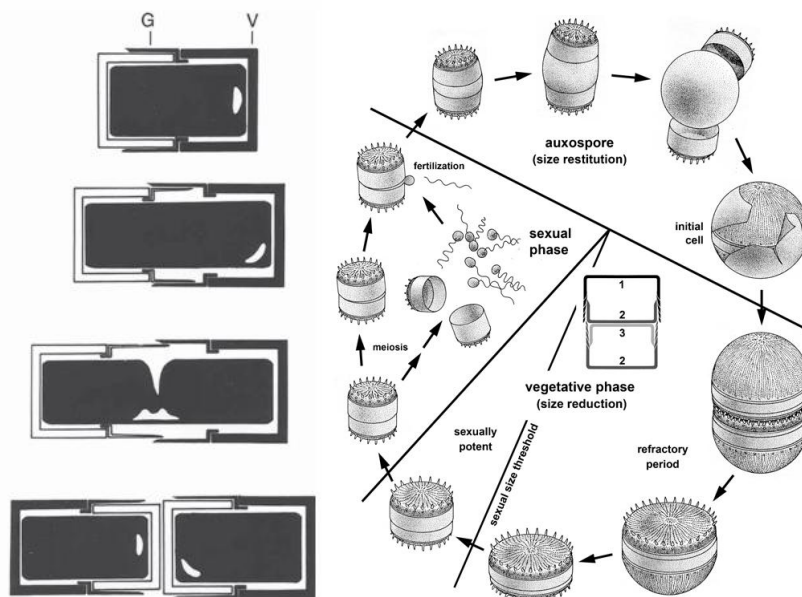
Figure 2.2:
To the left: Cell division in a centric diatom. The "G" and "V" represent the girdle band and one of the valves, respectively. The figure is taken from Gebeshuber, I.C. and R.M. Crawford, *Micromechanics in biogenic hydrated silica: Hinges and interlocking devices in diatoms.***[8]**
To the right: The life cycle of a diatom. The figure is taken from Mann, D., *Size and Sex***, in** *The Diatom World***.[9]**

However, when creating these new shells, the size of one of the resulting cells will be smaller than the mother cell, because the valves are formed within the parent's frustule. After multiple "generations" of mitotic division, the diatoms reach a critical size. At this point, instead of continuing to make smaller and smaller cells, the diatom will create sexual active cells when the environmental circumstances are correct and meiosis will occur. Thus, the resulting *auxospore* will expand until it reaches the characteristic size for its diatom species, and will then form an initial cell. This repeating process is illustrated in Figure 2.2. [9]

2.1.4 **Nanoparticles and chemical composition**

Silicic acid is believed to be the primary source of the diatom's silica since it is found in the natural habitat of the diatoms, but the process of how this is turned into the advanced frustule structures is currently unknown. For many years, the construction of the frustule was a mystery, but in 1965 it was found by Reimann et al. that organic material tightly surrounded every part of the frustule.[10] Four years later, Volcani and Nakajima, discovered that the frustule contained different organic components, indicating that biosilica could be a composite material.[11] Hecky et al. suggested that proteins in the cell walls were used as a template for the condensation of silicic acid in order to deposit biosilica.[12] The proteins, termed silaffins, are a family of polypeptides bound to long-chain polyamines. Kröger et al. found that the isolated silaffins were able to create silica nanospheres within seconds when exposed to a solution of silicic acid. It was also noted that the distribution of lysine amino acid in the peptides had a high influence on the silica-precipitating activity of the silaffins.[13] The polyamines on the other hand, were found to control the silica morphology. The structure of the polyamines differenced from species to species, but was found to induce rapid precipitation of biosilica when added to monosilicic acid, and also capable of controlling silica sphere size *in vitro*.[14] Because of these abilities, it is theorised that the combined action of silaffins and polyamines result in the species-specific basilica pattern of the diatoms.

The first discovery of nanospheres was done by Schmid in 1976. Additional tests done in 1978 and 1979 confirmed the initial observations. During valve development examinations, there were observed a structural difference between a younger zone and that of the finished wall. In the younger zone, small silica spheres as small as 12-30 nm were observed using transmission electron microscope (TEM) and SEM.[15]

In 2001, Crawford and Higgins used an AFM to sweep away the mucilage covering the outer surface of the diatoms *Pinnularia viridis* and *Hantzschia amphioxys*, enabling high resolution scanning of the surface without any acid treatments. The diatoms were also cleaved and the resulting cross section surfaces were scanned by both SEM and AFM. The frustule surface was found to have a granular appearance, in stark contrast to the smooth surfaces one usually observe when the diatoms had been chemically treated. The AFM study of the cross sections resulted in observations of nanoparticles, which was noted to be packed somewhat loosely, giving the material a porous structure. The size of the spheres varied slightly between the girdle band and the valve, having diameters of about 40 and 45 nm for the *Pinnularia viridis* and 38 and 37 nm for the *Hantzschia amphioxys*.[16]

Losic et al. [7] also witnessed nanoparticles in his AFM study of the diatom *Thalassiosira eccentrica*, but these varied in size, ranging from 20 to 70 nm and arranged in nodules. These diatoms were subjected to cleaning and removal of organic matter by various acids. Only the top and bottom layer were examined, with the results from outer layer illustrated in Figure 2.3.

The results from the various tests indicate that the chemical treatments will make it more difficult to view the real surface of the diatoms, especially with regards to the nanosphere structure. It is also believed that the nanospheres may vary in size between the frustule components, with more significant differences between species.
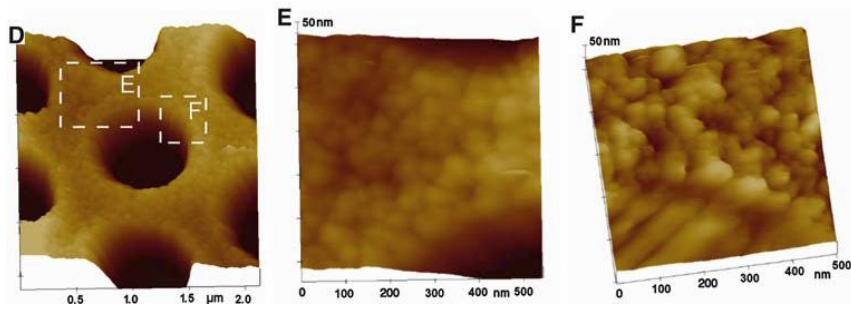
Figure 2.3: Tapping mode AFM imaging of ridge surfaces revealed the granular structure of the foramen. Figure is taken from Losic, D., et al., *Atomic force microscopy (AFM) characterisation of the porous silica nanostructure of two centric diatoms.*[7]

2.2 Equipment

2.2.1 Atomic force microscopy

When two solid surfaces approach one another, they exert both attractive and repulsive forces between them. These forces operate in three different interaction zones, namely the non-contact region, the intermittent contact region and the contact region. The potential energy difference in the different zones varies with the distance between the surfaces, as seen in Figure 2.4.
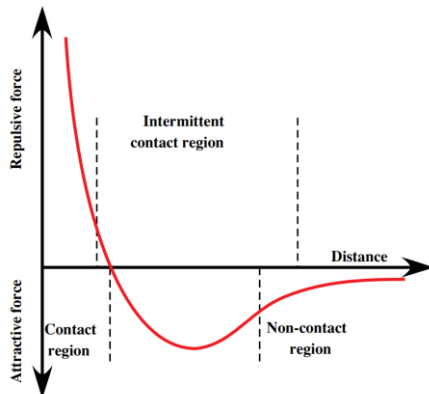
Figure 2.4: Potential energy curve for the interaction of two solid surfaces with corresponding interaction zones. Illustration is taken from Brandon, D. and W.D. Kaplan, *Microstructural Characterization of Materials*.[17]

In the non-contact region, Coulomb electrostatic forces dominate the interaction. These forces may either be repulsive or attractive, depending on the charge of the two surfaces being of the same or opposite sign. At shorter distances, polarisation or van der Waals forces are experienced. These include local electric field polarisations induced by molecular dipole moments, Debye interactions and localized attractive forces between neighbouring polarisable atoms. These forces decay rapidly, usually as d^{-7}.[17] The strong, short-range and repulsive forces between atoms are caused by the electron shells interfering with those of the atoms on the other surface.

The interactions will also be affected by the medium between the two surfaces, as well as the surface roughness and local curvature. For instance, at around 1 nm separation, a truncated cone exhibits roughly one order of magnitude larger force when compared to a rounded tip end. For an ideally sharp cone, the force is two magnitudes smaller.[18] . It is therefore imperative that instruments which measure surface forces, like atomic force microscopy, don't have the measurement tip deformed during testing.

Atomic force microscopy

Atomic force microscopy (AFM) is a method used to view the shape of a surface in three-dimensional details down to the nanoscale. AFM can image all materials and does not need vacuum to operate, although it is capable of doing so, but can image objects in air or in liquid environments.[18]

Unlike conventional microscopes, the AFM employs local measurement of the height of the specimen. This is done by the use of a sharp probe situated at the end of a micro-cantilever. By either moving the sample stage or the cantilever itself, the cantilever probe can be brought in close proximity to the sample, where it will interact with the surface forces, causing the cantilever to bend. By reflecting a laser off the cantilever surface and measuring the movement of the deflected laser

spot with a position-sensitive detector, the movement can be indirectly measured. This detector consists of an array of photodiodes which will measure the deflections based on both bending and torsion. The principle is illustrated in Figure 2.5.
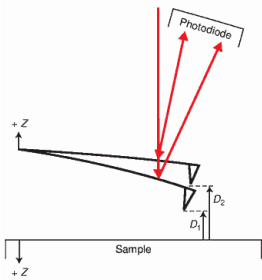
Figure 2.5: Deflection of the laser on the cantilever. The figure is taken from Haugstad, G., *Atomic Force Microscopy.*[18]

The laser deflection is however only dependent of the change in the angle of inclination near the tip and not the vertical tip displacement in itself, but that can be measured using the pre-calibrated Z-scanner. Said scanner, as well as the X- and Y-scanners which governs the specimen plane, is part of a set of piezoelectric crystals which regulates the movement of the cantilever (or in some cases, the sample stage). As the name suggests, these crystals have piezoelectric properties, which enables them to expand or contract when subjected to electric voltage and can are very accurate. A general layout of an AFM in contact mode is seen in Figure 2.6.
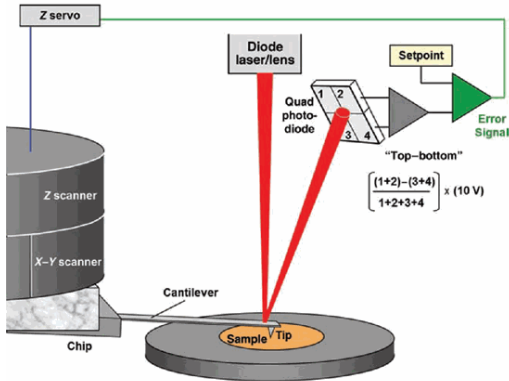
Figure 2.6: Schematic of an AFM. The bracketed number represents the feedback signal. Illustration is taken from Haugstad, G., *Atomic Force Microscopy.*[18]

There are two main ways to analyse a specimen in AFM; contact mode and tapping mode. In contact mode, the tip is kept very close to the specimen. The main specimen-probe force is repulsive and thus the difference in height is recorded by adjusting the cantilever distance ($D_{1,2}$ in Figure 2.5) so that the resulting deflection is constant. In tapping mode, the cantilever is subjected to oscillations just below its resonance frequency, and while the surface forces tries to dampen this effect, the vertical position of the cantilever is regulated in order to keep the amplitude constant. This is usually done to register the surface geometry of very fragile materials, as the interaction in contact mode can be enough to destroy the sample or invalidate the results.[18]

2.2.2 Scanning electron microscope

A scanning electron microscope (SEM) uses electrons as a source of illumination. The general layout of a SEM column consists of an electron gun, two condenser lenses, an objective lens, an electron detection system and a set of deflectors. The assembly of these components is shown in Figure 2.7.
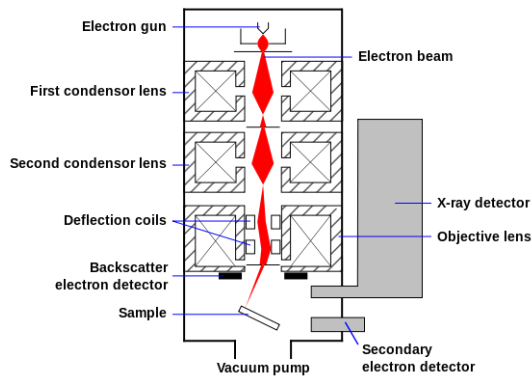
Figure 2.7: Schematic of a SEM. Image is taken from Wikipedia.[19]

The electron gun usually consists of a cathode made up of tungsten or LaB_6, which is heated by sending electrical current through it. In addition to the creation of light during this action, electrons are also released from it. By having two differently charged plates with a hole to guide the electrons, a resulting beam is created. This is illustrated in Figure 2.8. The speed of the electrons depends on the applied voltage to these plates, with a greater number resulting in a higher acceleration.
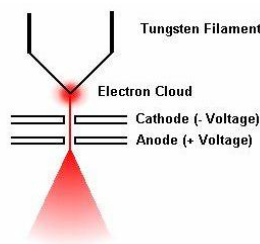
Figure 2.8: Detailed view of the electron gun. The figure is taken from Seal Laboratories.[20]

These electrons are then subjected to the lenses, whose main task is to focus the beam onto the specimen. The condenser lenses control the size of the beam, or the electrical current of it, while the objective lens focuses the beam into a spot on the sample. Increasing the current yields a better signal to noise ratio, but because the diameter of the beam is larger, the result is also a lower resolution.

A deflection system in front of the objective lens scans and guides the electrons to a raster-like pattern on the surface of the specimen and operates in synchronisation with a computer display or a cathode ray tube (CRT). As such, the image on the display has a linear relationship with the specimen raster. By decreasing the current through the deflection system's scanning coils and thus reducing the scanned area, a greater magnification can be obtained.

Lastly, a detection system is used to collect the different signals generated by the beam's interaction with the specimen.[21] These signals are shown in Figure 2.9.

9
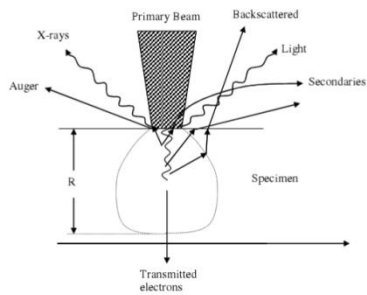
Figure 2.9: Signals generated by the SEM. Figure is taken from Khursheed, A., *Scanning Electron Microscope Optics and Spectrometers*. [21]

When the electrons interact with the specimen, they create a number of different signals that can be analysed. Most noteworthy are the secondary electrons and backscattered electrons. The secondary electrons are created when the electrons from the electron beam collides with electrons in the specimen. These electrons, if having received enough energy, will be released from their natural state and start to move out of the sample. The closer these electrons are to the surface, the greater number will be emitted due to reduced resistance. This is why the surface appears brighter compared to dimples when viewing results from secondary electrons. Backscattered electrons are electrons that are reflected from the specimen, usually by interactions with the nucleuses of the sample atoms. These will indicate the density of the material, as a dense material will result in a larger number of electrons.[22]

The SEM is not without limitations, however. Due to the electrons' sensibility to molecules between the sample and the electron launcher, both the specimen chamber and the column have to be situated in vacuum. This is due to the fact that the electrons are much more strongly scattered by gases than for instance light.[23] Another inconvenience is that since the electrons are electrically charged, the sample needs to be conductive to a certain degree in order to dissipate this charge.

An environmental scanning electron microscope (ESEM) bypasses this problem by having the specimen chamber separated from the high vacuum electron optics by separate pumped chambers and apertures, as illustrated in Figure 2.10. The main chamber is also filled with a pressurised gas, usually water vapour. This feature requires new sensors and detectors that can operate in these environments. The electron beam will be scattered when moving through the gas, resulting in an electron "skirt" being formed around the primary beam. This is termed oligo-scattering. If the gas pressure is too high, for instance at atmospheric pressure, the electrons will be completely scattered and no coherent beam is formed.

In general, the primary beam in oligo-scattering will yield just as good results as a focused beam, but more beam current is lost into the skirt, resulting in a lower signal from the impact point of the beam. As such, the contrast of small features is decreased. By using filtering techniques such as integration or averaging, high-resolution, high-quality images can be obtained. Alternatively, increasing the beam current or the dwell time may also increase the signal, but this can result in resolution loss at high magnifications and localised charging, respectively.[24]
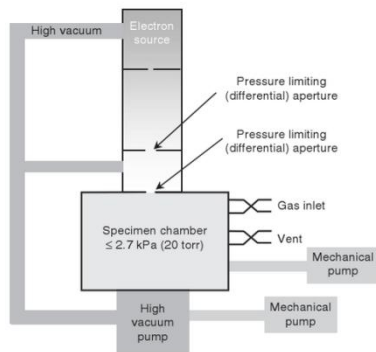
Figure 2.10: Schematic of an ESEM. Figure is taken from Stokes, D., *Principles and Practice of Variable Pressure : Environmental Scanning Electron Microscopy (VP-ESEM).*[24]

2.2.3 Focused Ion Beam

A focused Ion beam (FIB) works in a similar manner as a SEM, but instead of electrons, a FIB system uses ions. Gallium (Ga^+) ions are usually used, due to the material's low melting point, stability at this temperature, particle weight and visual characteristics. The weight is important as the ion needs to be heavy enough to allow milling, yet not to such a degree that it destroys the sample. Visibility of the ions is also useful as it then can easily be identified if implantation has occurred.

The gallium source is heated by a coil heater and the liquefied metal wets a sharp tungsten needle. The metal is then concentrated at the end of the needle with the use of electrodes, and a potential difference in the order of 10^{10} V/m between the tip and the aperture causes the ions to accelerate. The resulting ion stream is then focused by electrostatic and surface tension forces through the first aperture into a Taylor cone with an apex diameter of about 5 nm. The ion beam is further focused by a series of apertures and electrostatic lenses before it is released into the specimen chamber.[25]

A raster, similar to in SEM, is formed on the specimen surface and it is used to mill, image or deposit a material onto it.

Deposition is performed by creating a cloud of deposition material atoms (for instance platinum) above the sample and letting the ion beam strike these atoms, transmitting kinetic energy and causing them to impact the surface. Van der Waals forces will hold the atoms in place. This technique can be performed with both conductive and resistant materials, as the conductive properties of the suspended material do not matter. This can be used to improve electron beam imaging by depositing a thin layer of conductive material over the surface of the specimen.

Imaging is performed very similarly to the way it's done in SEM, but with the use of ions instead of electrons. As such, the test material will experience some damage during the operation. Ions are hitting the test material in inelastic collisions and create backscattered or secondary ions and electrons, as well as other signals. These are then picked up by sensors. Elastic collisions, where all the energy is transferred to the atoms of the material, result in milling (also called sputtering). However, in order for the sample atoms to leave the surface, they need to both receive enough energy to overcome the surface binding energy as well as moving in a favourable direction. The latter is also the reason why milling is more time consuming when there is only one free surface, as there are fewer ways to leave the material with the limited amount of energy the atom received.

A side effect of milling is the redeposition of ions and specimen atoms. After leaving the local milling area, they will in many cases reach another part of the specimen and deposit there. Except by creating a larger "exit path" or with the usage of a gas injection system, there is no way to prevent this.[25]

Other negative effects of the interaction with the ion beam include implementation of ions into the specimen and rise of temperature. The former has been found to influence the mechanical properties of the test material. A study performed by Orso on a 125 μm thick Kapton foil exposed to different amount of ions revealed that both the hardness and the Young's modulus had been changed. By using a nanoindenter, the effects could be measured. For the Young's modulus, the effect did not follow a particular trend, but rather fluctuated in levels above that of the original value. For instance, at a penetration depth of 30 nm, the Young's modulus had increased by 22 % between the unexposed material and the one that had been bombarded by $1{,}01 * 10^{18}$ ions/cm^2. [26]

The increase in specimen temperature has been calculated by Ishitani and Kaga to follow equation (2.1), where V is the acceleration voltage, I is the beam current, d is the spot size and κ is the thermal conductivity for the material.

$$\Delta T = \frac{V * I}{\kappa * d * \sqrt{\pi}} \tag{2.1}$$

A Gaussian type power profile was assumed, as well as having the temperature losses caused by sputtering, lattice damage, electron emission and ion backscattering neglected. The formula was calculated for bulk material, for semi-bulk materials, the temperature was found to increase by a factor of 2. For sheet samples and pillars, the factor was found to be just below 4.[26, 27]

2.2.4 **Nanoindenter**

A nanoindenter is an instrument used to measure the mechanical properties of small volumes. Usually, these properties consist of the hardness and the Young's modulus, but the nanoindenter is also capable of estimating the yield strength, fracture toughness, scratch hardness and wear properties.[28]

The nanoindenter works similar to the mechanical hardness tests, e.g. Brinell and Vickers, in the way that a tip is pressed against the specimen surface for a defined amount of time to allow elastic recovery and then released. In those hardness tests, the resulting imprint is optically inspected, but since the nanoindenter works on the microscale or even nanoscale, such a solution would be highly impractical. Oliver and Pharr developed an analytical method in 1992 in order to remove this hindrance and make nanoindentation viable in a scientific context.[28] In order for this method to be accurate, the exact shape of the indenter tip has to be known.

In general, indenter tips come in two shapes: spherical and pyramidal, with the latter having multiple sizes and geometries associated with it. Some of the geometries are illustrated in Figure 2.11.
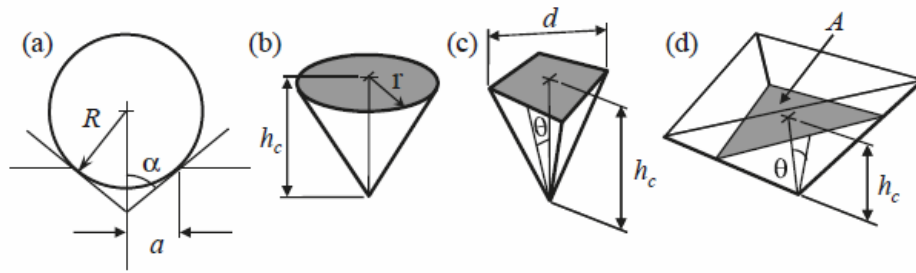
Figure 2.11: Indentation tips and parameters for (a) spherical, (b) conical, (c) Vickers, and (d) Berkovich indenters (not to scale). Illustration is taken from Fischer-Cripps, A.C., *Nanoindentation*.[29]

Each one of these has different parameters attached to it and will make different characteristic indentation marks. By combining these parameters with the results from indentation tests, one can calculate the area of contact and thus both the Young's modulus and the hardness of the material.

In addition to indentations, a nanoindenter can also function in as a scanning tool similarly to AFM and as a way of loading microstructures.

2.2.5 Picoindenter

A picoindenter is for most purposes a scaled-down nanoindenter, but instead of serving as a separate instrument, it is built to be able to fit inside a regular SEM, ESEM or FIB chamber. Due to this, both the instrument and the sample have to be vacuum-compatible and/or conductive. However, because of its location within a vacuum chamber, it has several distinct advantages over the nanoindenter.

First, it can be monitored by SEM/ESEM *in situ*, meaning the experiments can be seen in high magnification as the testing unfolds. This means that surface deformations are visible before post-test analyses. Secondly, it can be positioned vary accurately, allowing it to be applied on micron and submicron features more easily.[30] Thirdly, by also having an interchangeable indenter tip, it can be used in pillar compression testing or similar microscale experiments.

The resolution of the picoindenter is the same as the nanoindenter, having a load and displacement resolution of 3 nN and 0,02 nm, respectively.[31] However, the small scale restricts the specimen dimensions, as well as displacement- and load range of the system. It is also unable to perform experiments that can be executed in conventional indenter systems, for instance scratch resistance testing and electrical contact resistance testing.[32]

2.3 Mechanical testing – Hamm

In 2003, Hamm et al performed mechanical testing of live diatoms. The diatoms were of different species, but two were of centric shape. Using calibrated glass micro-needles to load and break the frustules, the force at fracture was recorded.[33] The results of these tests are shown in Table 2.1.

Table 2.1: Highest force at fracture for the diatoms tested by Hamm.[33]

Diatom species	Group	Diameter/longest axis, μm	Highest force at fracture, μN
Coscinodiscus granii	Centrales	130	90
Thalassiosira punctigera	Centrales	50	260
Thalassiosira punctigera	Centrales	100	180
Fragilariopsis kerguelensis	Pennales	30	730

As seen, the strength gets reduced by size, much like with ordinary materials, but having resisted pressures equal to 100-700 tonnes per square meter, even the weakest diatom is no pushover. A FEM model was made of the pennales diatom and loads were applied in different manners. Hexahedral elements (Hex8/C3D8) with a density of 350 elements per cubic micrometer were applied to the model. When having a force of 750 μN distributed across the valve and girdle bands, a von Mises stress value of 540 MPa was reached before fracture. When loading different parts of the frustule, tensile and compressive stresses were found to be 155 and 330 MPa and 560 and 680 MPa for the girdle band and the ribs on the valve, respectively. This suggested that the diatom frustule should have both high ultimate tensile and ultimate compressive strengths.

By using data from a compression test of a single girdle band and comparing that to a finite element simulation, the Young's modulus of Thalassiosira punctigera's silica was found to be 22,4 GPa. Even with a high degree of deformation, peaking at 2,5 % strain, the band exhibited a completely elastic response. This is in stark contrast to the normal behaviour of bulk silica.

2.4 Mechanical testing – NTNU

2.4.1 Nanomechanical testing of diatoms

In 2012, Bjørnøy performed a series of indentations of diatom frustules.[34] The main goal of his work was to develop a better method to perform material testing of the algae. One of the main issues was that with conventional bending tests, where the testing is performed on the material sample, the constraining material is not stiff enough to yield good results. By creating a sample holder out of steel and extracting a beam out of the diatom sample, Bjørnøy could perform tests which were less prone to external deviations and more related to the traditional three point bending test.

The test specimens were prepared using three different chemical agents. The purification process consists of a chemical washing treatment, followed by centrifugation and rinsing in water. This is repeated three times.

Ranging from mildest to harshest, SDS, H_2SO_4 and H_2O_2 were used. The SDS, an anionic surfactant, had the effect of leaving much of the organic matter behind, as well as doing little damage to the frustules. The sulphuric acid on the other hand, left the frustules more damaged, with fractures and broken areas. More organic matter had been removed when compared to the SDS-treatment. Lastly, the H_2O_2 had an even greater impact on the frustules, leaving very few intact, while almost completely removing the organic matter. This was deemed as an indication that the organic components influences the mechanical properties of the biosilica, as the cleaning process exerts the same amount of strain on the samples regardless of the chemical agent being used. In order to save time, the H_2SO_4-treated samples were excluded since it was deemed that the greatest difference would be between the two other chemical treatments.

In order to get data on the effects of the cleaning method, the frustules were subjected to nanoindentation. Frustules which had split into two valves were chosen for the tests, specifically the ones who had the internal surface pointing upwards. The diatoms were moved from their storage container using a pipette and placed on a glass slide. The ethanol, the fluid in which the diatoms were stored, evaporated thus in air, resulting in van der Waals forces to constrain the specimen.

Runs of 5-15 indents per frustule were executed with a cube-covered tip. An AFM scan was also taken before and after each nanoindentation session in order to confirm that the samples had not moved during testing and to view the indented area. Indentation was also done on a steel substrate sample in order to evaluate whether or not this would affect the three point bending test in a noteworthy manner. 25 indents were performed, with a force ranging from 400 µN to 4000 µN and AFM scanning before and after the indentations.

Unfortunately, the samples moved during the nanoindentation so no conclusive results could be obtained. However, the following was observed:

- The indentation depth was rather consistent in the H_2O_2-samples, while the indentation craters vary greatly in size for the SDS-samples.
- The appearance of the diatoms was very different from frustule to frustule. This was deemed as an indication of the samples being from different Coscinodiscus species.

- The deformation curves were divided into two slopes for both of the cases, but the effect was more pronounced for the H_2O_2-samples.
- Large pop-ins occurred in the SDS-samples.
- It was also found that the steel substrate was both hard and stiff enough to not affect the results of the tests.

To get the most accurate results from the bending test, a sample holder in steel was produced with the FIB. Beams made from the frustules were also produced in the FIB and subsequently transferred to the sample holder. This was then transported to the indenter for the bending tests. Before mounting the diatom samples in the FIB, they were coated with a 5 nm thick layer of platinum.

The fabricated beams were positioned onto the sample holder and a nanoindenter with a conical tip and a tip radius of 0,6 µm were used to fracture the beams. The load started at 200 µN, with a lower value chosen for the beams made out of single layers, and was increased by a rate of 27 µN/s. During the testing, it was observed that 50 % of the samples would move out of the sample holders, resulting in the following beams being fastened with small pieces of deposited platinum. The platinum was believed to only constraint the beams in the beginning of the tests and yield as the deformation increased. For the SDS cleaned samples, 5 beams were successfully tested, with one situated upside-down, as well as 1 foramen beam and a cribrum beam. For the H_2O_2 cleaned samples 8 beams were tested, with additional 2 foramen beams and 1 cribrum beam.

The force at fracture was found to vary heavily, ranging from 350 to 1050 µN but common for all tests was that the biosilica failed after little deformation, indicating brittle behaviour. The foramen layers failed at forces 4-10 times lower than this, but displayed lesser spread within the H_2O_2 prepared specimen. The SDS cleaned specimen appeared slightly stiffer.

Calculated values of fracture stresses and Young's modules were also performed, by assuming that the cross section of the beam could be described as varying between that of an I-beam and that of a hollow rectangular beam. The resulting stresses at fracture were calculated to be 365±92 MPa for the SDS-samples and 316±59 MPa for the H_2O_2-samples. The Young's modulus for bending or flexural modulus was calculated to be 5,72±2,90 GPa.

A FEM analysis of a typical beam was also performed, where it was shown that the holes in the structure made it more ductile without leading to stress concentrations. It also showed that the way the material was loaded had a great effect on the result, with a force distribution between the areola hexagons resulting in high local stresses in the cribrum. If the force was placed on top of the areola wall, the stresses would be distributed better. This was consistent with the testing, as fracture initiated both from the holes and the regions without any such features.

The issues caused by the advanced geometry and uncertain loading conditions aside, the diatoms seem to have created a clever way of increasing the stiffness and ductility. The ductile properties of the material, although not observed in Bjørnøy's study, may have been damaged by the chemical treatment in the preparation process or is more dependent on a larger section than that used in the samples.

Vebner continued Bjørnøy's work on the diatoms in 2013. The focus of his master thesis was to perform nanoindentations on the innermost part of the frustules, the foramen, as well as further

developing the diatom bending test. A more thorough investigation of the geometry of the frustules was also performed.[35]

The samples were prepared in the same manner as those used in Bjørnøy's experiments. That is, washed in a chemical agent, centrifuged and rinsed in water. The same goes for how the samples were moved to a glass slide.

A nanoindenter and a confocal microscope were used to document the shape of the foramen and the general size of the frustule. A sharp diamond cube-cornered tip with a radius of curvature of 40 nm was used during the scanning. The scan was performed at the very centre of the sample, covering a square-shaped area with sides of 60 μm. The goal was to quantify the dimensions of the internal dome, which was believed to have approximately the same shape for all the samples. Some of the samples had previously been subjected to mechanical testing but the indents from these were deemed to have a negligible effect on the global shape of the layer, as the brittle silica only induced local fractures.

14 frustules were imaged with the nanoindenter, of which 10 were successful, while 33 were examined in the confocal microscope. From these tests, it was confirmed that the centre of the frustule have a curved shape, as suggested by Bjørnøy, but the dimensions of the domes were found to be inconsistent and thus may not be suitable for geometry-dependant testing.[34]

Indentations in both the nanoindenter and picoindenter were then performed on the centre domes, the pores and the areas between the pores on the foramen. A cube-cornered tip with 90 degree edges were chosen in order to get a better indentation marks. The radius curvature of the tip was 40 nm. During testing, load control with a maximum load of 200 μN was applied. The result of the different indentation locations, numbering over 200 on 30 different frustules, varied greatly. In the pre-study done by Vebner, the SDS-cleaned frustules behaved stiffer compared to the new results. A possible explanation was the long storage time. A new batch of diatoms was prepared, but the results from these also varied greatly. The most probable explanation was therefore that the pre-treatment of the diatoms had changed during the two test sessions. This also indicated that the specimen were sensitive to the physical stresses induced by the chemical exposition and the physical centrifugation.

When testing the different areas, it was found that the further one indented from the areola structure, the bigger the chance of a pop-in. In the post-examination, cracks formed during testing were arrested in the foramen pores. As such, it is logical that the pores serve as a protection against crack propagation.

For the indentation of the pores themselves, it was found that the nanoindentations resulted in deflection depths of minimum 600 nm when the set-load of 200 μN was reached. However, during the picoindentations of the pores, remarkably high forces were needed to fracture the foramen. The loads were believed to be well distributed throughout the areola structure.

Lastly, 21 cantilever beams were made out of the foramen, in the manner shown in Figure 2.12. No successful tests were performed as the 10 beams that were brought to testing failed during the physical scan before the actual testing had begun. However, the progress and experiences were

documented to serve as a framework for further experiments. One of these failed cantilevers can be seen in Figure 2.12.
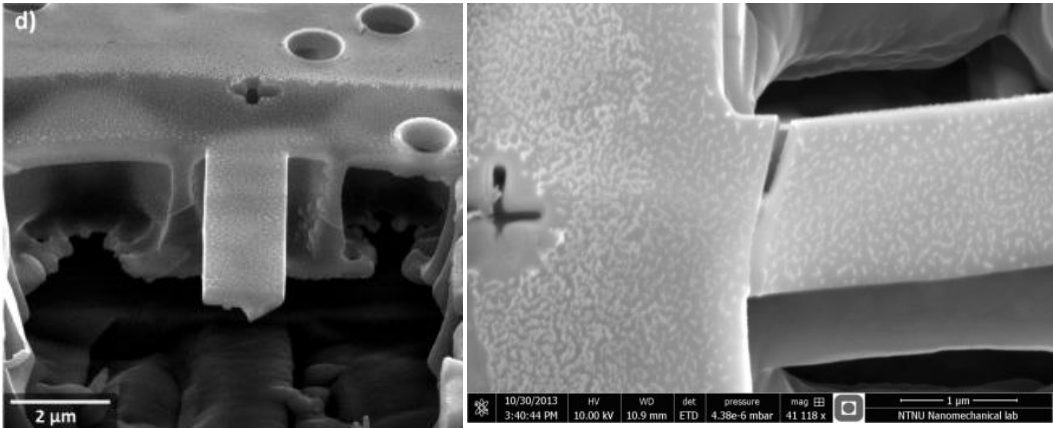
Figure 2.12:
To the left: Cantilever beam made by FIB. Image is taken from Vebner, M.J., *Nanomechanical Testing of Diatoms.***[35]**
To the right: The remains of a broken cantilever.

Two bending tests based on Vebner's work were successfully performed by Prof. Christian Thaulow. The fracture loads was found to be 38 and 36,6 µN with one of the results being displayed in Figure 2.13.
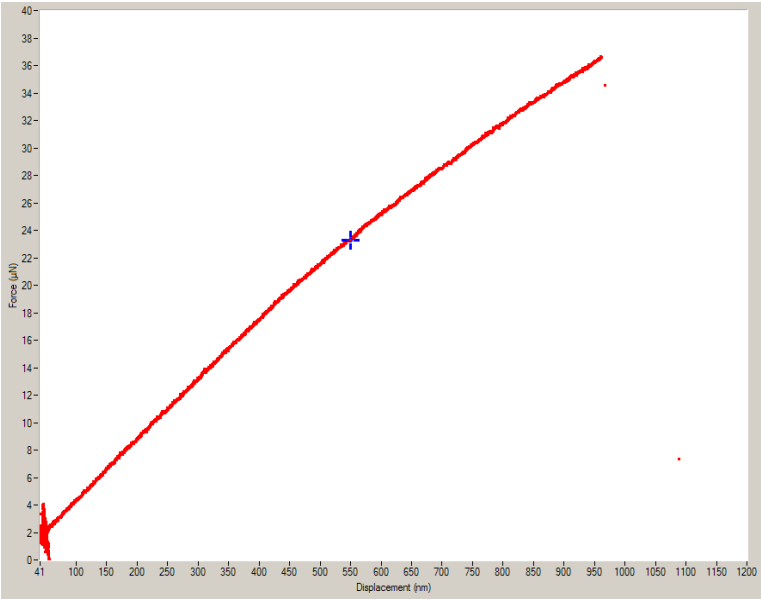
Figure 2.13: Output data from one of the cantilever bending tests performed by Prof. Christian Thaulow.

2.4.2   Diatoms in new design

In 2014, Morland continued with the work of analysing the biosilica, but with more focus on finite element modelling and analysis (FEM/FEA) than on mechanical testing. Two different models were made, one from the three point bending test and one from the cantilever bending test. Siemens NX was chosen to model the specimen and run the analyses.

It was found that in the three point bend test, the indenter would collide with the surrounding structure before reaching the foramen, as seen in Figure 2.14. Morland concluded that it was likely that the indenter had slid into the hole during the initial movement.
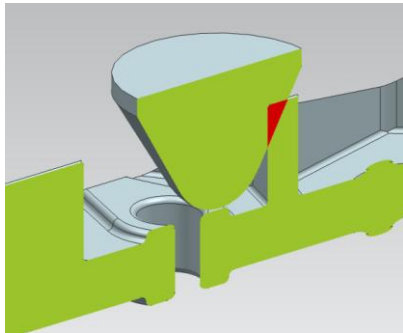
Figure 2.14: Section view of the three point bending test and indenter tip models. Figure is taken from Morland, M., *Diatoms in new design*.**[36]**

In the three point bending test, the load of 60,144 MN was distributed across the fillet of the centre hole while the load of 38 MN in the cantilever test was distributed across a circular area 3300 millimetres away from the base of the beam. By adjusting the Young's modulus until the desired deflection was attained, the final value of the elastic modulus was obtained.

To view the effect the different layers had on the mechanical properties, both the areola wall thickness and the foramen layer thickness were varied. The parameter study also served to make up for inaccuracies in the geometry. The difference in the areola wall thickness is displayed in Figure 2.15.
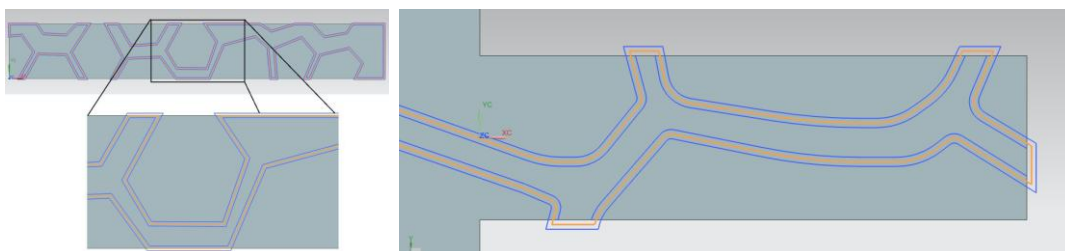
Figure 2.15: The different areola thicknesses used in the analyses. To the left, the three point bending test and to the right, the cantilever bending test. Figures are taken from Morland, M., *Diatoms in new design*.**[36]**

The final Young's modules for the cantilever bending test and the three point bending test ended up at 32,8 GPa and 35,9 GPa, respectively. High values for von Mises stresses were also observed, with the cantilever having a value of 3415 MPa while the three point bend model ended up at 2529 MPa. However, convergence was not reached for either of the models. For the three point bend model, the highest stress did not coincide with the area of fracture, which indicated that the results were of

high uncertainty. The different thicknesses resulted in large differences in the resulting stresses and in the Young's modulus, indicating the importance in using the correct dimensions.[36]

2.4.3 **Project work**

Prior to this master thesis, a project was performed that continued Morland's work. Both the cantilever and the three-point-bending models were reviewed in Abaqus, which was deemed to be a more advanced FEA-software. Due to the advanced geometry of the models, tetrahedral elements with extra integration points, C3D10, were being used, as well as a non-linear solver.

For both models, the mesh was refined at critical areas in order to reach convergence. The final mesh size for the three point bending model ended up at 20 nm for the elements around the hole, 7 nm for the elements on the corners where the maximum stress was observed and 150 nm for everything else. For the cantilever model, the global mesh size was set to 400 nm with mesh refinement on the cantilever geometry being 60 nm, while the mesh at the stress-sensitive areas being 3-5 nm.

By modifying the way the models were loaded by the use of a distributing coupling between the applied load and the loading area, converging results were obtained. The von Mises stresses were not viewed as the critical parameter for these models, as it does not take into account whether the stress field is dominated by compressive or tensional components. Instead, the maximum principal stress was studied, as the tensile forces were deemed more destructive for the material.

The Young's modulus was found to be 35921 MPa for the three point bending test and 32845 MPa for the cantilever bending test. The maximum principal stresses at the fracture inducing loads ended up at extremely high values compared to conventional materials, reaching a value of 3711MPa and 1757 MPa, with the former belonging to the cantilever model. The proximity of the Young's modules of the two models was deemed to be promising, but the difference in stresses meant that a value for the material's fracture strength could not be obtained. Additionally, the three point bending model did not have a stress concentration where the fracture initiated, and the stress values obtained from this study would therefore not be a valid value for the ultimate strength of the material.

However, the cantilever model displayed favourable fracture behaviour by having the highest stress appearing at the point of fracture, indicating that the model was largely realistic. The highest principal stress location can be viewed in Figure 2.16 while one of the failed cantilevers with a coinciding fracture initiation point is illustrated in Figure 2.12.[4] As such, it was concluded that the cantilever model was more fitted for future testing.
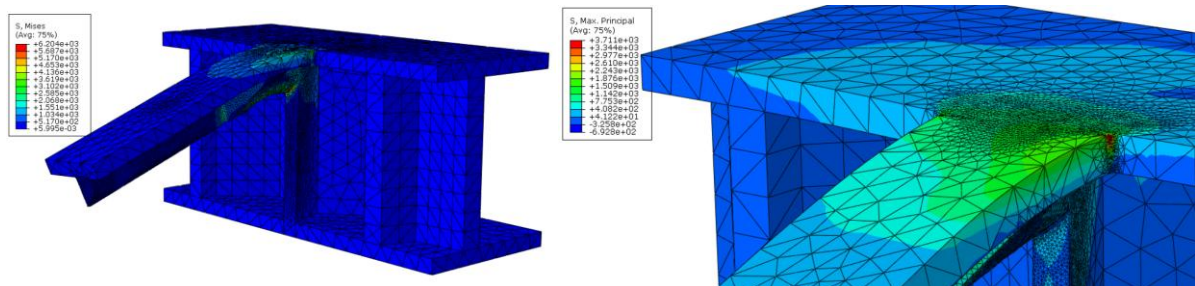
Figure 2.16:
To the left: The deformed cantilever model.
To the right: The stress concentration at the right corner of the cantilever base. The images are taken from Heggem, O.M., *NANOMECHANICAL TESTING OF DIATOMS.***[4]**

2.4.4 AFM-study of mechanical properties

Parallel to this project, Torstein Vågen Svendsgaard performed an AFM-study of the diatom frustules. Using a Veeco diMultiMode V AFM, both the topography and mechanical properties of the foramen, cribrum and cribellum layers were studied.

The measurements of the Young's modules of the layers were done by pre-calibrating the AFM-tip on a material with a known modulus and using that data to extrapolate the values from the test material. The measurements were performed at the very centre of the valves, the area surrounding the centre and the area close to the edge of the valve. The results can be viewed in Table 2.2.

Table 2.2: Young's modulus measurements of the different layers.

Layer	Young's modulus [GPa]			
	Centre	**Radial midpoint**	**Edge**	**Mean**
Foramen	28,62±4,45	30,73±5,09	20,29±3,11	26,55±4,22
Cribellum	22,60±2,29	28,92±5,36	22,08±3,22	24,53±3,62
Cribrum	22,60±2,29	28,92±5,36	22,08±3,22	24,53±3,62

2.5   **Comparison between the obtained material parameters**

Using the results from the cantilever model from the project work, the maximum principal stress of 3711MPa is considerably higher than what Hamm found in his analyses or the ones calculated by Bjørnøy. Bjørnøy's stresses, while having an average value ranging from 316 to 365 MPa, were based on the three point bending specimen and a simplified beam structure. One weakness with this approach is that it is highly geometry-dependant, as shown by Morland's results. By varying the foramen thickness by about six percent, the resulting stress increased and decreased by roughly the same factor. The difference between the results from the cantilever model and the ones obtained by Hamm is also quite large. His model only experienced a stress value of 680 MPa at its highest, but his mesh size of 350 elements/μm^3 results in an average size of around 142 nm. Compared to the elements of the cantilever, this is almost twice the size of the refined mesh on the beam. In addition, an even finer mesh of 3-5 nm is placed at the stress sensitive areas. The difference in stresses may be partly attributed to this inequality in mesh size.

The cantilever model was found to have a Young's modulus of approximate 33 GPa which is reasonably close to Hamm's value of 22,4 GPa. His tests were done on a girdle band and as such could have different properties because it is made by a separate SDV. The nanosphere size could also vary between the two diatoms or between the girdle bands and the frustules, resulting in a slightly different structure. Other sources of difference include difference in species and the chemical and mechanical treatment of the diatoms used in the cantilever testing.

The values obtained by Svendsgaard are very similar to the one obtained with the cantilever model. Since the cantilever was produced very close to the centre of the frustule, the value of the Young's modulus should be close to the ones measured either at the very centre or at the midpoint between the edge and the centre. The value of 33 GPa is thus in the upper range of those measurements, but fits otherwise perfectly with the listed values. As such, the value should be quite representative of the material.

The flexural modulus calculated to be 5,72±2,90 GPa by Bjørnøy seems to be too low when compared to these numbers but that is probably caused by the dimensions and formulas used to calculate the value.

2.6 Cantilever fabrication

In order to get reliable test results, the geometry of the material should be as simple as possible. As experienced by Bjørnøy in his master thesis, specimen made out of the entire frustule yielded scattered results, while the specimen made from only the foramen layer behaved in a more consistent manner.[34] As such, it was decided to shape the foramen layer into a notched cantilever beam with the FIB.

There are multiple ways to shape a material sample into a cantilever with the FIB, but they differ both in milling time and practicality. The most straight-forward technique is to tilt the sample 45 degrees from the surface plane to mill away a section and then simply rotate the sample 180 degrees and repeat the process. The resulting beam will then have a triangular cross section. By removing more material from one of the ends of the beam and from the sides, one will either obtain a cantilever with a triangular or a pentagonal cross section.[37-39] This process is illustrated in Figure 2.17.

The main drawback with this approach is that the cantilevers only have one axis of symmetry. When performing the tests, the crack width will vary during the loading phase if the cross section is triangular, or if the crack propagates too far if the cantilever has a pentagonal cross section. Another issue is that a large amount of specimen material needs to be removed when producing the cantilevers. This may result in accumulated FIB damage and the modification of the surface morphology.[25] If many cantilevers need to be tested, the fabrication process will also be very time-consuming. On the other hand, the cantilevers can be produced everywhere on the material sample, making it advantageous to use on materials with inhomogeneous properties on the micro- and nanolevel.
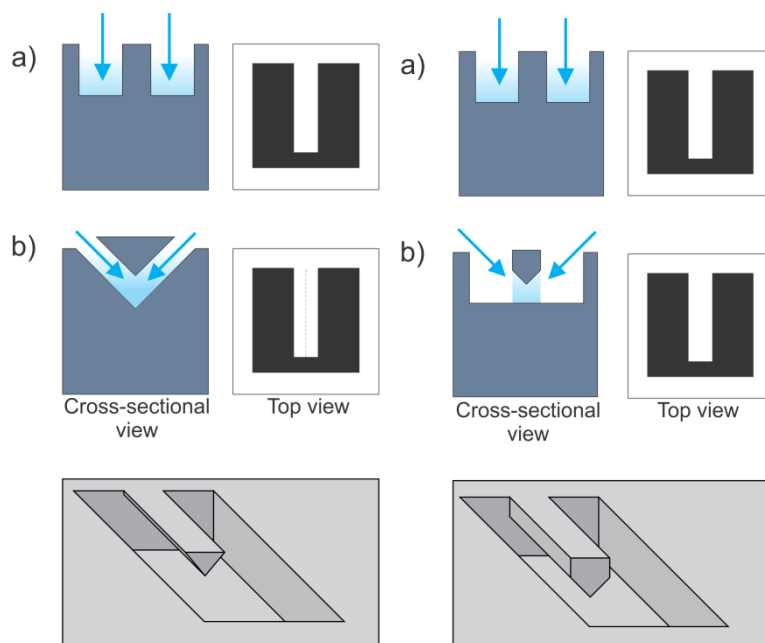
Figure 2.17: Schematic illustration of how to fabricate a cantilever directly from the surface of the sample.
To the left: Cantilever with a triangular cross section.
To the right: Cantilever with a pentagonal cross section.
The image is inspired by [40]

Another option is to start to mill from an available side surface and remove the material around the unfinished cantilever until the desired result is obtained. For a vertical cantilever, this is done in one operation, but for a horizontal cantilever, a manual tilt of 90 degrees is required before the final milling operation can begin.[41-43] This is illustrated in Figure 2.18.
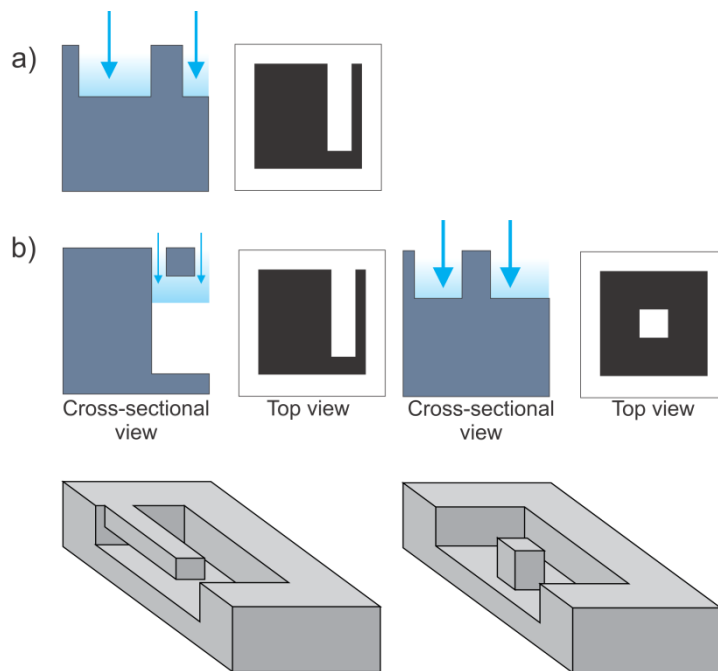
Figure 2.18: Schematic illustration of how to fabricate a cantilever from a free side surface of the sample, either by milling a horizontal or a vertical cantilever.

Compared to the first method, these cantilevers have symmetrical cross sections in both directions, but the placement of said structures are less flexible since they require a free side surface to enable indenter movement. Both methods require large amounts of sample material to be removed in order to fabricate cantilevers, with the vertical cantilever demanding the most due to its orientation. This requirement of material in the depth direction may result in the cantilever material having different properties along the length of the beam if the sample material changes properties beneath the immediate surface.

Lastly, it is possible to use thin material samples and mill out a beam without modifying the thickness of the sample. Based on the desired thickness of the cantilever, this is done by using a lamella and only milling away the surrounding material.[44] The result, as illustrated in Figure 2.19, requires a substrate when performing the indentations in order to give room to the deflection of the cantilever. However, this method requires small amounts of sample material and is thus less time consuming when being processed with the FIB, while also maintaining a square cross section. Compared to the second method, it can be performed anywhere on the surface of the sample, allowing greater flexibility in the placement of the cantilever. The small amount of material removed also means that the finished specimen will be less affected by ion implementation and similar effects from the FIB.
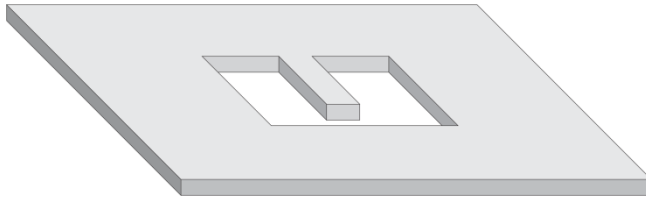
Figure 2.19: Illustration of a cantilever made from a thin material sample. The area surrounding the cantilever is simply removed with the ion beam.

It is also possible to manufacture thin films from bulk material. The ion slicer is commonly used to produce samples for Transmission Electron Microscopy (TEM) investigations by creating freestanding lamellae with a thickness of some micrometers, but can also be used to obtain very thin specimens. Compared to FIB, this instrument offers less damage to the material due to the usage of argon ions instead of gallium ions, as well as by having a lower acceleration voltage.[45, 46]

When used on a diatom, these techniques vary in effectiveness and viability. The last method, while viable if one can remove everything but the foramen layer, is not very practical due to the time and expertise needed to perform such an operation. Another issue is that the frustule is shaped like an elliptic paraboloid, having no flat surfaces besides the section at the very centre.[34] This makes it very hard to obtain a large enough surface which also has a constant thickness.

The second method has similar issues. Due to the lack of a free side surface, the diatom needs to be split in order to fabricate a cantilever. The layered structure will also complicate matters, making the vertical cantilever unable to be manufactured while the areola will be a hindrance for the horizontal cantilever. Tilting a small sample like the frustule will also be a very inaccurate process. As such, the first method is the most viable. Although time-consuming, its simplicity and flexibility will be crucial to the creation of the cantilevers.

2.7 Fracture mechanics

2.7.1 Fracture toughness and stress intensity factor

Historically from an engineering point of view, structures and materials have been limited by their resistance to fatigue and fracture. Modern structures and products are perhaps more vulnerable to these phenomena as they often are created with advanced shapes and by minimizing the material usage during the construction. In order to safely design products that can withstand cyclic loads, several methods for calculating the resistance towards crack-induced fracture has been developed.

In 1920, Griffith theorised that if a flaw reached a point of instability, fracture would occur. By using the first law of thermodynamics on an elliptical hole positioned in a large plate, he came to the conclusion that if the crack increment resulted in a strain energy change which overcame the surface energy of the material, the material would fail. Tests performed on glass specimen verified the theory, but following tests on metals made it clear that Griffith's model only applied to ideally brittle solids.[47, 48] By including the dissipated energy from local plastic flow, Irwin expanded Griffith's model to include metals in 1948.[49]

Nearly twenty years after Griffith published his model, Westergaard developed a method for analysing the stress- and strain situation ahead of a sharp crack.[50] After developing the energy release rate concept, Irwin used this approach in 1957 to show that the stresses and displacements near the crack tip could be described by a single constant, the stress intensity factor K.[51, 52]

During loading of a cracked sample, the stress intensity factor will increase until it reaches a critical value and unstable crack growth initiates. This critical value of K is known as K_C or the fracture toughness of the material.

The general expression for the stress intensity factor is given in Equation (2.2), where σ is the characteristic stress, a is the characteristic crack dimension and $f(a/b)$ is a dimensionless geometry factor that depends on the geometry and the mode of loading.[48] The denotation means that the factor is valid for mode I loading, which is when the tensile stress is normal to the crack plane.

$$K_I = \sigma\sqrt{\pi a}\, f\left(\frac{a}{b}\right) \tag{2.2}$$

2.7.2 The J-integral

When the plastic zone near the crack tip becomes larger, the stress intensity factor becomes less accurate, up to a point where it is no longer valid. Usually, this is when the material no longer can be described with the linear elastic model, but rather is characterised as having elastic-plastic behaviour. By the end of the 1960s, Cherepanov[53] and Rice[54] independently showed that an energetic contour path integral, the J-integral, was independent of the path around a crack. The integral was also shown to be equal to the energy release rate in a nonlinear elastic body containing a crack.

For a two-dimensional system, the J-integral is defined as:

$$J = \int_{\Gamma} \left(wdy - T_i \frac{\partial u_i}{\partial x} ds \right) \tag{2.3}$$

where w is the strain energy density, T_i is the components of the traction vector, u_i is the displacement of the vector components and ds is the length increment along the contour Γ, as illustrated in Figure 2.20.
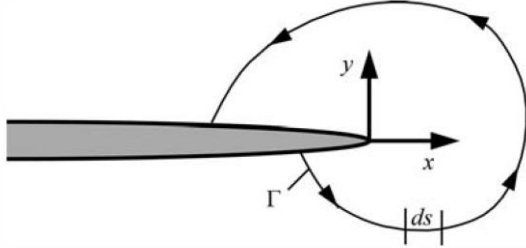
Figure 2.20: A contour around the tip of a crack. The image is taken from Anderson, T.L., *Fracture mechanics: fundamentals and applications.***[48]**

If the material analysed is behaves in a linear elastic fashion or yields a small plastic zone, the J-integral can be directly related to the stress intensity factor, as seen in Equation (2.4) and (2.5).

For plane stress:
$$J = \frac{K_I{}^2}{E} \tag{2.4}$$

For plane strain:
$$J = \frac{K_I{}^2(1 - v^2)}{E} \tag{2.5}$$

where E is the Young's modulus and v is the Poisson's ratio for the material.[48]

2.7.3   The cantilever model

As described in section 2.6, there are multiple ways to produce a cantilever specimen. However, only the pentagon cross section model is convenient to use on the diatoms. As seen in the previous chapter, the fracture toughness is dependent on sample geometry, the size and location of the crack and the magnitude of load, as well as the mode of loading.

In 2005, Maio and Roberts performed a series of test on coatings made from monolithic silicon and tungsten carbide.[39] The materials were used to produce pre-cracked microscale cantilevers with a FIB and subsequently loaded to fracture with a nanoindenter. In order to get a correct value of the fracture toughness from equation (2.2), the fracture load was inserted into an expression of the fracture stress, which was approximated as:

$$\sigma_f = \frac{FLy}{I} \tag{2.6}$$

where F is the fracture load, L is the distance between the crack and the indentation location, I is the moment of inertia of the beam cross section and y is the distance between the upper surface and the neutral plane. A weakness with this expression is that it is only accurate with small deformations, as for instance the horizontal loading length will change with large deformations.

The moment of inertia of the beam was calculated as:

$$I = \frac{wh^3}{12} + \left(y - \frac{h}{2}\right)^2 hw + \frac{w^4}{288} + \left[\frac{h}{6} + (h - y)\right]^2 \frac{w^2}{4} \qquad (2.7)$$

where the dimensions w and h are shown in Figure 2.21 while the distance y was expressed as:

$$y = \frac{\frac{h^2 w}{2} + \frac{w^2}{4}\left(h + \frac{w}{6}\right)}{hw + \frac{w^2}{4}} \qquad (2.8)$$

By using a boundary element method (BEM) software, the expression for $f(a/h)$ was found to be:

$$f\left(\frac{a}{h}\right) = 1{,}85 - 3{,}38\left(\frac{a}{h}\right) + 13{,}24\left(\frac{a}{h}\right)^2 - 23{,}26\left(\frac{a}{h}\right)^3 + 16{,}8\left(\frac{a}{h}\right)^4 \qquad (2.9)$$

where a is the crack length and h is the height of the parallel vertical sides. This expression is only valid when $0{,}3 \leq a/h \leq 0{,}5$ and was found by calculating the relationship between the applied load and specimen/crack geometry.

Zhao et al.[37] had a similar approach, but instead of using a BEM/FEM model, the dimensionless geometry factor was taken from Murakami[55] and is given by:

$$\begin{aligned} f\left(\frac{a}{h}\right) = {} & 1{,}122 - 1{,}122\left(\frac{a}{h}\right) + 3{,}74\left(\frac{a}{h}\right)^2 + 3{,}87\left(\frac{a}{h}\right)^3 - 19{,}05\left(\frac{a}{h}\right)^4 \\ & + 22{,}55\left(\frac{a}{h}\right)^5 \end{aligned} \qquad (2.10)$$

This is different from the one used by Maio and Roberts, but it is also considerably older. The rest of the calculations were approached in an identical manner.
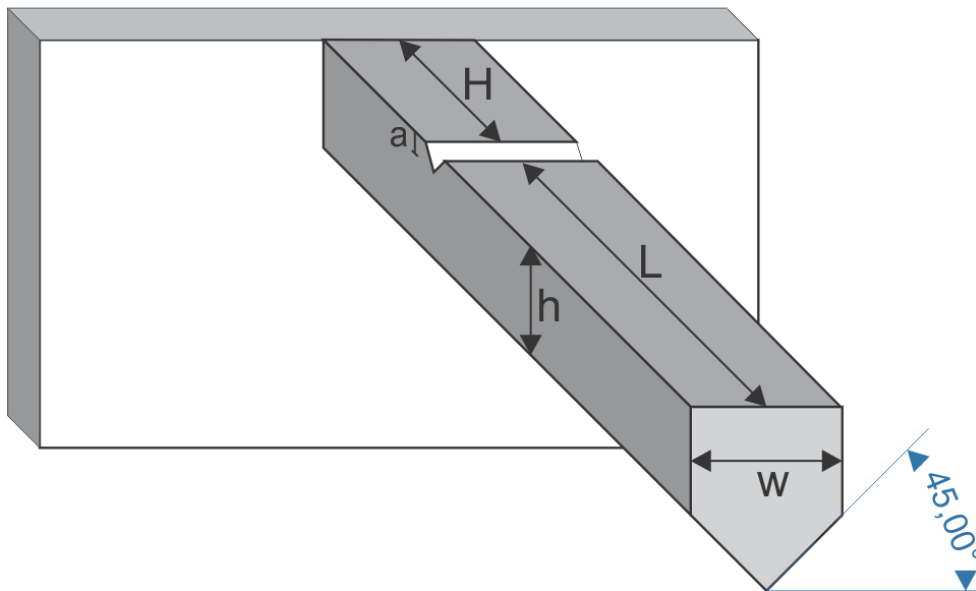

Figure 2.21: The defining dimensions of a cantilever with a pentagonal cross section.

2.7.4 Cantilever geometry and the dimensionless geometry factor

The dimensions of the FIB milled beams may deviate from the set parameters to some extent due to the difficulties involved with accurately controlling the process. The dimensionless geometry factor will suffer because of this, especially if there is a large change in the ratio of crack length to the height of the parallel sides of the cantilever.

In order to better understand how these geometry changes affect the results, Durst and Ahmad[56] performed a study in which they varied the dimensions of the beam and observed the change in the fracture toughness. This was done by using Abaqus to model a cantilever and then vary the different dimensions. It was found that the stress intensity factor and the applied force varied with a change in the geometry parameters.

Apart from verifying the approach, the paper used the equations and experimental results from Matoy et al.[57], in which cantilevers with square cross sections were loaded to fracture. The geometry factor and the employed expression for the stress intensity factor are shown in equation (2.11) and (2.12) respectively, with Figure 2.22 illustrating the different parameters. The geometry factor was reported by Matoy et al. to only be valid for a/h ratios between 0,05 and 0,45, as well as when the aspect ratio of the beam was $H:L:h:w = 2:5:2,1:1,7$.

$$f\left(\frac{a}{h}\right) = 1{,}46 + 24{,}36\left(\frac{a}{h}\right) - 47{,}21\left(\frac{a}{h}\right)^2 + 75{,}18\left(\frac{a}{h}\right)^3 \tag{2.11}$$

$$K_I = \frac{FL}{wh^{\frac{3}{2}}} f\left(\frac{a}{h}\right) \tag{2.12}$$
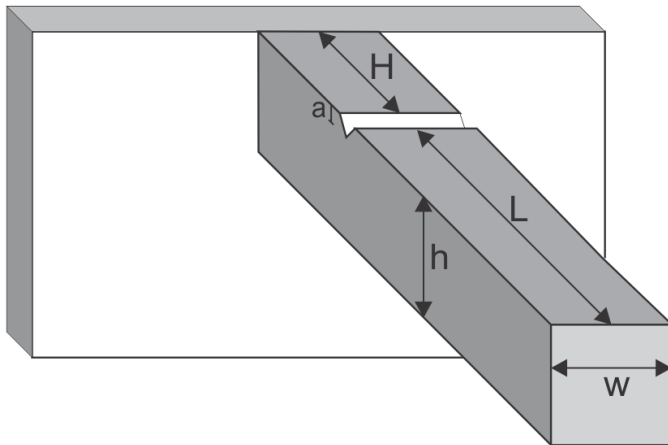
Figure 2.22: The defining dimensions of a cantilever with a square cross section.

The model was loaded until a specific deflection was reached, at which point the simulation stopped and the data from the analyses were examined and compared.

First, the ratio of crack length (a) to specimen height (h) was evaluated. The resulting stress intensity factors were plotted against the force required to deflect the beam. From Figure 2.23, it is seen that the magnitude of the crack length negatively affects the cantilevers' resistance to external forces. This is indicated both by the beams needing lower loads in order to reach the desired deflection and

by the increasing stress intensity factor. The geometry factors were calculated for the different *a/h* ratios and compared to literature values where they were found to be in good agreement. This was done by applying the results from the simulations to equation (2.13).

$$f\left(\frac{a}{h}\right) = \frac{K_I w h^{\frac{3}{2}}}{FL} \tag{2.13}$$

By keeping the a/h ratio constant and varying the width (w) to height (h) ratio, it was observed that the cantilever with the highest ratio resulted in a higher force required to reach the target deflection, but there was not any difference in the stress intensity factor at this level. This is illustrated in Figure 2.24. The geometry factor was found to be independent of the *w/h* ratio.

However, it was also reported that when the same force is exerted, the beam with the lowest *w/h* ratio had a higher stress intensity factor but a lower deflection value. Judging from Figure 2.24, this is not correct. When the same displacement is being reached, the stress intensity factor will be the same and the forces exerted will be different. In other words, the beam with the lowest *w/h* ratio will, at a comparable force, have a higher stress intensity factor and result in a higher deflection value.

By using the data provided by the different graphs and model dimensions, and by inserting the *w/h* ratio into equation (2.12), equation (2.14) was obtained, with the results of the calculations being shown in Table 2.3. The geometry factor was also taken from the same paper and controlled to be correct.

$$K_I = \frac{FL}{\left(\frac{w}{h}\right) h^{\frac{5}{2}}} f\left(\frac{a}{h}\right) \tag{2.14}$$

Table 2.3: Comparison between the values read from Figure 2.24 and the calculated stress intensity factor.

h [μm]	L [μm]	w/h	a/h	f(a/h)	Displacement [μm]	F [μN]	K − graph [MPa√m]	K − calculated [MPa√m]
1,8	5	0,6	0,5	11,2	1	310	6,6	6,66
1,8	5	0,81	0,5	11,2	1	420	6,6	6,68

Since the graphical values were picked by direct measurements, the values of the calculated stress intensity factor are deviating by a minor degree. However, the results show that when the height of the cantilever is kept constant while varying the width, an identical displacement will yield the same stress intensity factor. As such, while varying the width of the beam, the ratio of displacement to stress intensity factor will be constant. This means that the *w/h* ratio does not need to be consistent across the tests in order to get comparable results, but if the heights of the beams are changed without a corresponding change of the crack length, a different geometry factor must be applied.

Figure 2.23: Stress intensity factors for different crack length to specimen height ratios. The image is adapted from Durst, K. and S. Ahmad. *Fracture simulations of micro-cantilever beams using Finite element modeling.***[56]**
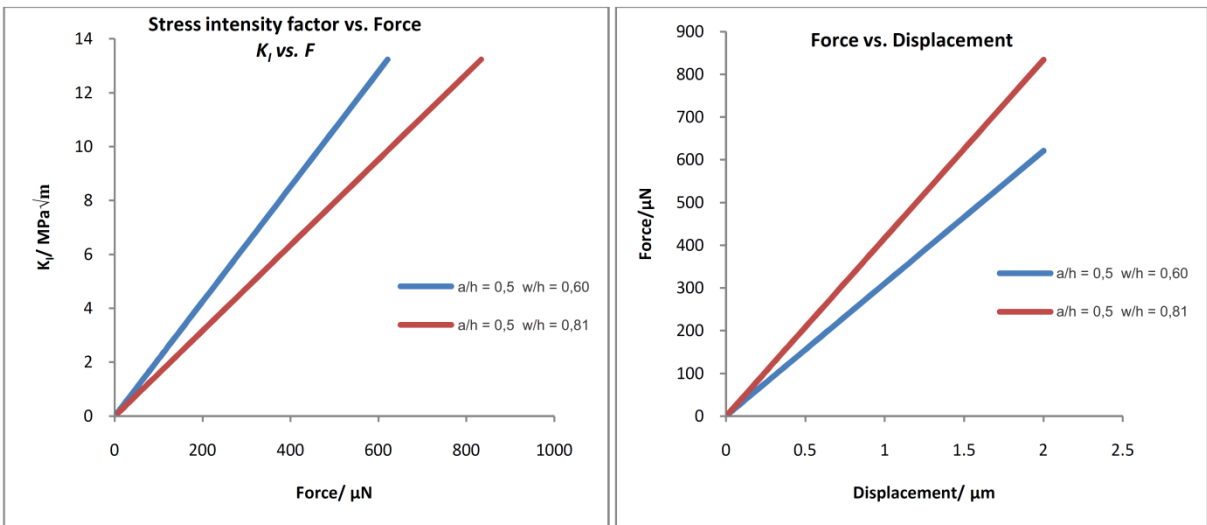
Figure 2.24: Comparison of how the *w/h* ratio affect the results while the *a/h* ratio is constant. The image is adapted from Durst, K. and S. Ahmad. *Fracture simulations of micro-cantilever beams using Finite element modeling.***[56]**

Lastly, simulations were performed to document the effect of the loading point (L). The obtained results show that both the values of the stress intensity factor and the force both decrease with increasing loading point distance, as seen in Figure 2.25. The geometry factor was then calculated. It was found that the values remained the same for the different loading positions and was in good agreement with the literature values, having only a deviation in the range of 0,4 %.
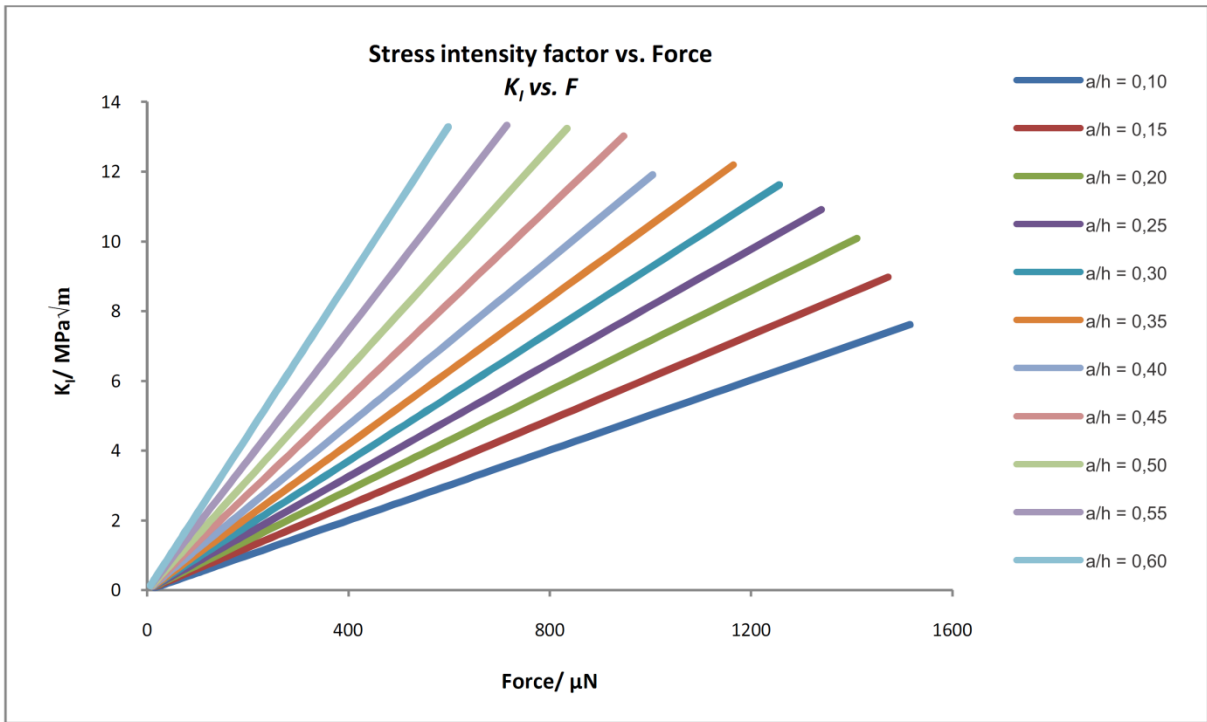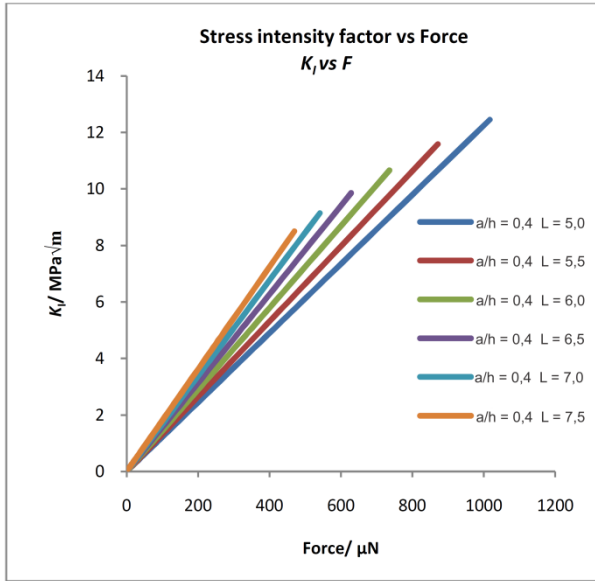
Figure 2.25: Stress intensity factor for different loading point distances. The image is adapted from Durst, K. and S. Ahmad. *Fracture simulations of micro-cantilever beams using Finite element modeling.*[56]

Iqbal et. al[58] performed a similar study on a cantilever identical to the one used by Matoy[57], where the aspect ratio was changed between analyses. By changing the dimensions illustrated in Figure 2.22 from $H:L:h:w = 2:5:2,1:1,7 \rightarrow w/h = 0,8$ to $H:L:h:w = 2:5:2,1:1,3 \rightarrow w/h = 0,6$ and by varying the *a/h* ratio, the effect of the geometry on the dimensionless geometry factor could be studied. By plotting *f(a/h)* from equation (2.13) against *a/h*, an expression for the constant could be derived by applying a cubic polynomial fitting. The model used, as well as the polynomial curve are illustrated in Figure 2.26, with the resulting expressions given in equations (2.15) and 2.16).
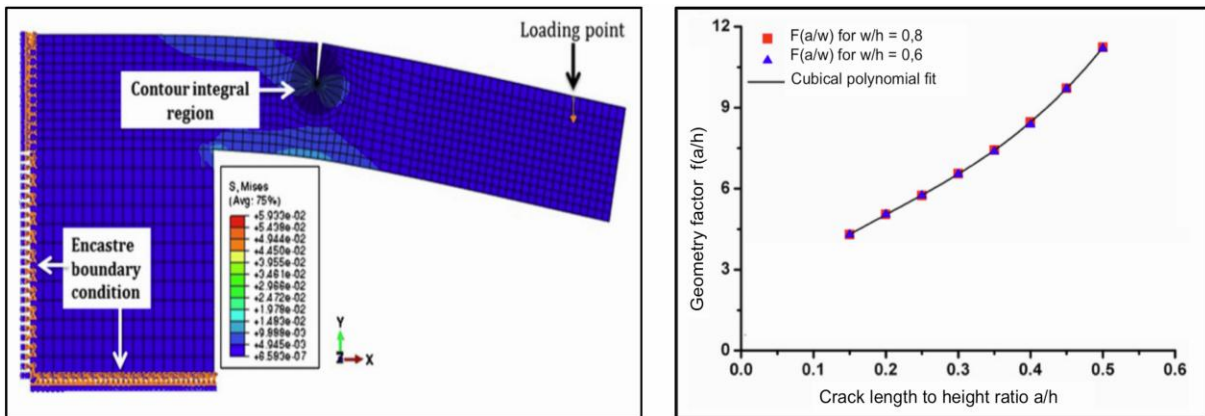
Figure 2.26: 2D FE-model with the resulting geometry factors for different *w/h* **ratios. The image is adapted from Iqbal, F., et al.,** *In situ micro-cantilever tests to study fracture properties of NiAl single crystals.*[58]

$$\frac{w}{h} = 0,8 \rightarrow \quad f\left(\frac{a}{h}\right) = 1,52 + 24,184\left(\frac{a}{h}\right) - 48,422\left(\frac{a}{h}\right)^2 + 77,608\left(\frac{a}{h}\right)^3 \quad (2.15)$$

$$\frac{w}{h} = 0,6 \rightarrow \quad f\left(\frac{a}{h}\right) = 1,603 + 23,055\left(\frac{a}{h}\right) - 43,755\left(\frac{a}{h}\right)^2 + 72,106\left(\frac{a}{h}\right)^3 \quad (2.16)$$

The equations, while very similar, were also in good agreement with equation (2.11) from Matoy et al. and confirms that the dimensionless geometry factor is largely unaffected by a change in the *w/h* ratio.

2.8 Fracture mechanic testing of silicon-based materials

The tests performed by Di Mayo and Roberts included four test cantilevers made out of monolithic silicon. These were exclusively produced with FIB-milling, in a similar fashion to the procedure discussed in section 2.6 for cantilevers with a pentagonal cross section. The notch was created by milling successively deeper rectangles in the beam. A nanoindenter was used to both scan the beams for the indentation position and to apply the bending load. The loading rate was set to 20 N/s.[39]

Matoy et al. also performed material testing of the mechanical behaviour of silicon based materials, but this was done in a study of silicon-based thin films. The materials studied were amorphous PECVD silicon oxide (a-SiOxHz), amorphous PECVD silicon oxynitride (a-SiOxNyHz) and amorphous PECVD silicon nitride (a-SiNyHz).

Nine cantilevers were successfully tested, whereas two were produced from silicon oxide, three from silicon oxynitride and the rest from silicon nitride. The beams were produced by a combination of lithography and FIB milling, with the FIB adjusting the imperfect etched geometry. Indentation marks as well as the notch were also milled out with the FIB. The notch was created by scanning the ion beam above a straight line on the beam top surface. The depth of the notch was identified after the fracture experiment using SEM. The loading of the cantilever beams was performed with a nanoindentation system attached to an atomic force microscope. A cono-spherical tip with a radius of 550 nm was used as a deflection tool and the load rate was set to 1 mN/s.[57] The fracture load was used with equation (2.12) and (2.11), with the latter being calculated by Abaqus.

The results from these experiments, as well as the typical dimensions of the cantilevers, can be seen in Table 2.4.

Table 2.4: Dimensions and fracture toughness from theory. The values were obtained from Di Mayo and Roberts and Matoy et al..[39, 57]

Material	Cross section shape	Notch length, a [nm]	Loading distance, L [μm]	Width, w [μm]	Height, h [μm]	Fracture toughness, K_{Ic} [MPaVm]
Monolithic Si	Hexagonal	Approx. 10	9,5	4	2,8	1,1±0,016
Silicon oxide	Rectangular	340-380	5,1-5,2	1,69	2,1	0,63–0,72
Silicon oxynitride	Rectangular	380	5,2	1,65-1,67	2,1	0,91–1,00
Silicon nitride	Rectangular	290-350	4,9	1,45-1,61	2,1	1,54–1,73

3 Experimental details

This section concerns the creation of finite element analyses and the parameters used. It also contains information about the production of cantilevers made out of the foramen layer, fracture testing of said cantilevers and other details relevant to the experiments performed.

3.1 Geometry factor analysis

The geometry factor has considerable impact on the stress intensity formula. There have been some results from testing of cantilevers with pentagonal cross sections, but these have had a larger rectangular section than the cantilevers produced in this project. In order to verify or obtain a new geometry factor, a FEM model was created and analysed.

3.1.1 Material properties

The material properties were copied from the project work leading up to this master thesis, as these yielded the correct results compared to the material tests.[4] The results from Svendsgaard's AFM study also support these parameters. Thus, the material was described as having a Young's modulus of 32845 MPa and a Poisson's ratio of 0,33.

3.1.2 Geometry and mesh

The model was based on one of the cantilevers produced, with measurements from the project work serving as assistance if the dimensions were unknown. The model was based on multiple SEM and FIB images, where some can be seen in Figure 3.1.
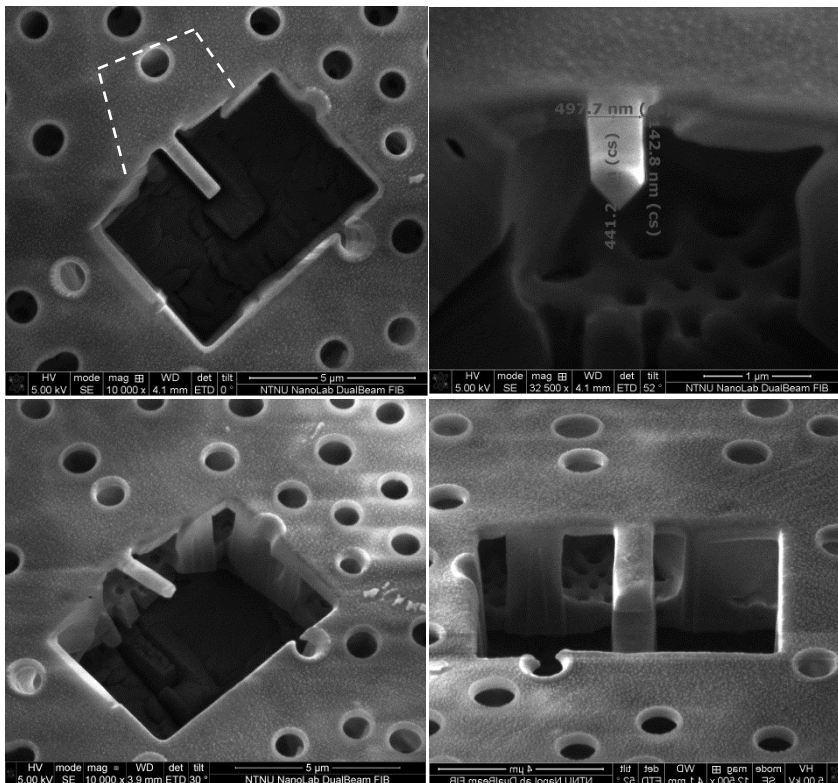

Figure 3.1: Images used to create the FE model. The top images were used to obtain the dimensions, while the bottom images were used to control the measurements. Note that the bottom right image is depicting the cantilever prior to its completion. This was used to document and compensate for the material redeposition.

It was assumed that the surrounding structure had a negligible impact on the results. Therefore, only a relatively small area surrounding the cantilever was modelled. Rounded and curved surfaces were straightened out in order to use a more accurate element type. Another reason was that these minor features were deemed to not contribute to the resulting stress distribution, as the stresses would be concentrated around the crack. Overly detailed surroundings would therefore only increase the time consumption of the analysis and lead to a more difficult meshing process. The curvature of the cantilever was negated in this instance, as a straight cantilever would yield comparable results to the geometry factors described in section 2.7.3. The finished model is depicted in Figure 3.2, with the characteristic dimensions listed in Table 3.1.

Table 3.1: The characteristic dimensions of the model.

Aspect	Dimensional size [nm]
Notch length, a	45
Loading distance, L	1500
Cantilever width, w	498
Height of the vertical sides, h	143
Cribrum thickness	500
Foramen thickness	445
Areola height	2165
Areola thickness	320

The model was created in Siemens NX, and imported into Abaqus in order to run the analyses. However, due to a limitation in the NX code, the model dimensions had to be designated in millimetres. When it was imported into Abaqus, the model was scaled by a factor of 10^{-6} in order for the dimensions to be in nanometres.
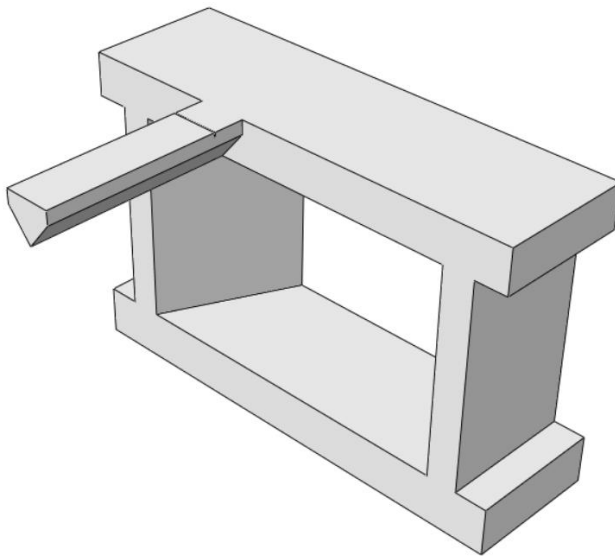
Figure 3.2: The finished model.

The crack was modelled in two different ways, one sharp and one rounded, as depicted in Figure 3.3, with the crack front defined as the line in the very bottom. Collapsed elements were employed to simulate the linear elastic singularity at the crack tip. The analyses were performed with 15 contours active for every element group along the notch width. Based on the results, the depth of the rounded notch was prolonged from 31 % of the height of the square section to 42 % and 50 % in order to see

how this affected the stress intensity factor. The rounded notch was chosen for these analyses, as it was deemed to be a more accurate representation of the notch produced with the FIB.

In order to get a value for the stress intensity factor, both a direct output request and the usage of the J-integral was applied. As the direct output resulted in a large spread in results, only the J-integral method was applied to the following analyses. The reason for this is that the direct measurements are very sensitive to mesh size, while the J-integral is more mesh-independent due to the utilisation of contours.[48]
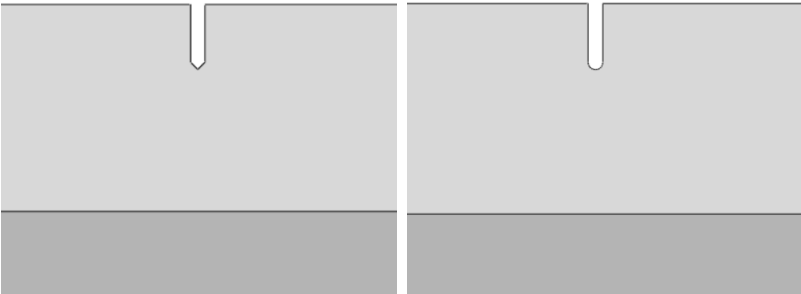

Figure 3.3: The modelled notches, one being sharp while the other was rounded.

Due to the performed simplifications, twenty node brick elements with reduced integration points, C3D20R, could be used. These elements provide a very accurate solution, while the reduced integration points make them resource-effective. Compared to the same elements without reduced integration and the comparative eight node elements, these offer the most accurate bending stiffness without using excessive amounts of elements across the thickness of the cantilever. A linear solver was chosen as this would save resources and because only small deflections were being tested in these simulations, as it was believed that the material would behave in a brittle manner.

In the initial study, the mesh was refined in order to obtain convergence, with the smallest elements being placed around the notch. The mesh size around the notch was varied from 6,6 to 1,6 nm while the surrounding structure had a mesh size of around 100 nm, depending on where it was measured. The distribution of elements around the sharp and rounded notch is illustrated in Figure 3.4 and Figure 3.5, while an example of the entire model is depicted in Figure 3.6.
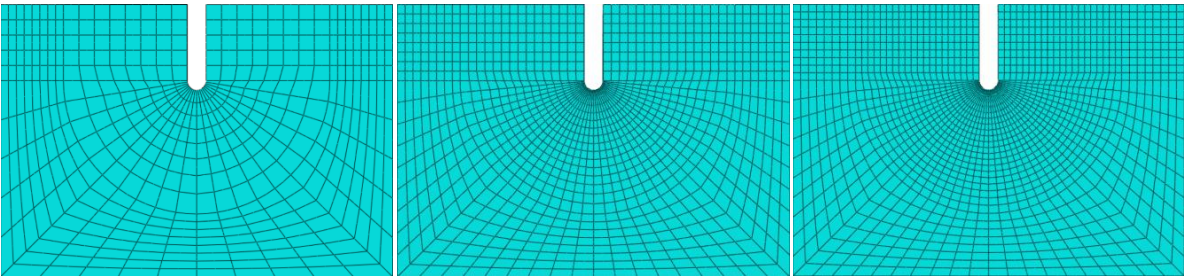

Figure 3.4: The mesh used during the rounded notch analyses. From left to right: notch element size of 6,6, 3,9 and 3 nm.
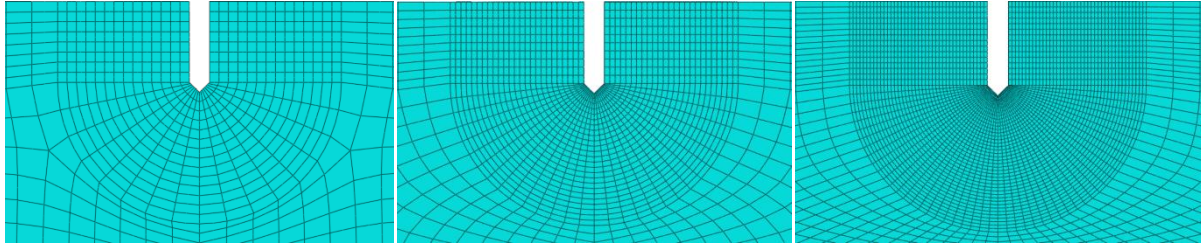
Figure 3.5: The mesh used during the sharp notch analyses. From left to right: notch element size of 4,7, 2,6 and 1,6 nm.
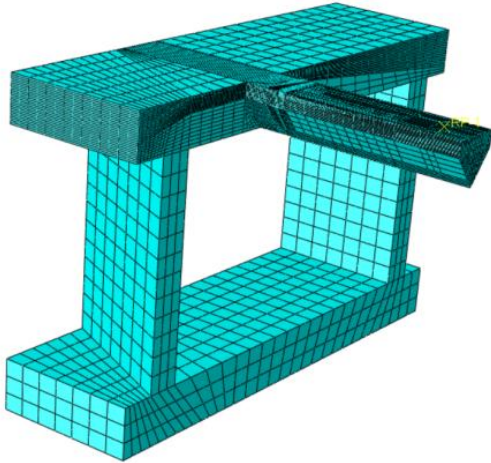
Figure 3.6: Mesh of the entire model. The mesh is smallest in the areas surrounding the notch, with coarser mesh applied on the rest of the cantilever and the surrounding structure.

3.1.3 Loading

In order to distribute the load across an area near the edge of the cantilever, a reference point was created at the location of the indentation mark. This point was then connected to the surrounding region, as seen in Figure 3.7, by the use of a distributing coupling. This will allow the force to be distributed across the area without creating additional stiffness.
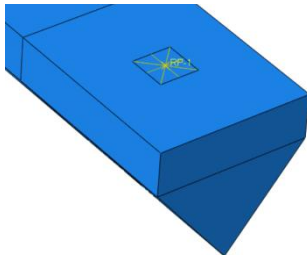
Figure 3.7: Load distribution.

The applied load was set to 8,625 µN. Originally, a circular area was chosen as the area of loading, but since this caused incompatibility with the surrounding mesh, a square area was chosen instead. This should have no impact on the results, as only the fact that the force is being distributed across roughly the same area is important in a cantilever study. The model was constrained in accordance to Figure 3.8.
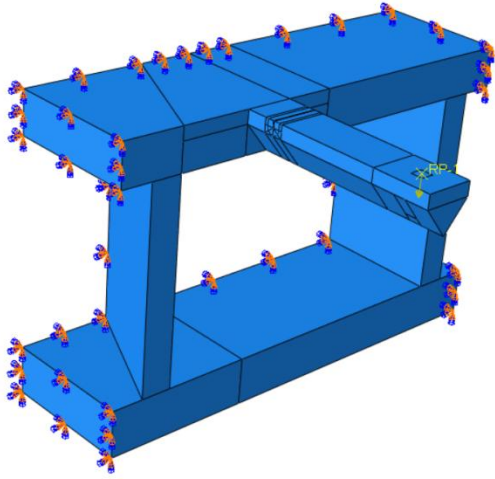
Figure 3.8: Boundary conditions of the model. The blue and orange arrows represent encasement, meaning no degrees of freedom, while the yellow arrow represents the load applied.

3.2 **Cantilever production process**

Prior to the actual testing, old diatom frustules used in previous master theses were used for experimenting what would yield the best results in the FIB. These frustules had already been coated and had been placed on stubs of different sizes. As the markings of the external containers had worn off, it was difficult to precisely tell from which study they came from. However, most of them seemed to be from Vebner's experiments[35], as they did not appear to be placed on double sided tape and several had the characteristic cantilever craters.

New diatom samples were also produced. This was done by using a needle to collect and transport the frustules from an ethanol solution to multiple AFM-plates. These steel plates were chosen because it was believed that it would make the positioning in the picoindenter easier, as well as enabling them to be analysed with the AFM. The ethanol was then evaporated and the frustules were viewed in a microscope to confirm the position and orientation of the different specimen. A common issue was that they would lie on top of each other, but nothing could be done to prevent that, as attempts to modify their positions resulted in broken frustules. The plates were then fastened to specimen stubs with the aid of translucent carbon tape and coated with an 80 % platinum and 20 % palladium layer using a Cressington 208 HR B sputter coater. The first specimens were only coated with a 5 nm thick layer, but this proved to be insufficient to prevent charging effects. The rest of the samples were therefore coated with a 10 nm thick layer. It was also performed experiments regarding the usage of carbon tape between the AFM plates and the frustules, but this resulted in broken frustules or other diatom material interfering with the undamaged valves.

The production of the cantilevers was performed with a FEI Helios NanoLab DualBeam FIB at NTNU Nanolab. Frustules close to the centre of the stub were chosen, as it was believed that these where within the movement range of the picoindenter. Since the deposition of diatom frustules on the stubs cannot be done in an exact manner, many of the frustules will be oriented in the wrong position. Only frustules having the foramen layer facing upwards could be used. Many possible candidates were discarded as they did not have a stable enough contact with the stub, either because they were slightly tilted or because components from broken diatoms were interfering with the contact surfaces.

The appropriate frustules were then rotated in such a way that a cantilever could be produced between the holes in the foramen, as illustrated in Figure 3.9. When this had been done, the milling procedure was initiated. This process consists of a series of different stages with different milling parameters, as listed in Table 3.2.
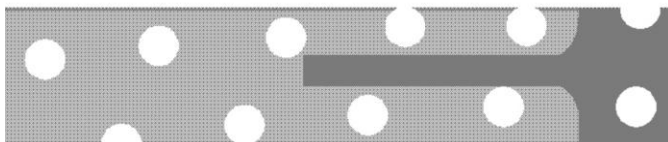
Figure 3.9: Possible orientation of a cantilever. The figure is taken from Bjørnøy, S.H., *NANOMECHANICAL TESTING OF DIATOMS***.[34]**

As the purpose of the first steps is to remove a relatively large amount of material, a high beam current was chosen in order to save time. If it was set too high, the resulting dimensions would often

be very inaccurate, especially at the corners of the pattern. While this was not a problem if the pattern was set up properly, it could result in the base of the cantilever being slightly uneven, which would need to be corrected at a later stage. Another important aspect of this step was to mill away enough material. If the crater was too small, material redeposition on the cantilever was a bigger issue. The indenter also required some space during loading in order to not coming into contact with the surrounding structure, resulting in the need for a large crater.

The next part, the correction and cleaning of the edges, was important because it limited the amount of material that needed to be removed during the milling of the bottom of the cantilever. Another effect was that it made the following steps more accurate because the sides had become parallel and less sloped in both the vertical and horizontal directions.
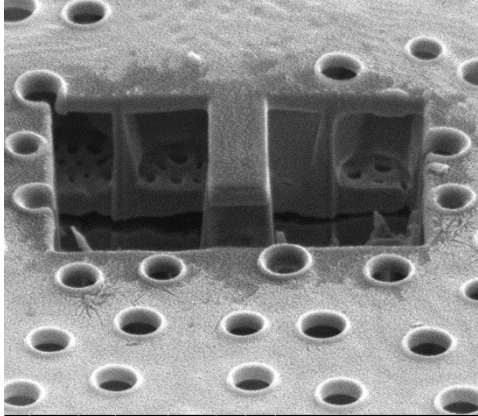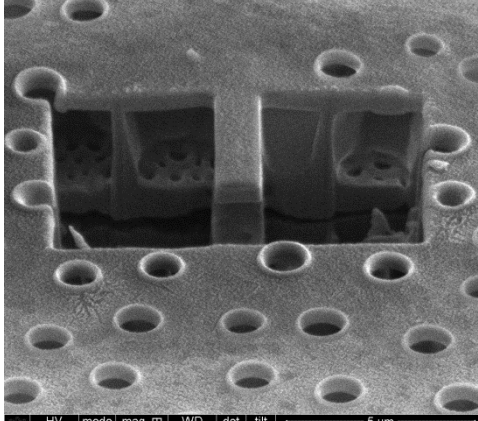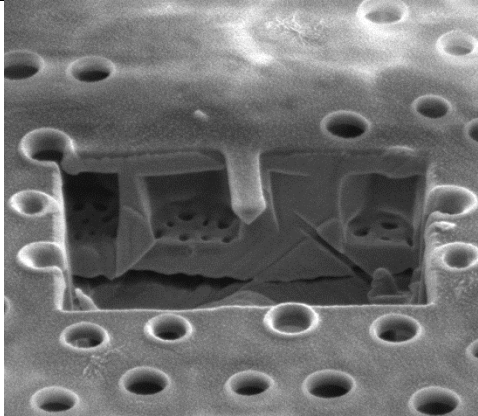
The milling of the sloped bottom was found to be more demanding. At this stage, the cantilever would often start to tilt in one or more direction, making it difficult to have a consistent slope along the length of the beam. This may be caused by surface stresses induced by the cleaning process or from the mechanical stresses involved with transferring of the frustules to the stubs. Another possibility is that the electron or ion beam adds enough energy in the form of heat to the system, causing the cantilever to distort. After a long session in the FIB, the sample holder would often have a higher temperature than its initial state, reinforcing this theory.
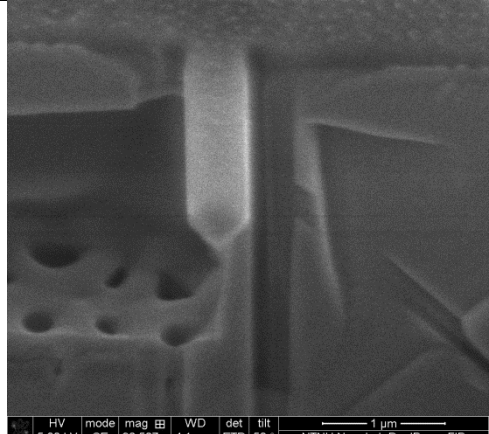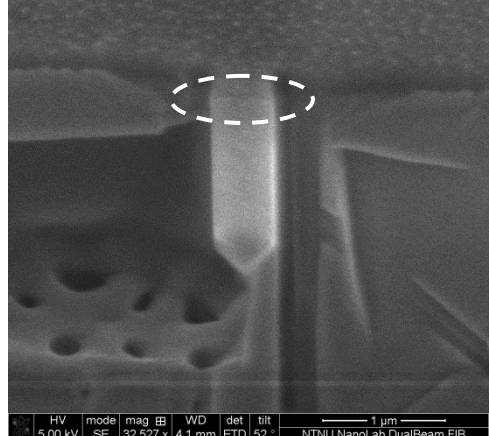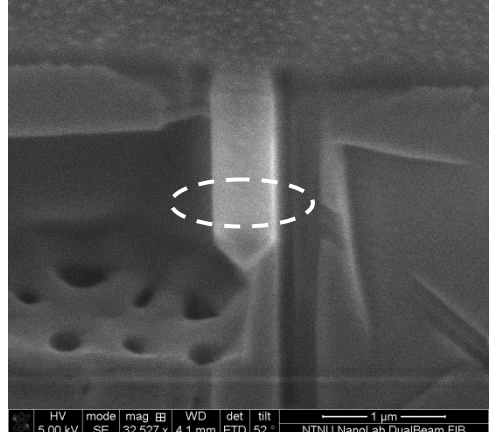
A technique applied to solve this issue was to only mill away the sides of the cantilever first, as seen in Figure 3.10. This resulted in a high accuracy when milling the sides, but the beam would curve during exposure to the ion beam and would often additionally curve upwards in a large degree when one of the ends was milled free. It was also more difficult to precisely control the shape of the cross section, as there was no visual aid before one of the ends was freed. If the beam was found to have inadequate cross section geometry, no adjustments could be performed due to the curvature, resulting in the need to start anew. As such, this technique was discarded after a couple of unsuccessful cantilevers.
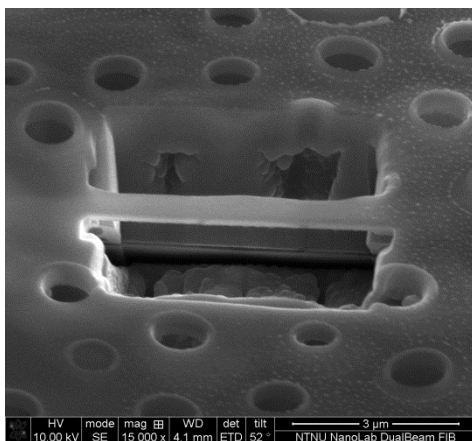
Figure 3.10: A cantilever constrained in both ends.

Table 3.2: The main steps of producing a cantilever.

	Step 1: Milling of crater
	Orientation: 90° with respect to the ion beam
	Pattern: A series of rectangles
	Typical size: Side rectangles: 3x5 µm
	Bottom rectangle: 1-1,5x1 µm
	Depth: z = 0,8 µm
	Beam voltage: 30,0 kV
	Beam current: 0,28 nA
	Step 2: Reducing the width
	Orientation: 90° with respect to the ion beam
	Pattern: Cleaning cross section
	Typical size: Depending on previous step, 1-1,5 µm
	Depth: z = 0,8 µm
	Beam voltage: 30,0 kV
	Beam current: 46 pA
	Step 3: Milling of angled surfaces
	Orientation: 45° with respect to the ion beam. One side was milled and then the specimen was rotated 180° in order to mill the other side
	Pattern: Cleaning cross section
	Typical size: From the edge of the beam to the end of the crater
	Depth: z = 0,8 µm
	Beam voltage: 30,0 kV
	Beam current: 26-46 pA

Step 4: Milling of the vertical sides and beam end

Orientation:	90° with respect to the ion beam
Pattern:	Cleaning cross section
Typical size:	Sides: small increments until the beam width is around 500 nm
	Beam end: milling until the length is three times the width of the beam
Depth:	z = 0,5 µm
Beam voltage:	30,0 kV
Beam current:	26 pA

Step 5: Milling of notch

Orientation:	90° with respect to the ion beam
Pattern:	Rectangle
Typical size:	10 nm x width of the beam
Depth:	z = 30 % of the height of the vertical sides
Beam voltage:	30,0 kV
Beam current:	1,5 pA

Step 6: Milling of indenter target

Orientation:	90° with respect to the ion beam
Pattern:	Two rectangles placed in a cross
Typical size:	10 nm x 50 % of the width of the beam
Depth:	z = 10-20 nm
Beam voltage:	30,0 kV
Beam current:	1,5 pA

43

The approach chosen was to mill one sloped side first, rotate the stub and then align the pattern to be as parallel as possible to the opposite side. The table was tilted 7 degrees from the horizontal axis, as this would yield a 45 degree slope. Due to the curvature of the cantilever, this approach will give some slight inaccuracies along the length of the beam, but it was deemed that it was most important to have a consistent cross section closest to the base of the cantilever. The pattern was therefore aligned at this position and then adjusted slightly to obtain a more accurate geometry along the beam. This procedure was repeated until a triangular cross section was formed, with a final cut taken on the original side in order to remove some of the redeposited material. The vertical sides were then milled one at a time with the first one serving as target geometry. The cantilever length was adjusted in accordance to the cantilever width.

The milling of the notch required more experimental approach. Due to the small size, it was nearly impossible to obtain an image with a high enough resolution to monitor the notch depth. Noise generated from the ion beam would also contribute to the inadequate image quality. One workaround was to mill a wider notch, but this would often result in an undesired shape with a still undefined notch depth. As Figure 3.11 shows, the notch would often have a blunt end with rather sloped sides. Another issue with this approach was that the larger pattern would cause more damage to the cantilever sides, causing it to have a smaller cross section over a larger area.
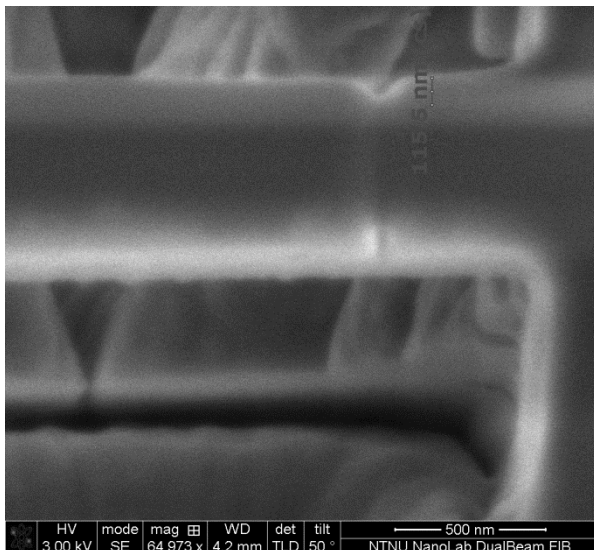
Figure 3.11: A milled notch with a depth interpreted to be 115,5 nm.

Additionally, the electron beam could not be used to generate an image directly from the side of the cantilever due to the limited table movement and risk of collision, further making the measurements of the notch depth more difficult. The ion beam could obtain such an image though, but this would also damage the cantilever, as described later in this chapter. As such, it was decided to have a smaller pattern and trust the ion beam to be accurate enough to mill the correct notch depth. Material redeposition would still be an issue, but by examining the fracture surface after the testing, an exact value of the notch was thought to be obtained.

The indenter target was milled in a similar way as the notch, but with a smaller depth. The reason for having a target was to increase the accuracy of the indenter tip during the testing, as it is hard to interpret the distances involved due to the tilted perspective.

One of the main challenges with the production of the cantilevers was the control of the ion beam. Due to the destructive nature of the beam, a live image feed could not be maintained for long, as this would result in the surface of the specimen being milled away. To overcome this obstacle, the beam was focused over an unimportant area and then aligned with the electron beam. Initially, to further reduce the damage, only the snapshot function was used to image the surface. However, after some instances where the ion beam milled the wrong area, it was discovered that the image would shift and stabilise after a few scans of the surface. The snapshot function only consisted of one scan, resulting in an image showing a different region than the area milled away. Often, this would only manifest itself when the operation required a high degree of accuracy, for instance when removing small amounts of material, as a small deviation would not be noticed during the initial steps. As such, the procedure was changed into letting the beam scan until the image stabilised. This was done with a dwell time of one microsecond and it was found that two to three complete scans were enough to obtain a stabile image feed. At this point, the scan was paused and the patterns were created. Control scans were subsequently performed and the patterns were adjusted if necessary.

This new procedure was not without flaws however, as the ion beam would continue to mill away material from other areas than where the pattern was located, as shown in Figure 3.12.
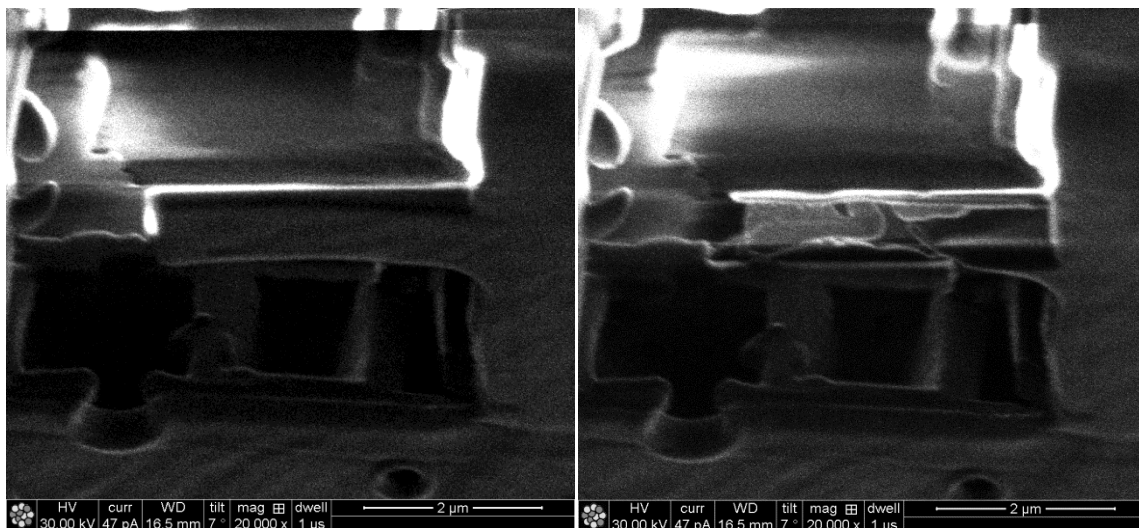
Figure 3.12:
To the left: A cantilever prior to the removal of what should have been a thin strip along the upper edge.
To the right: The resulting geometry. Before the patterning was started, it was checked multiple times that the pattern was located in the right place.

In retrospect, given the discoveries during the indentation, this may be caused by the charging of the sample, resulting in an incorrect representation of the frustule geometry. This will be discussed in section 3.3.2.

Redeposition of material was also found to be a problem, especially due to the layered structure of the frustule and the aforementioned noise generated by the ion beam. As seen in Figure 3.13, this could have a large impact on the finished cantilever. In that specific case, neither the notch nor the redeposited material could be seen during the session when the cantilever was produced. In the following session however, the geometry became very apparent and the cantilever was deemed unfit for testing.

This could have been prevented by producing a smaller cantilever, effectively removing the underlying structure so that material could not be trapped between the protruding areola sections. On the following cantilevers, the height of the end was compared to the thickness of the foramen layer. Although the thickness also gets affected by the redeposited material, this would at least provide some control over the material composition of the cantilever.

Six cantilevers were brought to testing, but only four of these had adequate geometry. Originally, a greater number was planned to be made, but the issues described above resulted in many failed cantilevers. Given that the milling process is time consuming, especially due to the precision required to mill out nanoscale dimensions, there was not enough time to make any more. The FIB was also very busy; being fully booked most of the time. A maintenance lasting two weeks further damaged the cantilever production.
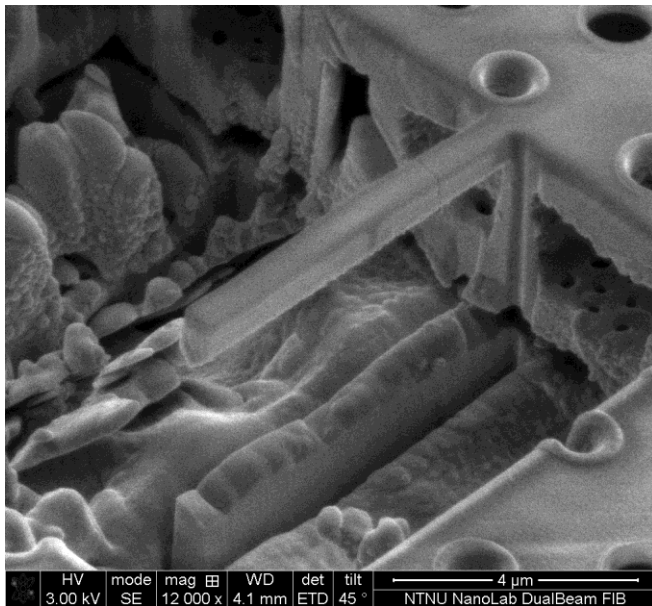
Figure 3.13: Material redeposition on a cantilever. The darker surfaces represents the frustule material, while the rest is material from the surroundings.

In addition to the measurements obtained during the fabrication process, additional measurements were acquired with the use of ImageJ.[59] This third-party image processing software was used both in order to save time, as well as to ensure that every dimensional size could be obtained in the event that some measurements were found to be missing or inaccurate.

3.3 Cantilever bending test

A Hysitron PI 85 SEM Picoindenter placed inside a FEI ESEM was used during the cantilever loading. The stage of the SEM had to be positioned correctly, as a wrong position would either result in a collision with the surrounding components in the SEM chamber or a poorly imaged experiment. Using data from previous tests, the stage parameters were set to; x = 0, y = -8, z = 35, R = -30 and T = 25, where R and T are the rotation and tilting of the stage, respectively. In order to see most of the material tested, a tilt angle of 45 degrees would be optimal. However, due to the decrease in accuracy of the picoindenter with tilt angles above 30 degrees and due to the limited space within the chamber, a 45 degree tilt is simply not practical. Such a tilt angle would also entail a greater working distance, which, as seen in Figure 3.14, was already quite large compared to what is normal for regular SEM imaging.

5/9/2015	det	x: -0.1878 mm	tilt	z	
1:34:31 PM	CCD	y: -8.2386 mm	25 °	35.0020 mm	

Figure 3.14: The inside of the SEM chamber with the picoindenter installed.

The material samples, placed on top of a stub, were mounted onto the picoindenter stage and then fastened so that the distance between the sample surface and the tip of the indenter was less than 2 millimetre apart. This had to be done prior to the installation of the indentation system inside the SEM chamber, as the opposite would result in little room to manoeuvre, as well as a greater risk of damaging the indenter tip.

A nanoindenter with a Berkovich tip was used during the testing, as it was believed that the tip would be sharp enough to be used on the nanoscale cantilevers. The initial tests were performed on the sample from a previous master thesis. This consisted of a test frustule with multiple cantilevers produced, as illustrated in Figure 3.15. Prior to the testing, it was important that the orientation of the cantilevers were known in order to properly mount the stub onto the picoindenter stage. If the

cantilever's lengthwise neutral axis was parallel to the tilt axis of the stage, the indenter tip would cover most of the image during testing, resulting in poor visual feedback. In order to prevent this, the stubs were marked on one particular side and mounted with this mark pointing in the appropriate direction.
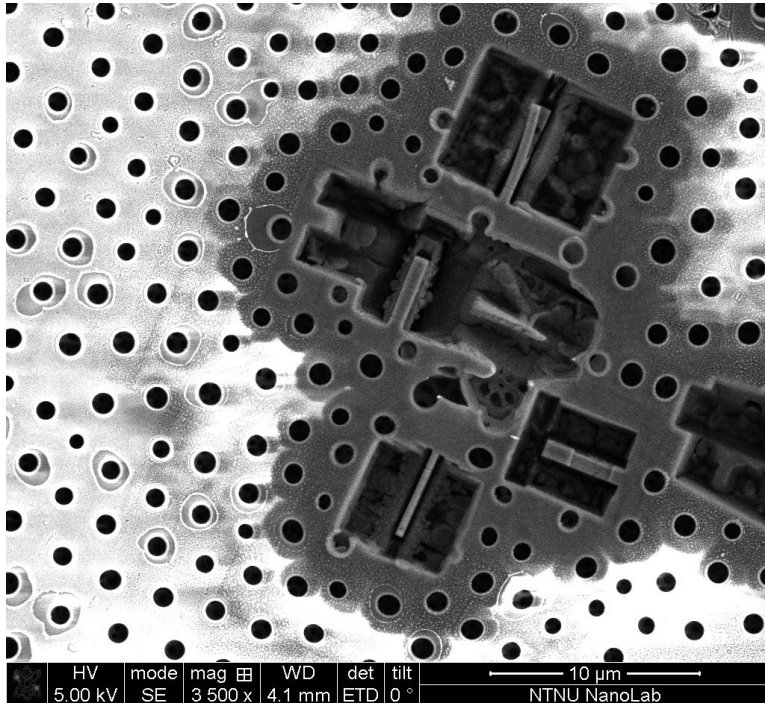
Figure 3.15: The cantilevers produced on the test frustule. The three oriented in the vertical direction were the focus of the testing, with the one in the centre having the correct geometry.

During the first session, it was found that the frustule was just out of reach of the indenter tip, as the stage only has a vertical and horizontal movement range of 1 mm in either direction from the initial position. However, the axis of indentation does not align perfectly with the centre axis of the installed stub, leading to a greater flexibility when the sample is located in the top left section of the stub. After some experimenting with the stub rotation, the frustule was placed correctly and it was discovered that as long as the sample was within a 3 mm radial distance from the centre of the stub, the indenter would be able to reach it. Due to the small size and lack of precise adjustments of the stub rotation, it is recommended to be as close to the stub centre as possible, because having the sample at the 3 mm distance leaves little room for error.

Any mistakes would result in demounting and adjusting of the picoindenter, which involves the ventilation and re-pumping of the SEM chamber, and would cost a noteworthy amount of time if the process needed to be repeated multiple times.

With the samples located on an AFM-plate, the mounting process was greatly simplified. When the samples were found to be outside the range of the indenter, the plate was merely adjusted on top of the stub for a more favourable orientation.

3.3.1 Test procedure

When the correct frustule was located and a good resolution had been obtained of the indenter tip, the indenter had to be brought into contact with the sample in order to accurately approach the frustules. This was done by having the indenter automatically approach the surface. The speed and sensitivity of the indenter were varied during the different approaches, with the most accurate approach employed closest to the cantilever. The different parameters can be seen in Table 3.3.

Table 3.3: Automated approach parameters used during the testing.

Indenter position	Step size [nm]	Velocity [nm/s]	Peak force [µN]	Withdrawal distance [nm]
Starting position, above an empty area close to the valve	200	5000	5	10000
Above the approximate centre of the valve	15	500	2	200
Close to the cantilever	10	50	2	100 - 200

The first approach was performed on an empty area in order to locate the surface of the stub, with the following approach performed on what was deemed to be an area that aligned horizontally with the centre of the valve. The sample stage was moved 3 µm away from the indenter in order to avoid collision with the valve edge and then moved horizontally until the indenter was above the approximate centre of the valve. The next approach was then performed. The sample stage was subsequently moved to an area that horizontally aligned with the cantilever, wherein the final approach was executed. This process is illustrated in Figure 3.16. A trial indentation was also performed at this location. This was done in order to confirm that the indentation parameters were correct and yielded stable results.
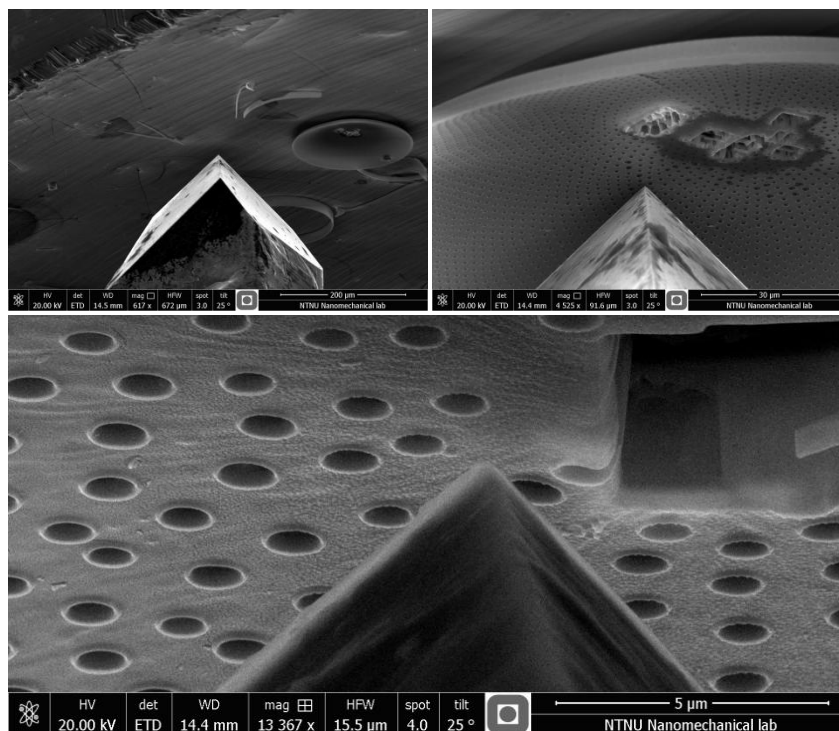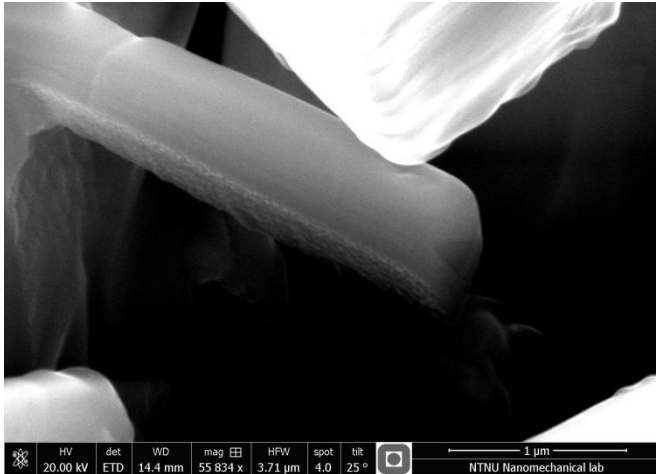

Figure 3.16:
Top left: Initial indentation close to the valve.
Top right: Indentation close to the centre of the valve.
Bottom: Indentation on the area deemed to be on the same level as the cantilever.

After the indenter had been positioned near the indentation mark, it was brought closer to the surface to see if the tip was properly aligned. Unlike previous movements, this was not done by moving the picoindenter stage, but rather by extending the indenter. As the stage often suffers from jolting movements, this was more easily controlled and resulted in a very accurate approach. It was found that when adjusting the stage to the final position, small increments in the movement resulted in very little jitter. The indenter tip prior to loading can be seen in Figure 3.17.

Figure 3.17: Correct positioning of the indenter tip.

An image frame grabber was used to create videos of the SEM images during loading. The resolution was limited due to the large working distance and the material tested. It was therefore necessary to use a slow scan rate and in some cases the "average filter" in order to reduce the image noise.

During the loading of the cantilevers, displacement control was used. The different parameters applied can be seen in Table 3.4, with the first four parameters regulating the process. The Q-parameter is not native to the indentation setup, but stabilizes the indenter during the entire session. In the initial tests, the Q-control parameter and number of data point were set to 0,08 and 200 pts/s respectively, but this yielded results with a high degree of noise and was adjusted in the following tests. A comparison between two experiments run with the different parameters can be found in Appendix E. It was also observed that whether one only activated the Derivative Gain or the Adaptive Gain, or if both were activated, the result would be very similar. Thus, during the tests, only the Derivative Gain was activated.

Table 3.4: The displacement control parameters used during the indentations.

| Displacement control parameter	Input
Proportional Gain (P)	0,07
Integral Gain (I)	0,30
Derivative Gain (D)	0,07
Adaptive Gain (A)	*0,50*
Velocity [nm/s]	10
Data points [pts/s]	100
Indentation depth [nm]	Varies
Q-control	0,20

3.3.2 Observations and issues during testing

During testing, one of the three cantilever valves on the AFM-plate attached itself to the indenter tip during the first approach to the surface. It is believed that the valve was of insufficient size, resulting in a too small contact area between the valve and the substrate. This was partially solved by gently moving the indenter stage horizontally and vertically until the valve reattached itself to the substrate, with subsequent adjustments moving the valve until the centre was deemed to be stable.

The indenter was then moved closer to the centre, where it was observed that the SEM image started to shift upwards or downwards whenever the focus was adjusted. This behaviour would stabilize after a while, but would start anew whenever adjustments were made or when the stage was moved, making testing impossible. This effect is illustrated in Figure 3.18.
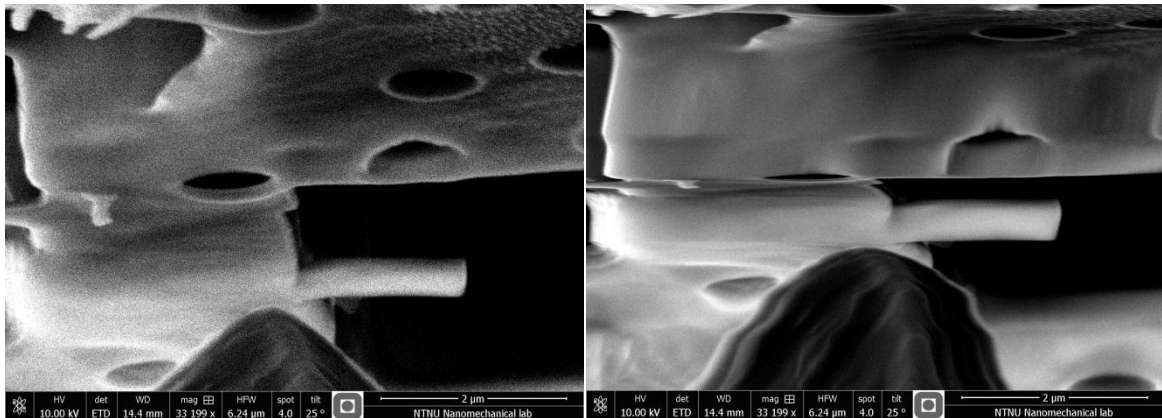
Figure 3.18: Charging effects of the cantilevers. The images are obtained with the same focus, with the left image having a dwell time of 3 μs and the right image having a dwell time of 30 μs.

Due to time limitations, the equipment was dismounted. During the next session, it was observed that the valve had detached from the substrate, with only traces from the FIB indicating its previous position, as depicted in Figure 3.19.
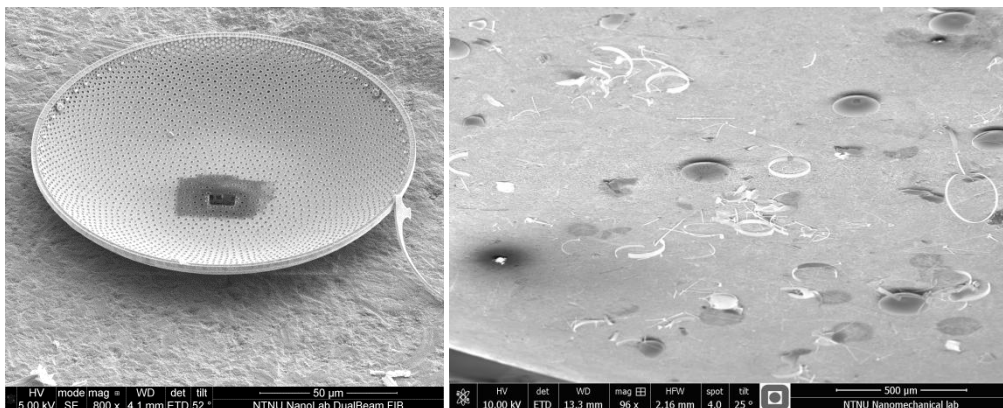
Figure 3.19:
To the left: The detached valve, as seen in the FIB after the cantilever had been created.
To the right: The area indicating where the valve had been located, given by the bright surface close to the left edge. This is the milled section underneath the crater, which, given the superior conductivity of the metal plate, yielded a stronger signal.

The other cantilevers on the AFM-plate also suffered from charging effects. Initially, it was unclear what caused this, so a troubleshooting process was commenced. The indenter tip was cleaned in

order to remove what was thought to be residue from the contact with the detached valve, as this could be the source of the current charging effects. When this yielded no improvement, it was decided to switch from high-vacuum mode to low-vacuum mode in order to see if the usage of water vapour as a signal medium would remedy the situation.

The stage was moved away from the indenter to avoid collision during the time it took to pressurise the chamber. However, during said operation, vibrations were introduced into the system, causing the indenter to touch the surface of the valve, ruining the cantilever. The valve and the indenter tip with the ruined cantilever structure are depicted in Figure 3.20.
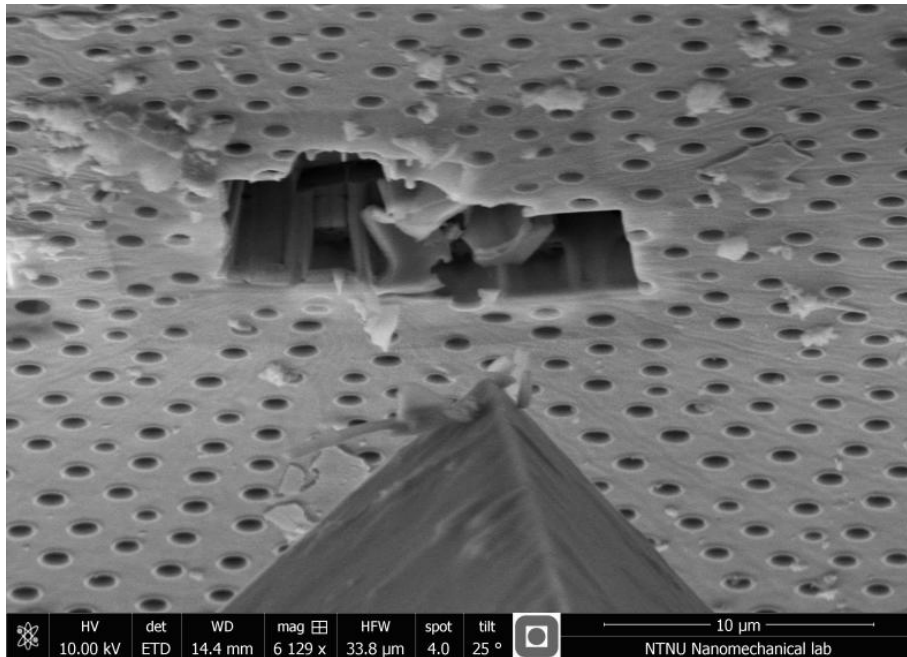
Figure 3.20: Indenter tip with the broken cantilever attached to it.

When a new layer of 10 nm protective coating was applied on the remaining valve, the effect was greatly reduced. It is believed that the FIB had removed the original coating from the areas surrounding the cantilever during the fabrication process, resulting in charging effects from the nonconductive biosilica. Another cause may be that the original coating was not applied properly, but this was dismissed as no such issues were experienced in the FIB. The testing of this last cantilever was completed without any issues.

3.4 Study of the fractured surface

Following the bending test, the fractured surfaces were studied. This was performed in the SEM right after the material testing, as well as with a Veeco diMultiMode V AFM. Prior to the SEM study, the samples were removed from the indentation system and placed in a conventional stub holder. Due to limitations in the working distance of the instrument, only the samples mounted on the AFM-plate could be studied in the AFM. The frustules were located using the built-in microscope, with the movement of the AFM-tip doing the finer adjustments. Tapping-mode was applied in order to not cause damage to the structure.

3.5 Finite element analysis of the fractured cantilever

This section is heavily based on the results from the bending tests, so it is recommended that the contents of sections 4.3 to 4.5 is known before reading through this chapter.

3.5.1 Material properties

The material properties were initially chosen as the same values from the geometry factor study, but adjustments needed to be made in order to match the experimental results. By incrementally adjusting the Young's modulus until the deflection at the loading area matched that of the indenter tip, a final value could be obtained. This process was done in accordance with equation (3.1), where E is the Young's modulus, u_n is the deflection from the analysis and u is the target deflection from the experimental data.

$$E_{n+1} = E_n * \frac{u_n}{u}$$

(3.1)

3.5.2 Geometry and mesh

As with the previous model, Siemens NX was chosen for the creation of the model, while Abaqus was used to run the analyses. Since the test specimen was the very same which was used as a basis for the model in the geometry factor study, the model was modified to fit with the updated values. The surrounding structure was left identical, but a new cantilever was formed in accordance to the measured values and the results from the bending test. One example of this can be seen in Figure 3.21.
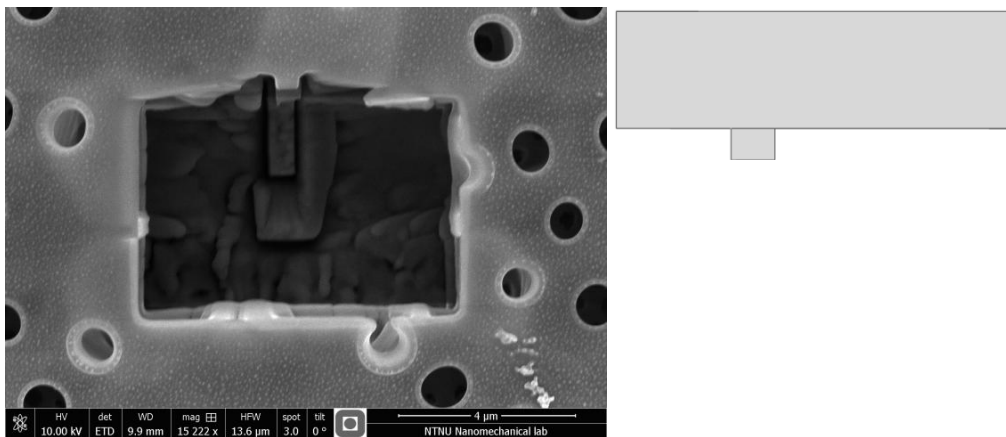

**Figure 3.21: The remains of the cantilever and how it was modelled.**

In some areas, the model had to be simplified in order for it to run properly in Abaqus. The crack area is a prime example of this. Due to Abaqus needing either brick or wedge elements at the crack tip in order to compute fracture mechanics parameters, the fractured surface had to be represented with a simpler geometry, as shown in Figure 3.22.
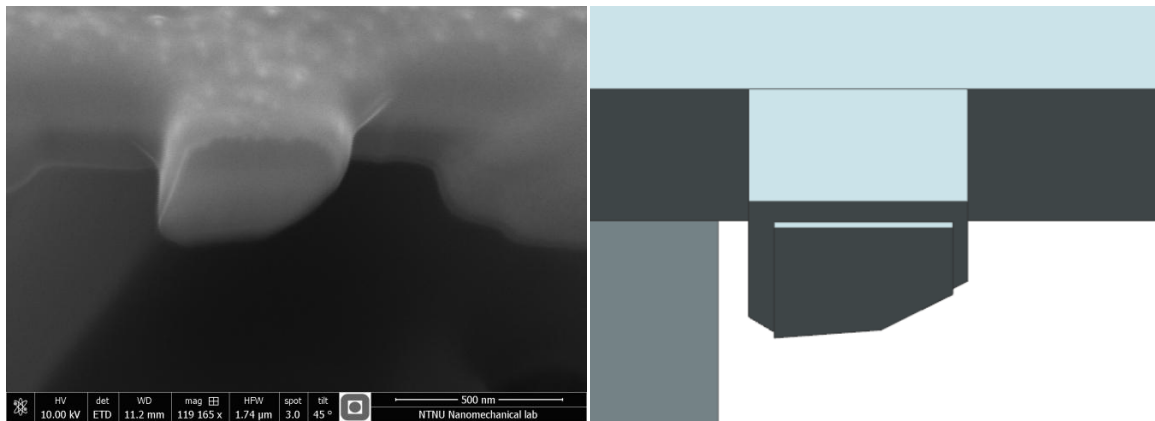
Figure 3.22: Comparison between the fractured surface and the geometry modelled in NX.

The general uncertainty around the exact dimensions of the cantilever was also a problem, but this was solved by using the fractured surface and the cantilever end dimensions as a reference for the rest of the cantilever. Since the patterns used in the FIB during the manufacturing process only consisted of rectangles, a linear relation was assumed to exist between the surface around the notch and the edges on the cantilever end. The deflection data was used to determine how much the cantilever was sloped prior to the deformations, as the vertical distance between the initial loading position and the base of the cantilever was known from the bending test. By using the horizontal distance from the loading position to the notch and the total horizontal length of the cantilever, the total difference in height between the end of the cantilever and the base of the cantilever could be calculated by the use of a linear relation. This distance was found to be 938 nm. Surfaces were created between the notch area and the cantilever end, as displayed in Figure 3.23.
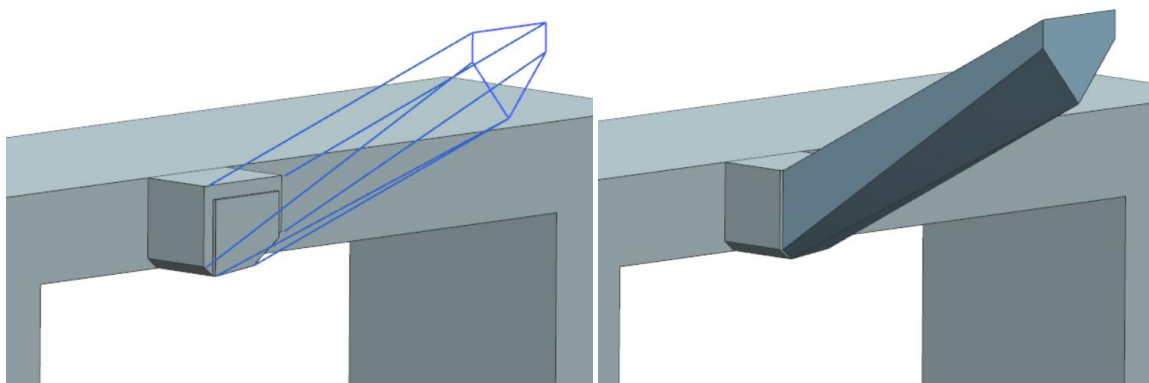
Figure 3.23: The creation of the geometry between the fractured surface and the end of the cantilever.

The model was exported by the use of the Iges-format and a 10 nm fillet was placed in the notch in Abaqus after the model had been imported. As usual, it had to be scaled by a factor of 10^{-6}. The finished model is displayed in Figure 3.24, with Table 3.5 showing the characteristic dimensions.
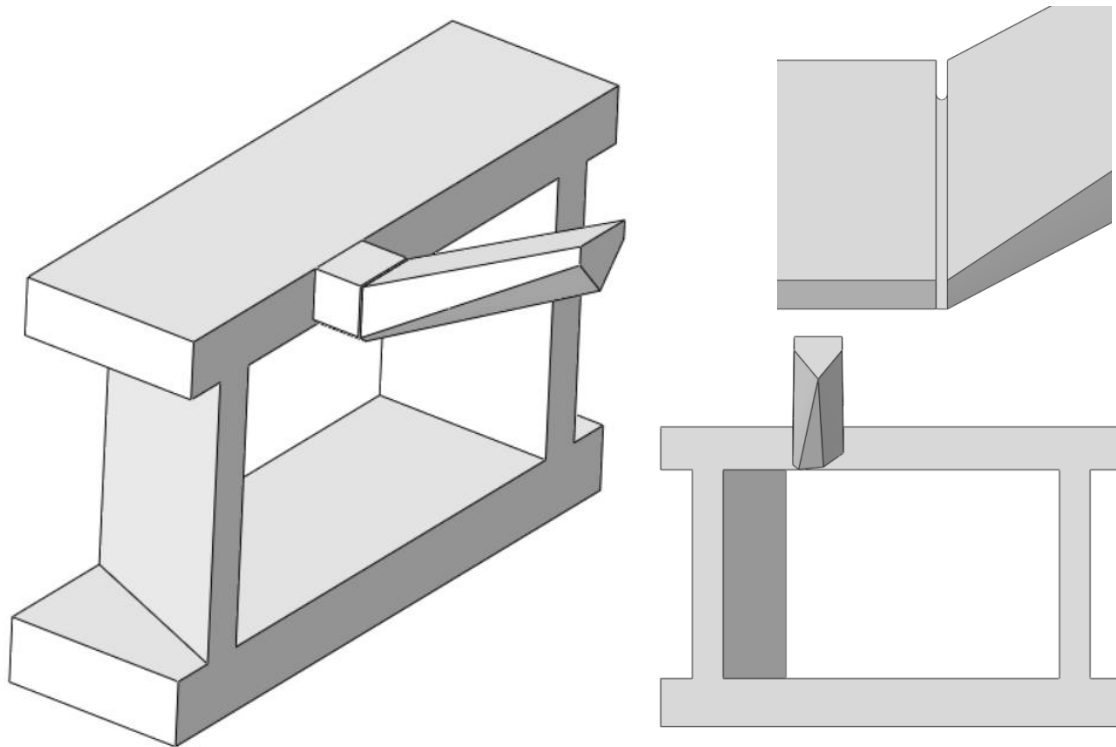
Figure 3.24:
To the left: The finished cantilever model.
To the right: Top picture displays the rounded notch created in Abaqus, while the bottom picture displays the model as seen from the front.

Table 3.5: The characteristic dimensions of the cantilever model.

| Aspect	Size at notch [nm]	Size at end [nm]
Cantilever width, w	526	498
Height of the vertical sides, h	391 / 269	143
Maximum height, h_{tot}	442	441
Horizontal loading distance, L	1400	
Notch length, a	70	
Notch width	20	
Cantilever width, notch	429	
Cantilever length, horizontal	2180	
Height difference, base/end	938	
Cribrum thickness	500	
Foramen thickness	445	
Areola height	2165	
Areola thickness	320	

The analyses were performed with 10 contours active for every element group along the notch width in order to save time. Of the fracture mechanics parameters, only the J-integral output was activated. The nonlinear solver was activated as the model would experience large deformations,.

C3D20 elements with reduced integration points were chosen as the main element type. However, due to the advanced geometry, ten node tetrahedral elements, C3D10, had to be used on the extruding end of the cantilever. When trying to solely model the cantilever with brick elements, the mesh would be distorted from the notch to the end of the cantilever. In order for the two element types to be compatible, the nodes were tied at the contact areas, resulting in a fused region. Since

very little deformation would occur at the transition area, this would have a negligible impact on the accuracy. The mesh on the surrounding structure was kept quite coarse, having a size of approximately 200 nm, while the mesh was refined on the cantilever. The general mesh size at this location ranged from approximately 100 to 30 nm while the mesh surrounding the notch was refined from 6 to 3 nm in order to check if the results converged. The entire mesh is displayed in Figure 3.25, with Figure 3.26 illustrating the difference in mesh size around the notch.
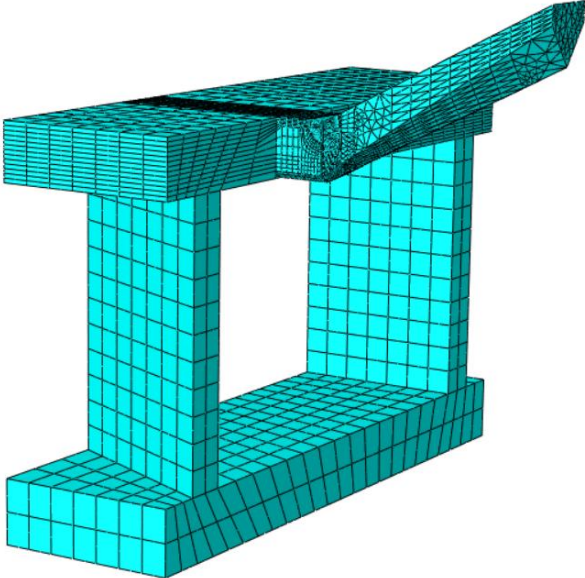
Figure 3.25: Mesh of the entire model. A very coarse mesh was placed on the bottom half of the surrounding structure, as it will not yield any interesting results, nor will it be deformed during the analyses.
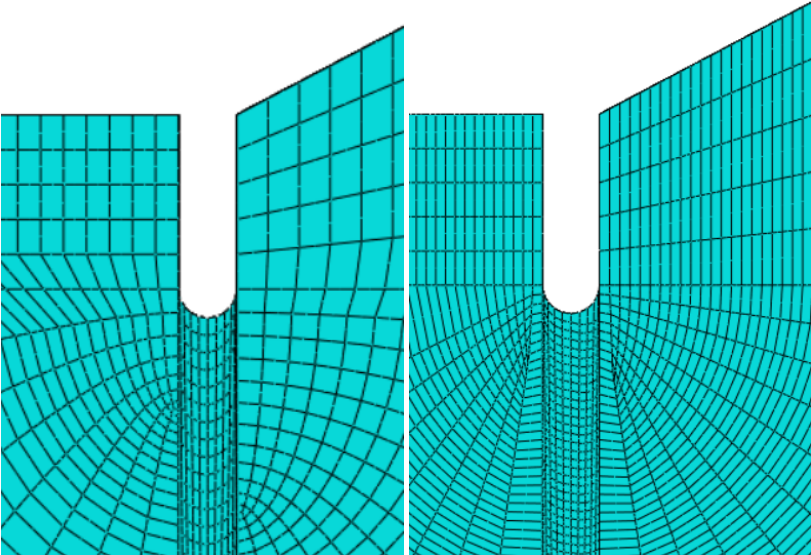
Figure 3.26: Mesh refinement of the notch.

A second model was also created based on the analysis results of the model with the finest mesh. This new model was exported from the deformed parent model when the loading area had reached the same level as the top surface of the foramen layer. This model is displayed in Figure 3.27.
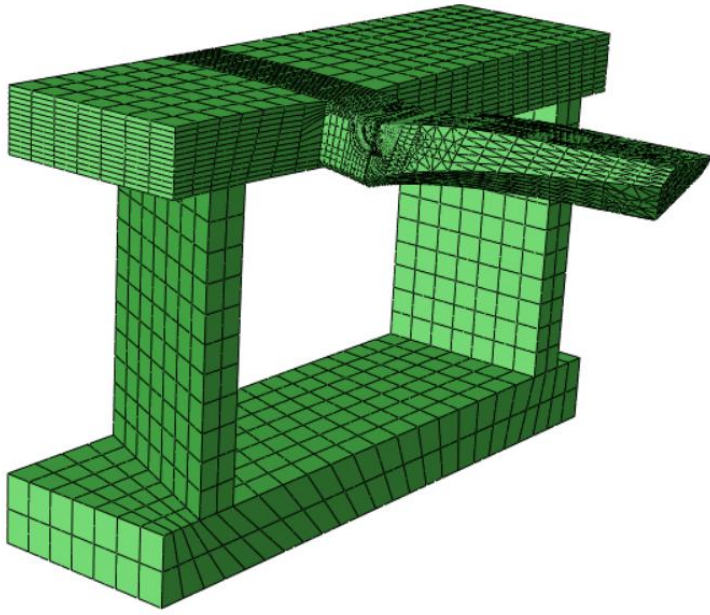
Figure 3.27: Mesh of the pre-deformed model.

3.5.3   **Loading and analysis end conditions**

For the original model, the load was set to 28,65 µN, the values given by the secant from Figure 4.22. In the initial analyses, the load was distributed around an area at a horizontal distance of 1500 nm from the notch. After the first iteration, the point corresponding to the distance of 1400 nm from the notch was located and the load was placed here. By doing this, the load could be placed very precisely at the point corresponding to the indentation area at the point of fracture. The two areas can be seen in Figure 3.28, with a distributing coupling used to distribute the force across the loading area. For the deformed model, the exact same load distribution was kept, but the load was changed to match the load at fracture. In this scenario, the use of a secant was disregarded as this was a study of the possibility that no crack growth had occurred. The load was thus set to 7,73 µN. The models were constrained in accordance to Figure 3.29.
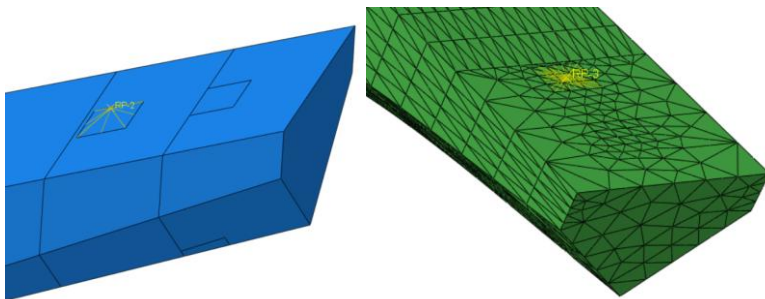

Figure 3.28: Load distributions for the two models. The second square surface on the top of the cantilever represents the initial loading position.
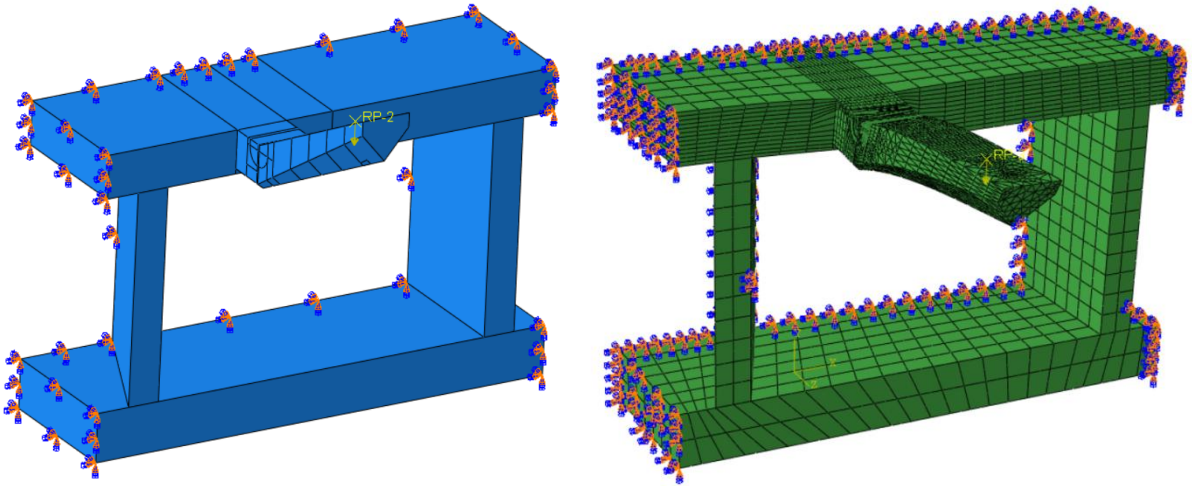
57

Figure 3.29: Boundary conditions of the models. The blue and orange arrows represent encasement, meaning no degrees of freedom, while the yellow arrows represent the loads applied.

Based on the results of the bending test, each model had a target deflection value at the point of loading. For the pre-deformed model, this was the remaining indenter displacement prior to fracture. For the full model, the value needed some adjustments. The value given from the secant was from the original loading position, while the value used in the model had to be from the adjusted position. The height difference between the two positions was therefore subtracted from the secant value. The resulting target deflections can be found in Table 3.6.

Table 3.6: End conditions for the analyses

| Model	Original target value [nm]	Adjusted target value [nm]
Full	987,8	837,8
Pre-deformed	527	-

4 Results

In this chapter, the results from the numerical simulations, cantilever fabrication process and material testing will be presented. Explanations will be given where appropriate, but the discussion will be kept to a minimum as that will be covered in section 5.

4.1 Geometry factor analysis

4.1.1 J-integral and the stress intensity factor

The different behaviour of the J-integral and stress intensity factor were analysed on the model with a sharp notch. The results for the stress intensity factor can be seen in Figure 4.1, while typical results for the J-integral are displayed in Figure 4.2.
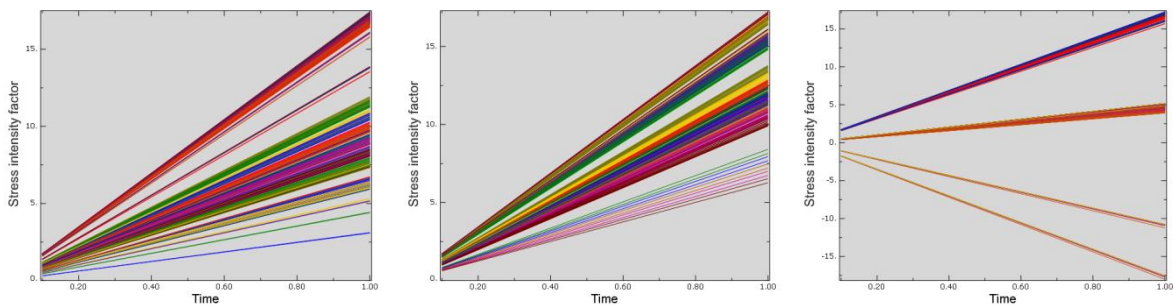
Figure 4.1: The stress intensity factor development as calculated directly during the analyses. The mesh size has been refined from 4,7 nm to 2,6 and 1,6 nm, with the size decreasing from left to right.
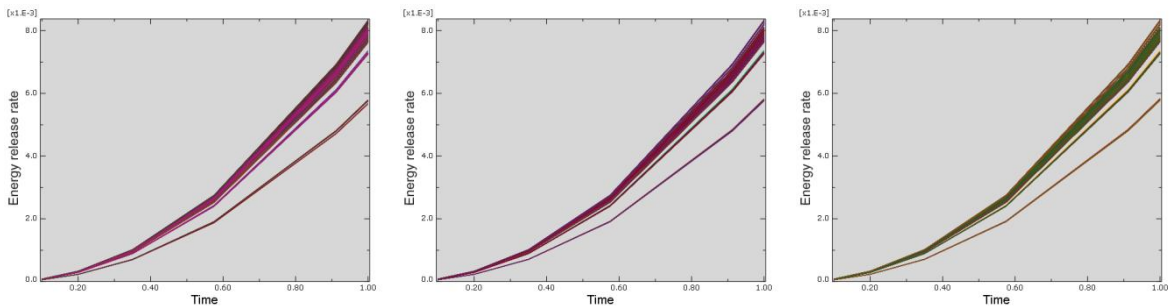
Figure 4.2: J-integral curves from the mesh refinement analyses. The mesh size has been refined from 4,7 nm to 2,6 and 1,6 nm, with the size decreasing from left to right.

By using equation (2.5), a comparison was made between the upper curves in Figure 4.1 and an average value of the clustered J-integral curves, with the results displayed in Table 4.1.

Table 4.1: Comparison between the K from the J-integral and the K taken directly from Abaqus.

Mesh size [nm]	K_I from Abaqus [MPa√m]	J-integral from Abaqus [N/mm]	K_{IJ}, calculated from J [MPa√m]
4,7	0,5389	0,00790	0,5396
2,6	0,5434	0,00795	0,5413
1,6	0,5406	0,00792	0,5403

It was also found that the surrounding structure was more or less unaffected by the deformations, confirming the assumption made when creating the model. Images of the deformed model, as well as additional J-integral curves can be viewed in Appendix A.

4.1.2 Convergence study – sharp notch

By varying the mesh size around the notch from 4,7 nm to 1,6 nm, the graphs depicted in Figure 4.3, Figure 4.4 and Figure 4.5 were obtained.

Figure 4.3: Maximum stresses as a function of the element size.

Figure 4.4: Maximum deflection as a function of element size.

Figure 4.5: J-integral as function of element size.

4.1.3 Convergence study – rounded notch

By varying the mesh size around the notch from 6,6 nm to 3 nm, the graphs depicted in Figure 4.6, Figure 4.7 and Figure 4.8 were obtained.
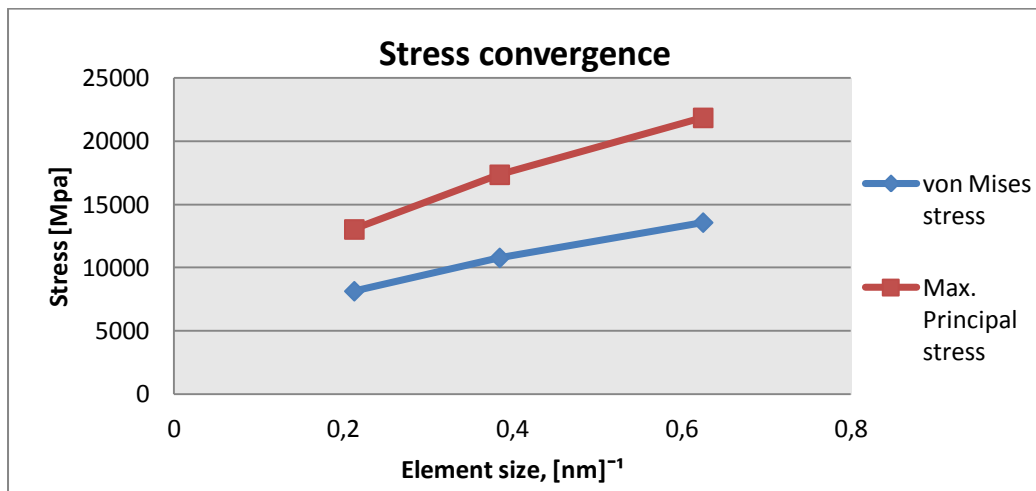

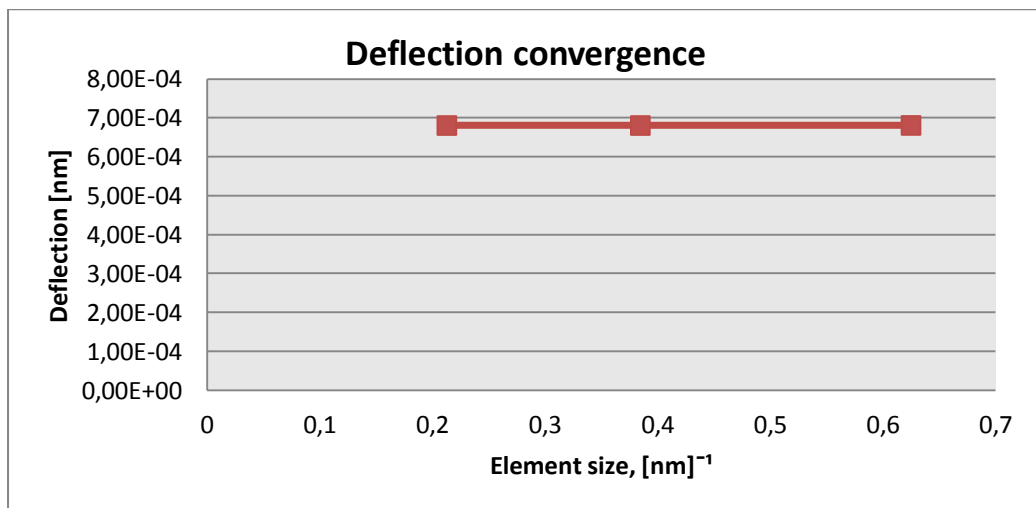**Figure 4.6: Maximum stresses as a function of the element size.**

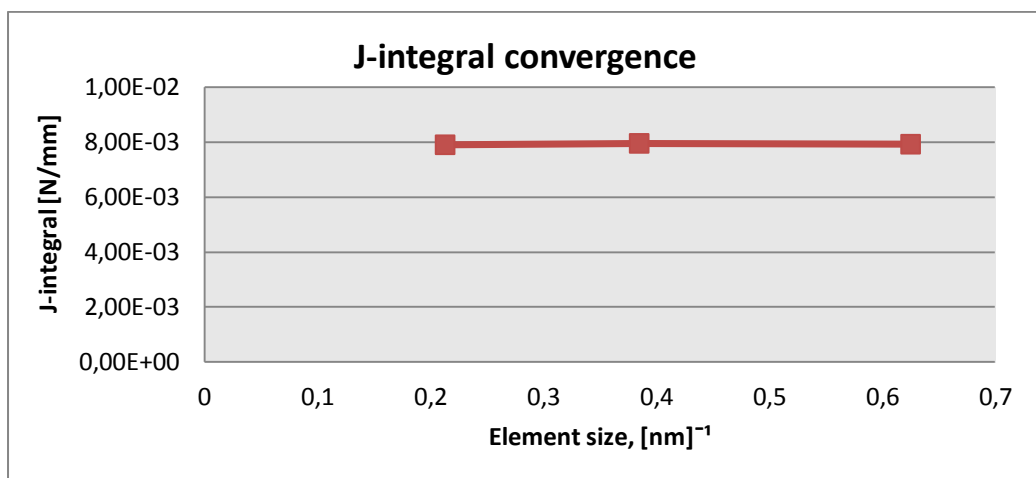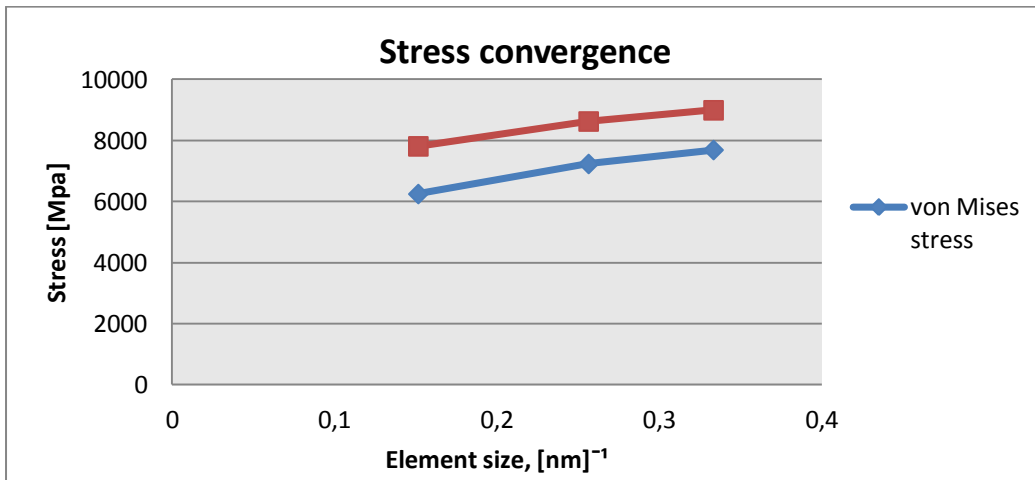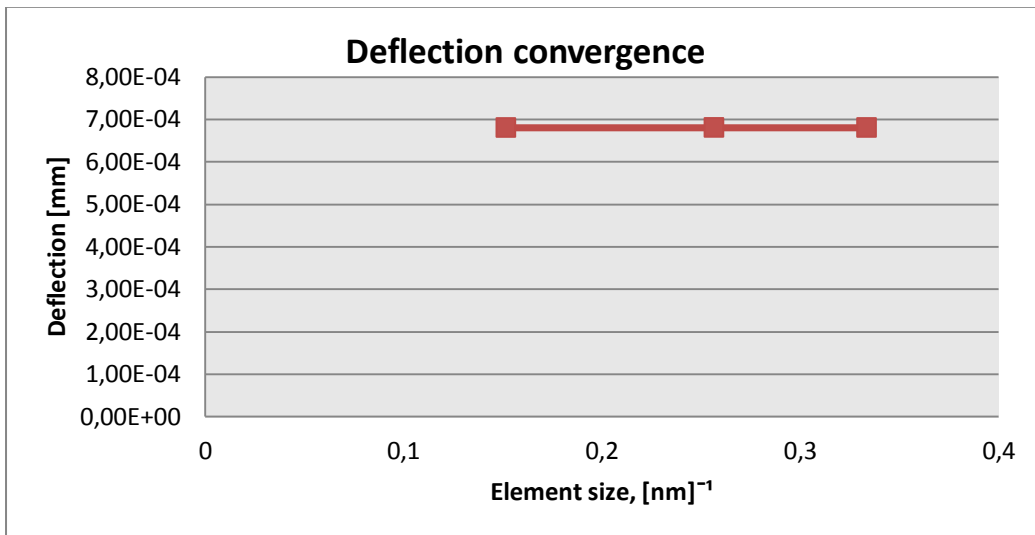**Figure 4.7: Maximum deflection as a function of element size.**
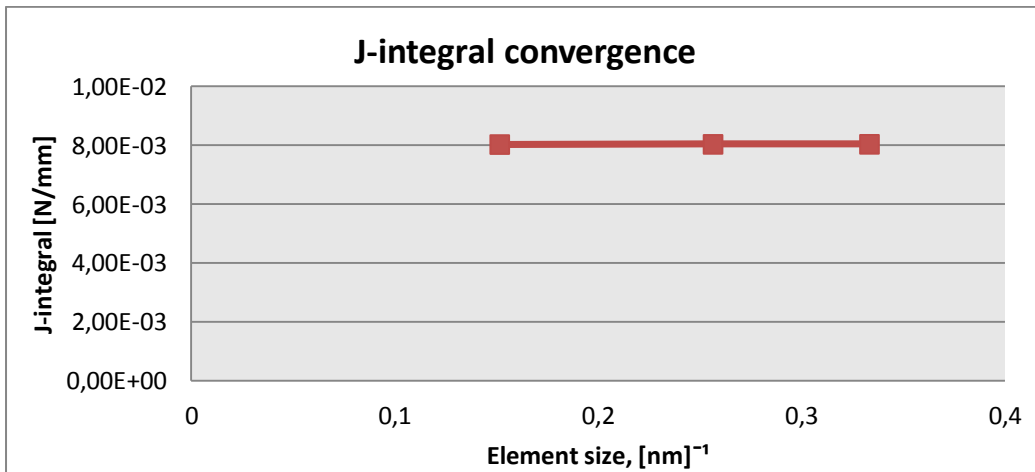
Figure 4.8: J-integral as function of element size.

4.1.4 Notch elongation analysis

During the notch elongation analyses, a mesh size of 4 nm was chosen around the crack tip. The notch was set to be 31, 42 and 50 % of the height of the vertical sides. The resulting J-integral numbers were inserted into equation (2.5). The outputted stress intensity factor were used to obtain values of *f(a/h)* from equations (2.2) and (2.6), which were compared to the a/h-ratio. The resulting factors are illustrated Figure 4.9 and listed in Table 4.2.
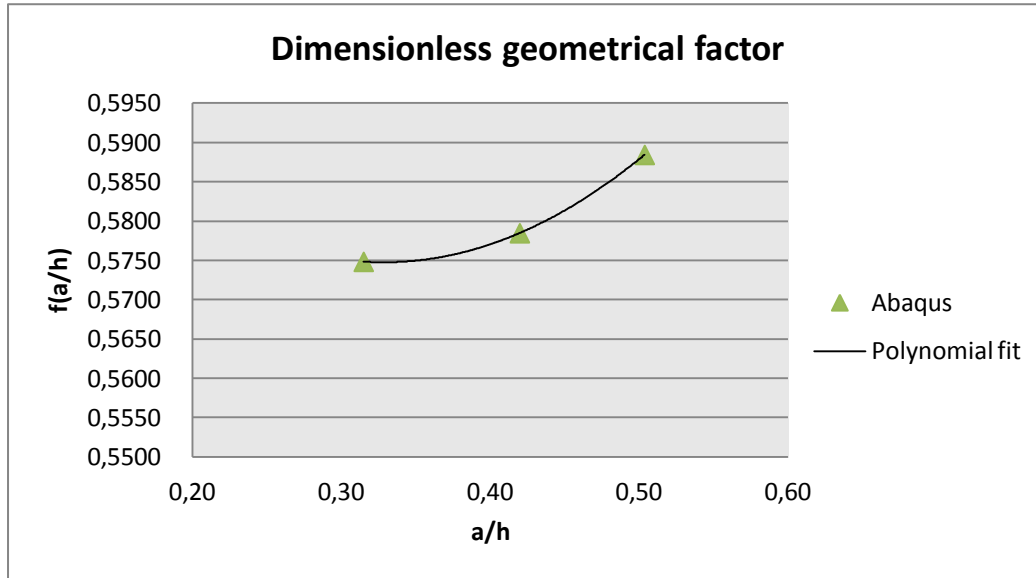
Figure 4.9: The calculated geometry factor as a function of the a/h ratio.

Table 4.2: The calculated geometry factor.

a/h	f(a/h)
0,31	0,57
0,42	0,58
0,50	0,59

Based on these results, a polynomial curve was fitted to the data points, with the resulting expression given in Equation (4.1). This expression is only valid for a/h ratios between 0,30 and 0,50, as there was not performed any tests outside this range.

$$f\left(\frac{a}{h}\right) = 0{,}6227 - 0{,}2923\left(\frac{a}{h}\right) + 0{,}4453\left(\frac{a}{h}\right)^2 \qquad (4.1)$$

4.2 Cantilever geometry

The results of the cantilever production can be seen in Table 4.3. Images of all the cantilevers tested can be found in Appendix B, while Appendix C holds images of untested or unsuccessful cantilevers.

Out of the six cantilevers tested, three were made from the old samples. Two of these, Cantilever 1 and 2 had poor geometry and were used for practice. Cantilever 3.1 had a triangular cross section, as it was thought it would be too slender if a pentagonal cross section was produced. Based on the results from the testing, modifications were done to the cantilever, resulting in Cantilever 3.2. This was made shorter and the sides were milled in order to create a pentagonal cross section. Three new cantilevers, all placed on an AFM-plate, were also created after this initial testing session.

Table 4.3: Cantilevers tested with the picoindenter, with their characteristic sizes. Cantilever 1 and 2 had poor geometry, making any measurements irrelevant for the calculations. Cantilever 3.1 had a triangular cross section, which was later changed. The total height is the distance from the top surface to the pointed bottom of the cantilever.

Cantilever number	Height, h [nm]	Width, w [nm]	Loading length, L [μm]	Notch depth, a [nm]	Total height, h_{tot} [nm]
1	-	-	-	-	-
2	-	-	-	-	-
3.1	-	680	2,77	95	575
3.2	266	620	1,99	80	620
4	143	498	1,50	45	441
5	163	530	1,50	50	485
6	95	385	1,16	30	341

4.3 Cantilever bending test

During the practice testing of Cantilever 1 and 2, it was observed that no forces were being recorded during loading. This was concluded to be caused by the cantilever's being too slender. By decreasing the loading distance, a load-displacement curve could be obtained, but this would suffer from both the irregular shape and the inaccurate location of the loading point. The results from these experiments can be found in Appendix D.

The loading of Cantilever 3.1 was also not done without problems. The deflection was far greater than expected, leading to contact with the bottom of the crater. The resulting load-displacement curve is displayed in Appendix D. This was corrected in the FIB by further increasing the size of the crater and the cantilever was also adjusted to have a pentagonal cross section.

The results from the loading of the adjusted Cantilever 3.2 are depicted in Figure 4.10. It was found that when the cantilever was loaded at the end on the indentation mark, the excessive deflection resulted in what appeared to be contact with the side of the indenter tip.
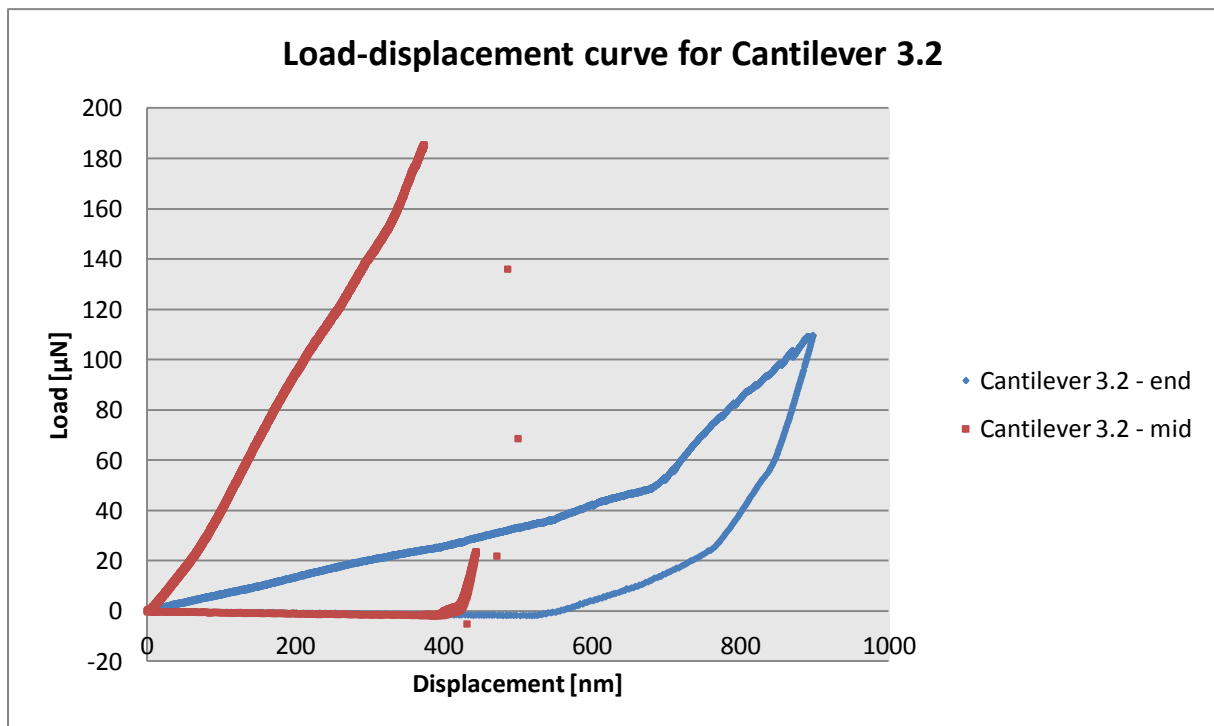
Figure 4.10: Load-displacement curves for Cantilever 3.2.

In the next test, the indenter was moved to approximately half loading distance. This resulted in a fracture at the base of the cantilever. Both the point of loading and the fractured cantilever can be seen in Figure 4.11.
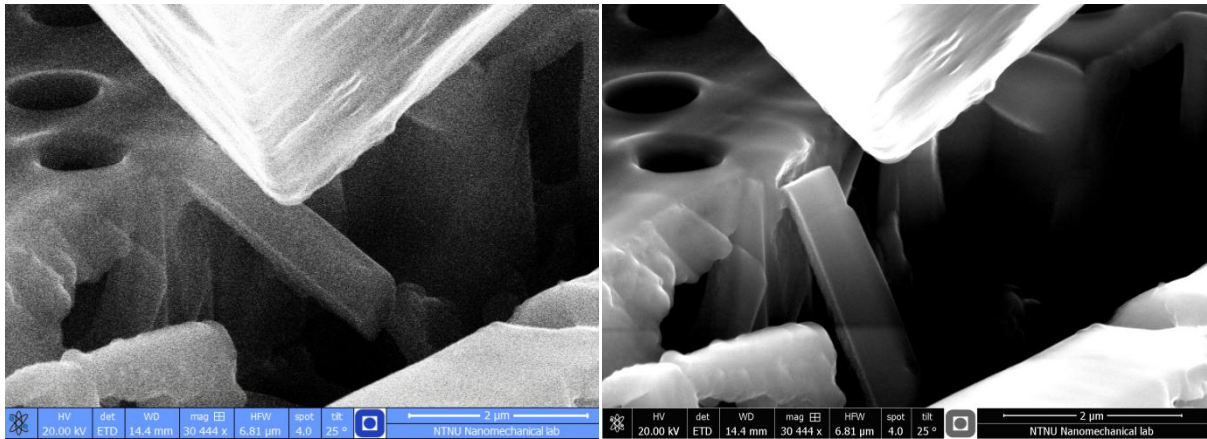
Figure 4.11:
To the left: Mid-length loading position of Cantilever 3.2. The image was acquired at the point of contact.
To the right: Cantilever 3.2 after fracture had occurred.

However, prior to the test, it was observed what appeared to be a significant amount of redeposited material surrounding the original material. As shown in Figure 4.12, the biosilica only makes up for the centre of the cantilever
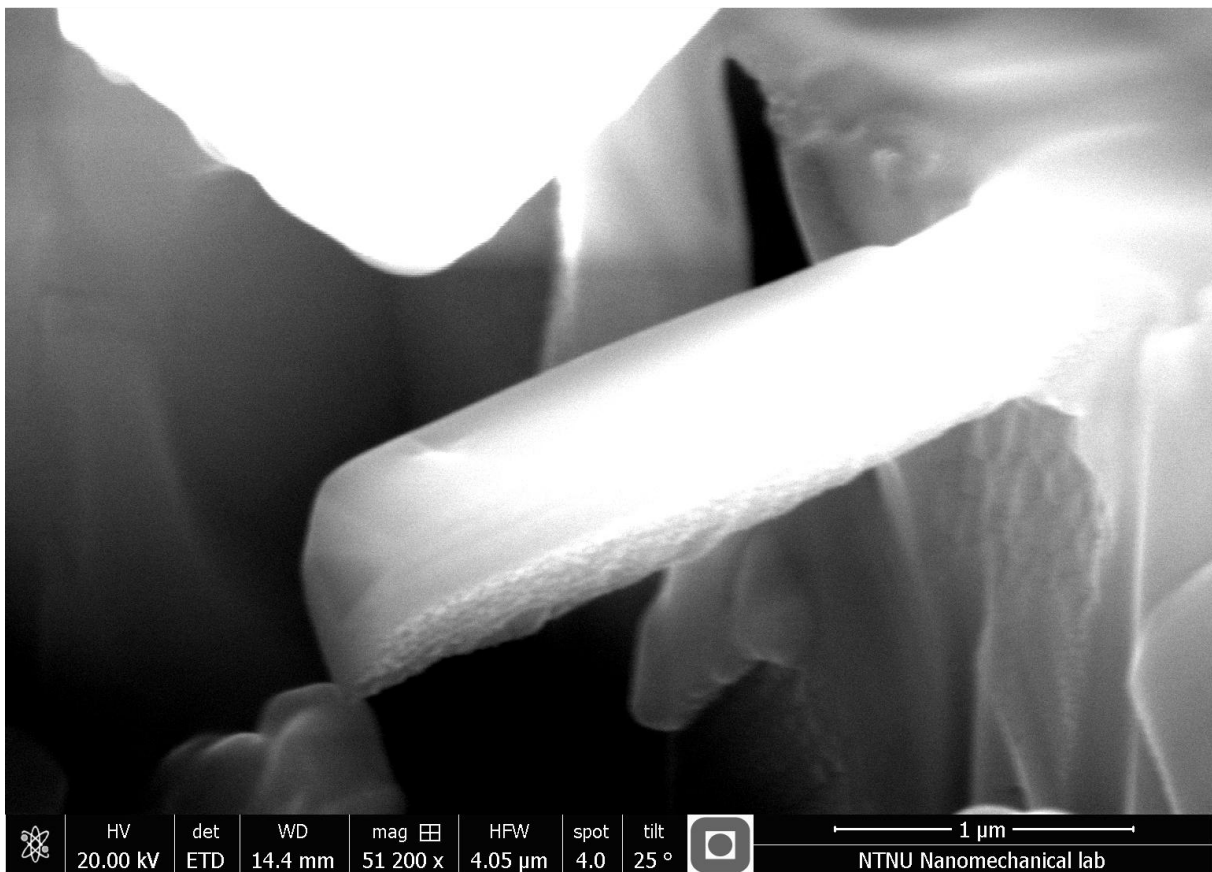
Figure 4.12: Redeposited material on Cantilever 3.2. Only the darker area at the very centre is from the original cantilever, with the rest being redeposited from the material that had been milled away.

The results from the loading of Cantilever 4 can be seen in Figure 4.13, with images of the cantilever both pre- and post-loading being displayed in Figure 4.14.
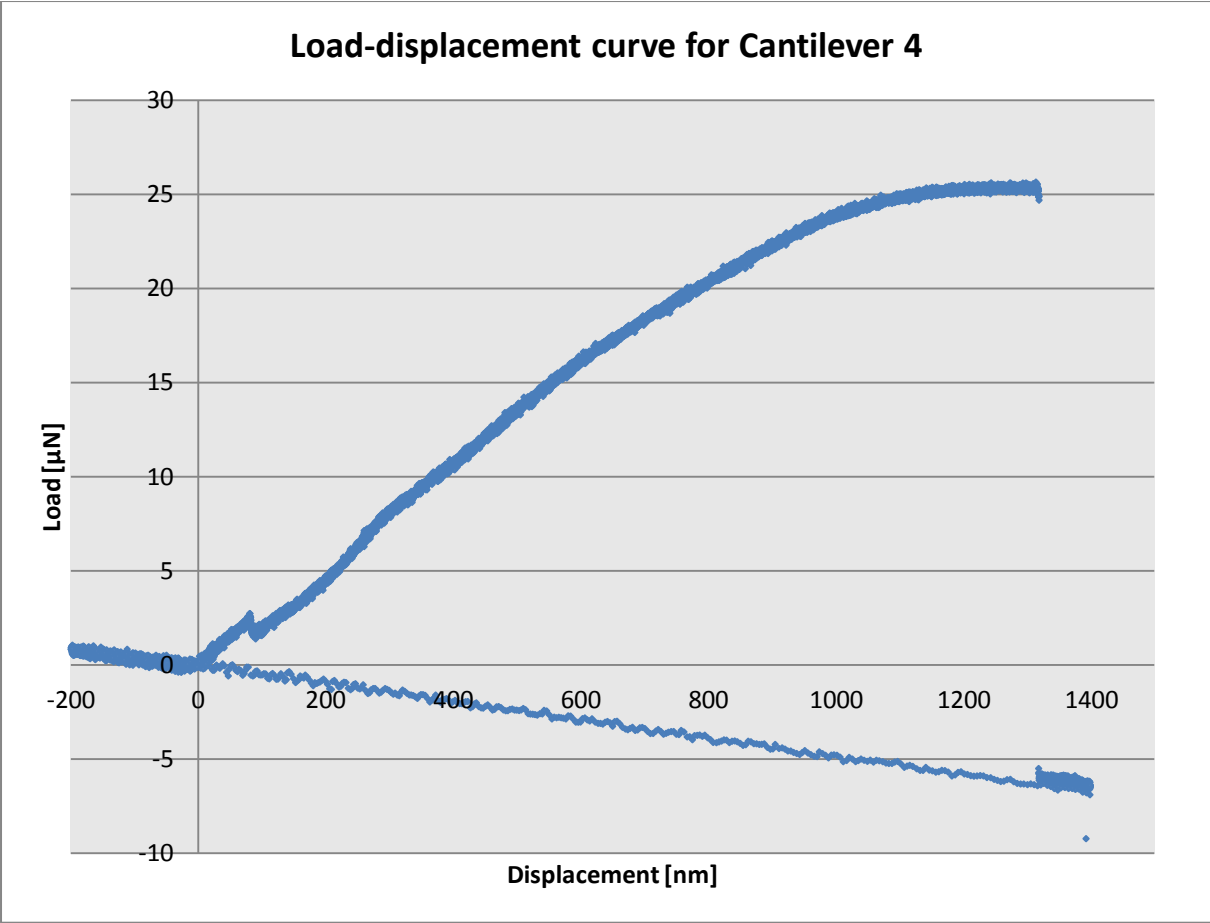
Figure 4.13: Load-displacement curve for Cantilever 4.
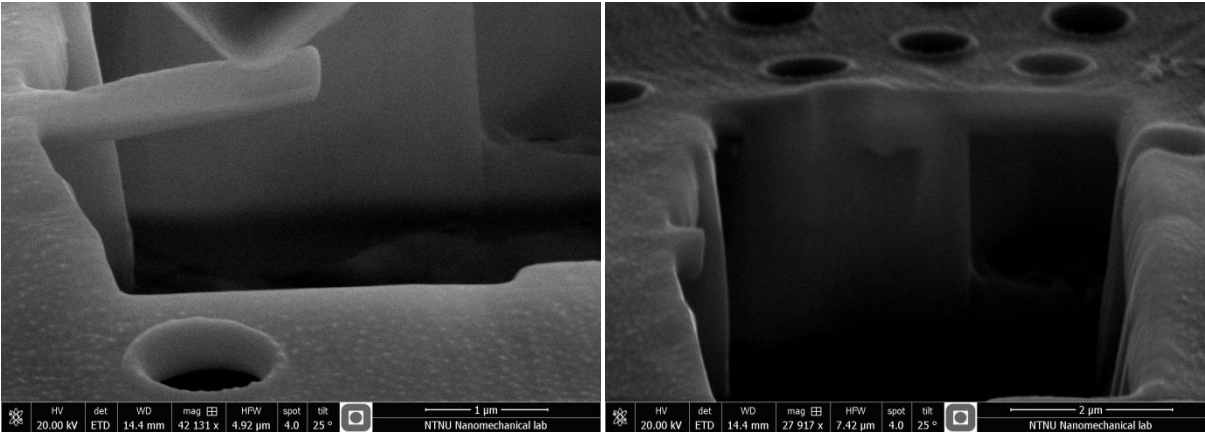
Figure 4.14: Cantilever 4 prior to loading and the remains of the beam post-fracture.

Based on the sloped unloading curve, it was decided to correct the values of the loading force. This was done by adjusting the values until the unloading line aligned with the horizontal axis. The result is displayed in Figure 4.15.
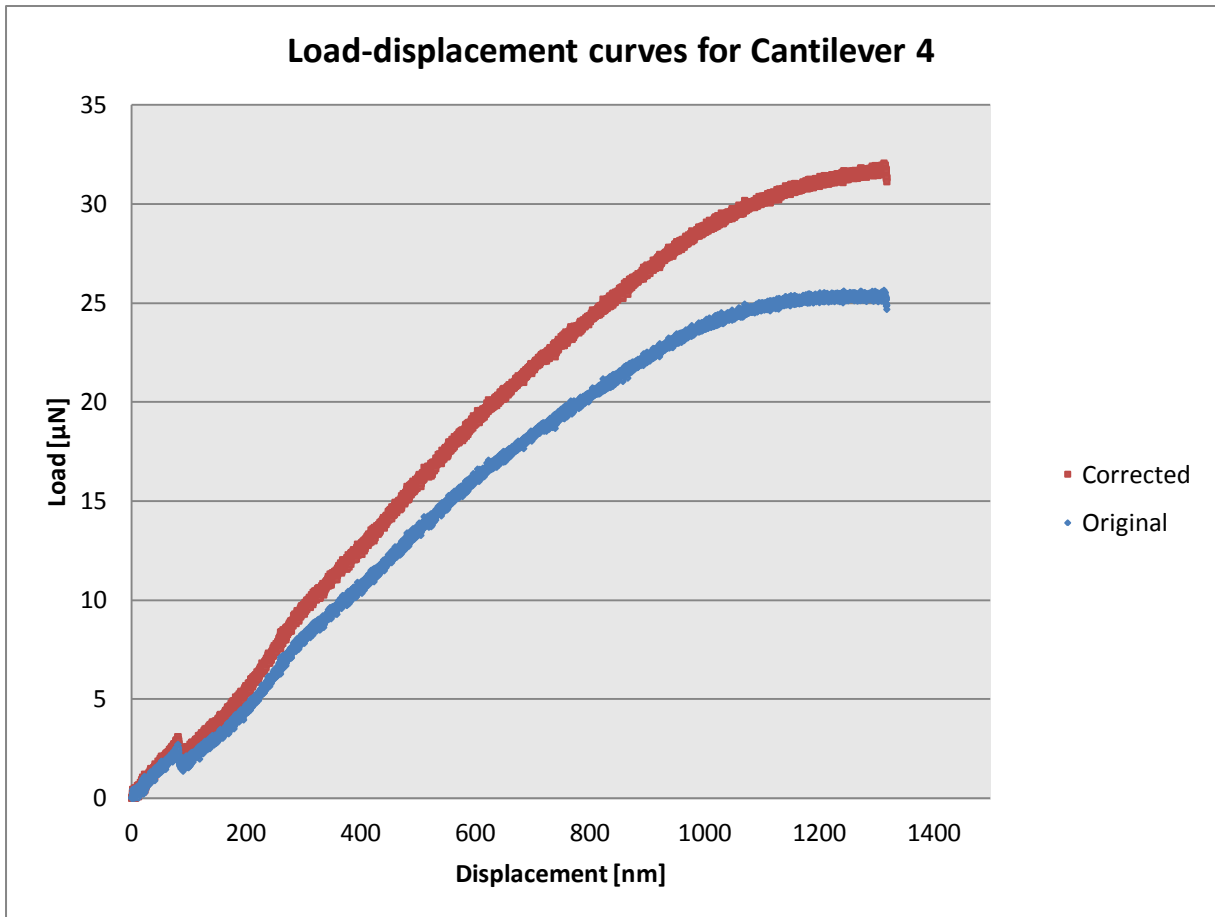
Figure 4.15: Original and load-correct load-displacement curves for Cantilever 4.

However, due to the upward sloping of the cantilever in the start position, the loading curve was also obtained from the point where the cantilever was completely horizontal. Prior to this load level, the notch may be dominated by compressive stresses due to the upward sloping, resulting in no stresses actively working to initiate crack growth. It was found that the cantilever was approximately horizontal when the indenter displacement had reached 790 nm. The load-displacement curve from this position is shown in Figure 4.16.
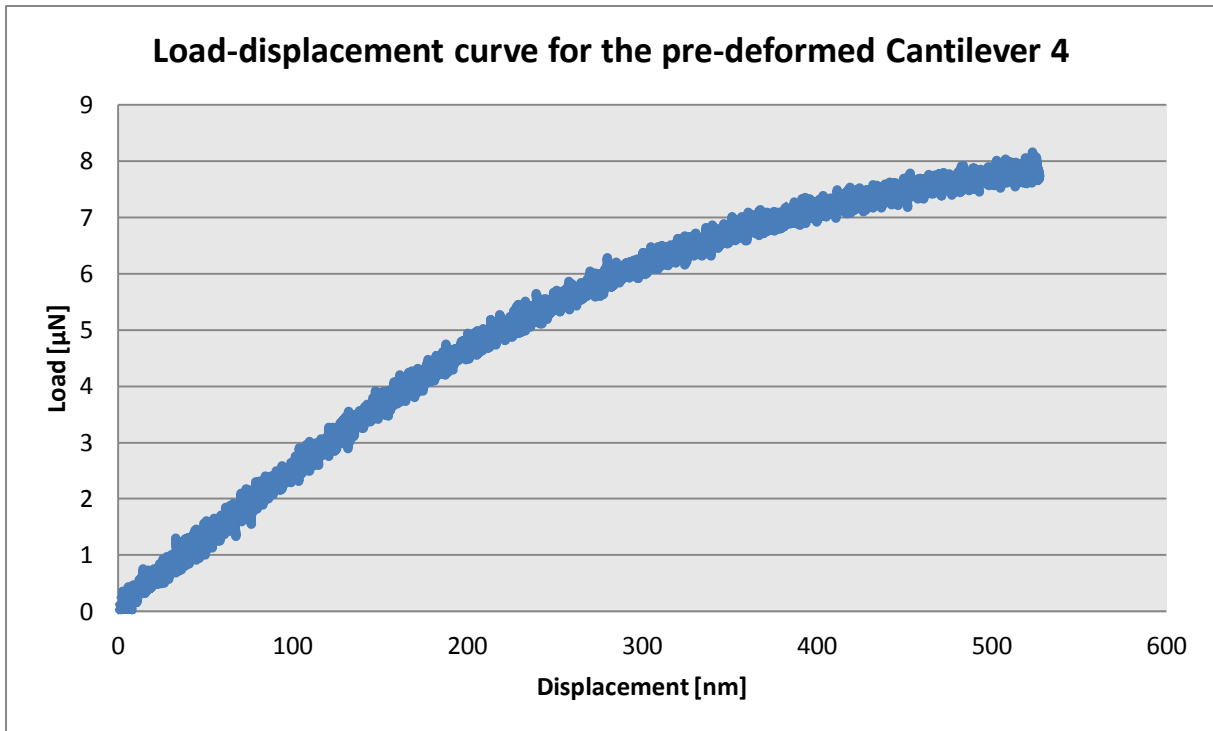
Figure 4.16: Load-displacement curve for the pre-deformed Cantilever 4.

From the recordings of the bending test, it was also observed that the indenter tip changed position during loading. In the initial stages, the indenter was placed at a location approximately 1500 nm from the notch, while this had been changed to 1400 nm at the horizontal level. A comparison between these two stages can be seen in Figure 4.17. The distance was measured to be constant during the rest of the bending test.
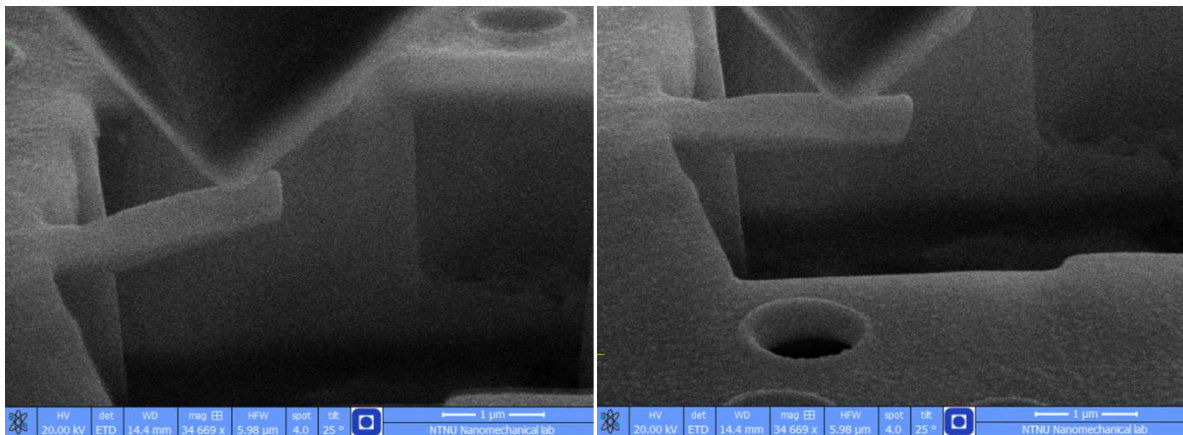
Figure 4.17: The cantilever at the initial loading position and at the horizontal alignment.

 Cantilever 5 and 6 were lost due to detachment and collision with the indenter tip respectively, as described in section 3.3.2.

Movies of the performed bending tests described in this section have been uploaded to DAIM with titles corresponding to the cantilever numbers and loading positions.[60]

4.4 Study of the fractured surface

From the study of Cantilever 4, the following images were obtained:

	HV	det	WD	mag ⊞	HFW	spot	tilt		3 μm
	10.00 kV	ETD	11.2 mm	22 480 x	9.22 μm	3.0	45 °		NTNU Nanomechanical lab
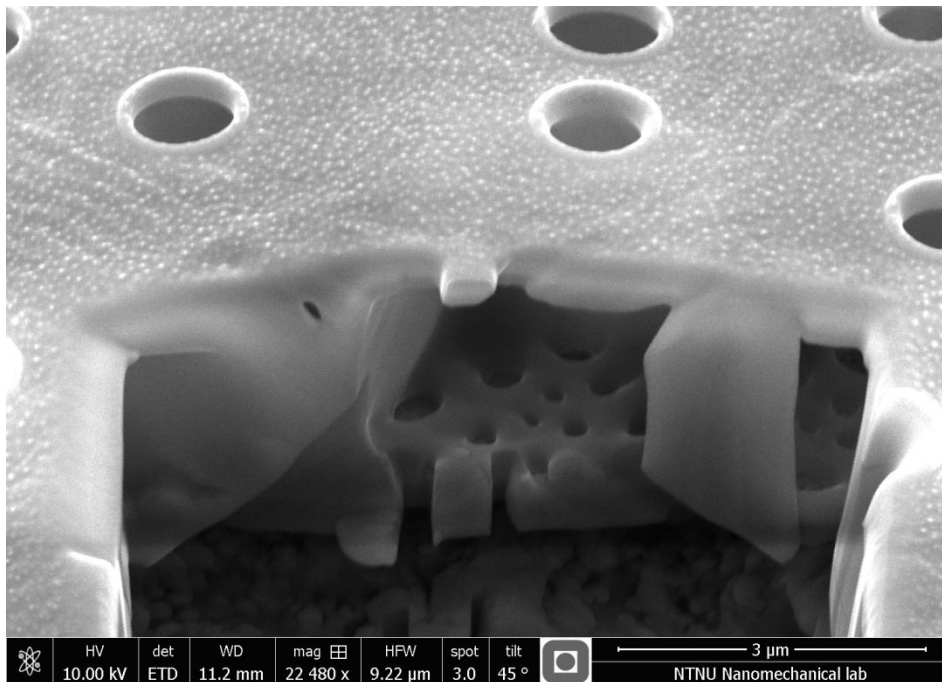
Figure 4.18: The remains of the cantilever and the surrounding area.

	HV	det	WD	mag ⊞	HFW	spot	tilt		500 nm
	10.00 kV	ETD	11.2 mm	119 165 x	1.74 μm	3.0	45 °		NTNU Nanomechanical lab
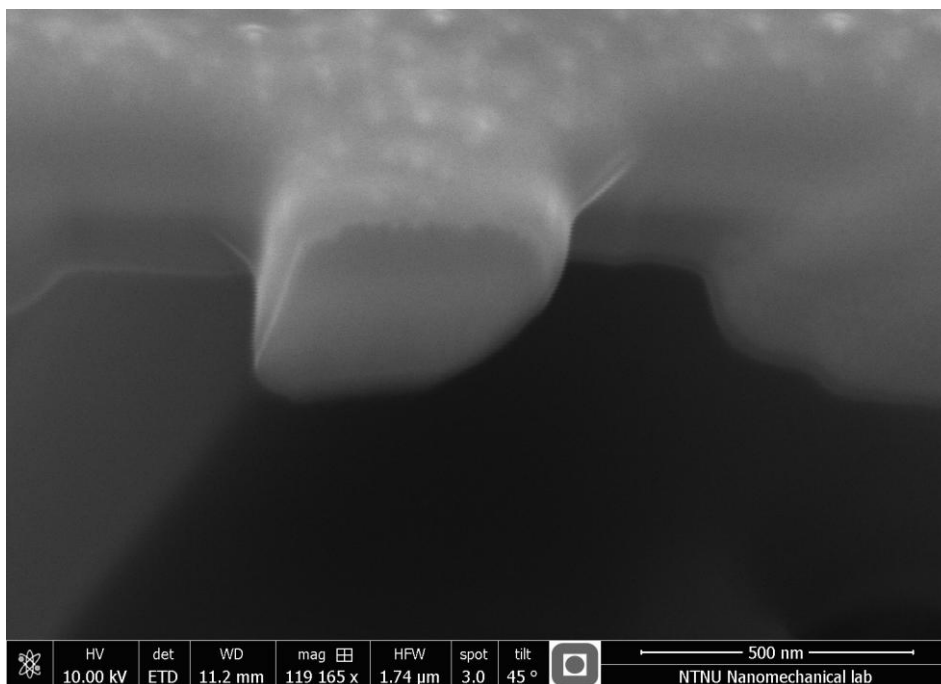
Figure 4.19: Detailed view of the fractured surface.

As seen, a section of the sides of the cantilever has been milled away when the notch was created. This was expected, but the amount of material milled away was surprisingly large.

A stable image was hard to achieve, as the material still exhibited charging effects. As such, it was not possible to get an image with greater detail of the fractured surface. Additional images with measurements are displayed in Appendix F.

During the AFM study, the frustule started to move during the scanning, yielding poor results. The frustule would usually attach itself to the AFM-tip when the tip was moved away from the frustule, as seen in Figure 4.20. Effort was made to stabilize the specimen, but with very limited success. Even when the initial scans after adjustments were successful, the frustule started to move again when the scanning area was changed. Examples of the obtained AFM scan results can be found in Appendix G.
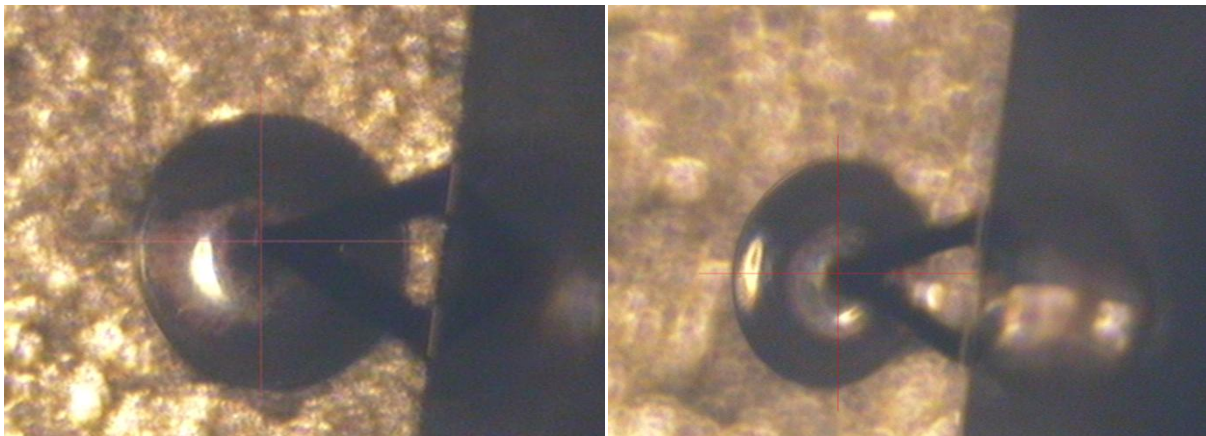
Figure 4.20: The frustule when being scanned by the AFM-tip.
To the left: Initial stable scanning.
To the right: The frustule had started to move and eventually attached itself to the AFM-tip.

4.5 Calculations of the fracture toughness

Based on the bending test and the study of the fractured surface, an approximation of the fracture toughness of the material could be performed. Since the surface deviated from the pentagon shape, it could be regarded as having a rectangular shape. By comparing the area of the original shape to that of a rectangle, it was found that the surface could be described as having a height of 416 nm and a width of 490 nm. The notch depth was set to 70 nm. The result is displayed in Figure 4.21.
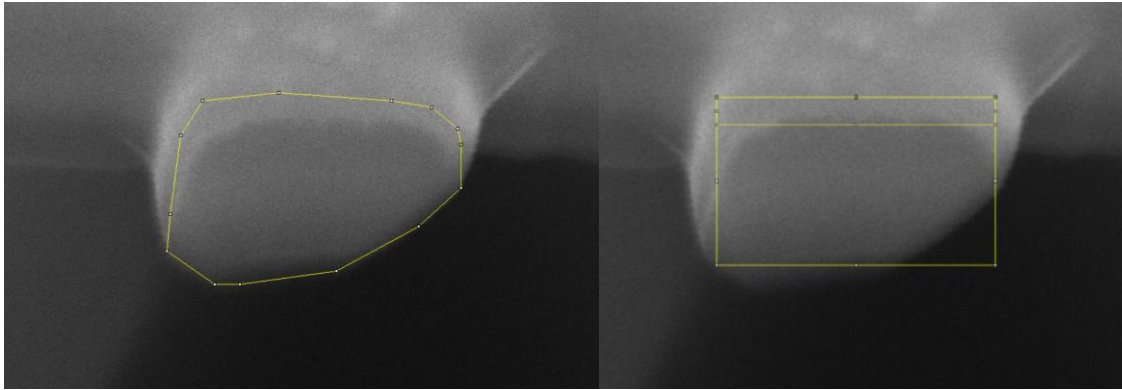
Figure 4.21:
To the left: The area considered to be the cross section at the fracture location, including the notch.
To the right: The rectangular approximation of the fractured surface. The upper rectangle represents the notched area while the outline represents the entire cross section.

Two possible load cases were considered; one were the notch experienced tensile stresses from the start and one were compressive stresses dominated the notch until the cantilever was horizontally aligned. In the case of the former, it was thought that the cantilever experienced crack growth when the load-displacement curve no longer was linear. A 5 % secant line was used to determine this transition area, with the result displayed in Figure 4.22.[48]
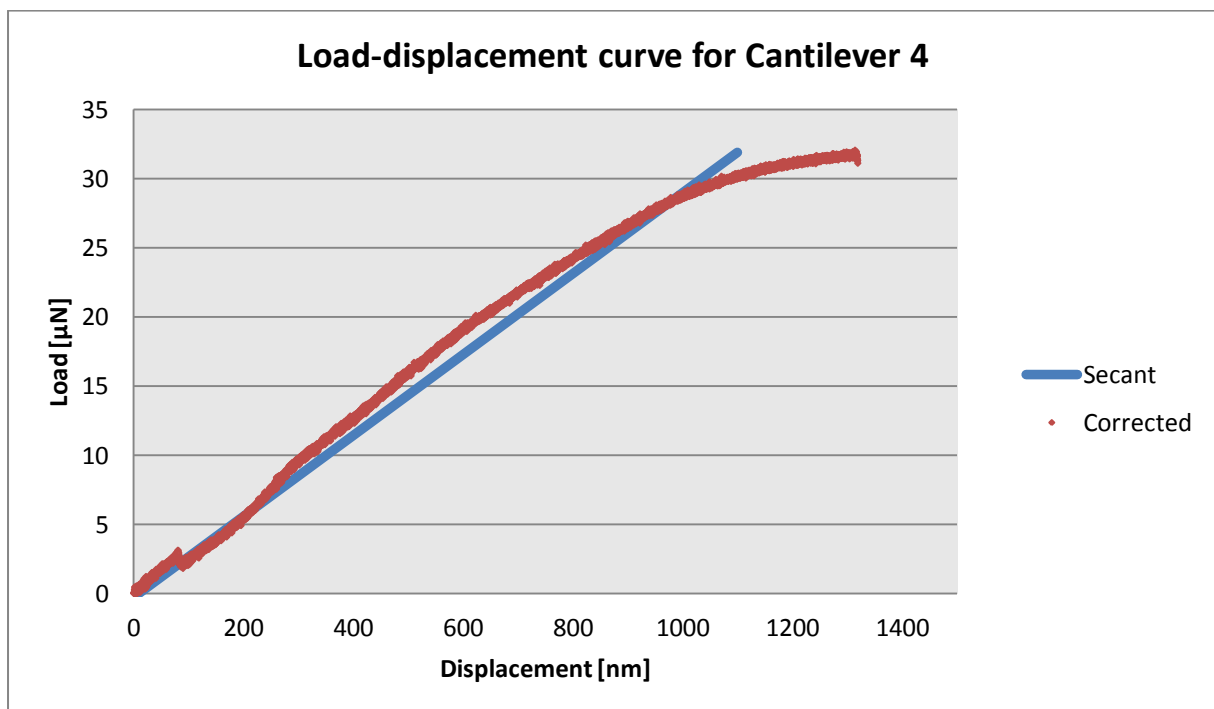
Figure 4.22: The corrected load-displacement curve and the 5 % secant line.

At the intersection point, the load and displacement was found to be 28,65 µN and 987,8 nm, respectively. For the horizontal cantilever case, the curvature of the graph was ignored and the load-displacement values were set to 7,73 µN and 527 nm. This was done in order to obtain a stress intensity factor at the exact point of fracture.

By using equations (2.12) and (2.11), a provisional fracture toughness, K_Q could be calculated. Once this was found, it would normally be controlled against a series of validation requirements in order to verify that the value is representative for the true fracture toughness of the material. However, due to having only one result with uncertainties test geometry, this would not provide an accurate value. Therefore, only K_Q was calculated.

Table 4.4 gives the relevant parameters and the results of the calculations.

Table 4.4: The calculated stress intensity factors.

Cantilever load case	a/h	f(a/h)	Loading length [nm]	Load [µN]	K_Q [MPa√m]
Secant	0,1683	4,5805	1400	28,65	1,3974
Horizontal				7,73	0,3770

4.6 Finite element analyses

4.6.1 Full model

The results from the full model can be seen in Table 4.5, with Figure 4.23 depicting the deformed model.

Table 4.5: The results from the full model analyses.

Mesh size at notch [nm]	Deflection [nm]	Young's modulus [MPa]	J-integral [N/mm]	K_{QJ} [MPa√m]
6	837,6	62192	0,05993	2,0452
3	838,4	62192	0,05910	2,0309
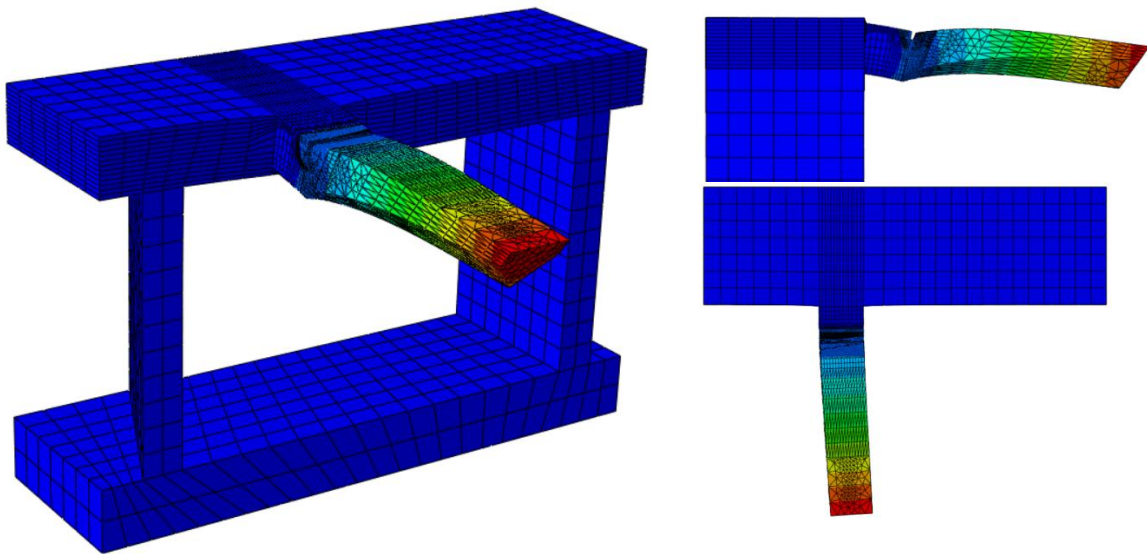
Figure 4.23:
To the left: The deformed full model. The colour is based on the vertical deflection.
To the right: Top picture displays the model as seen from the side, while the bottom picture displays the model as seen from above.

Since the deflection deviated by only 0,8 nm, the model was deemed to have reached convergence. The J-integral values were obtained by using the average value of the contours surrounding the stress field at the left side of the notch. This area, due to the cantilever's tilting to the right, had the highest stress values and is displayed in Figure 4.24. As such, the J-integral contours also reached a maximum value here.
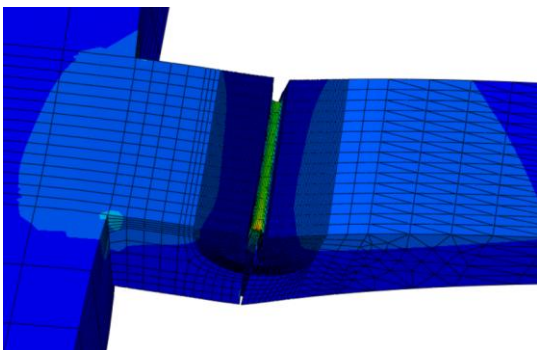
Figure 4.24: The maximum principal stress location.

73

4.6.2   **Pre-deformed model**

The results from the pre-deformed model can be seen in Table 4.6, with Figure 4.25 depicting the deformed model.

Table 4.6: the results from the pre-deformed analysis.

| Mesh size at notch [nm]	Deflection [nm]	Young's modulus [MPa]	J-integral [N/mm]	K_{QJ} [MPa√m]
3	526,9	27814	0,00303	0,3077
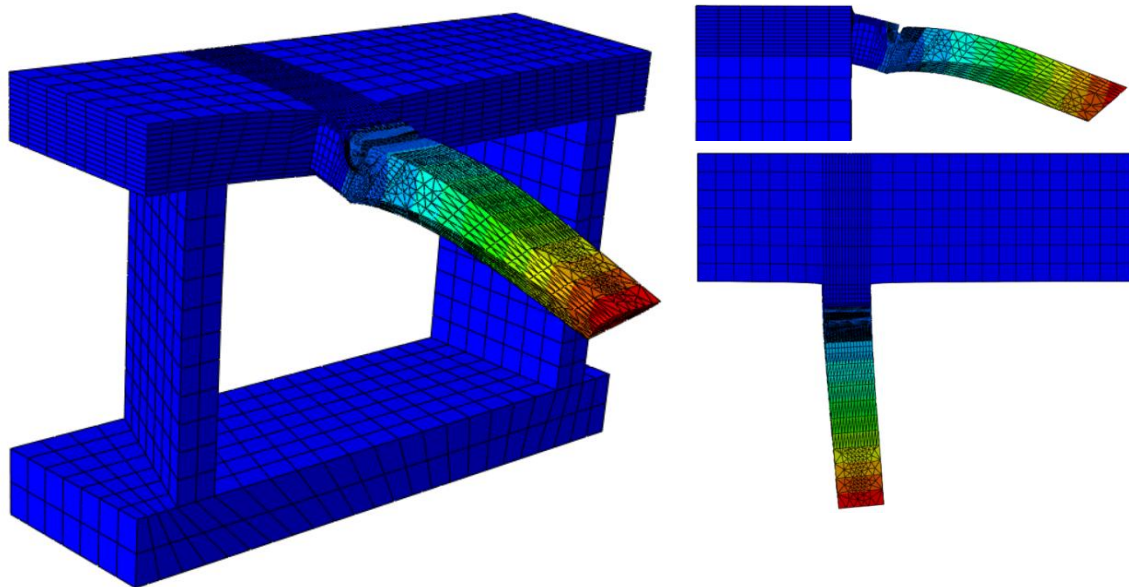
Figure 4.25:
To the left: The deformed pre-deformed model. The colour is based on the vertical deflection.
To the right: Top picture displays the model as seen from the side, while the bottom picture displays the model as seen from above.

As expected, the stresses also reached a maximum at the same location as observed in the full model, something that can be seen in Figure 4.26.
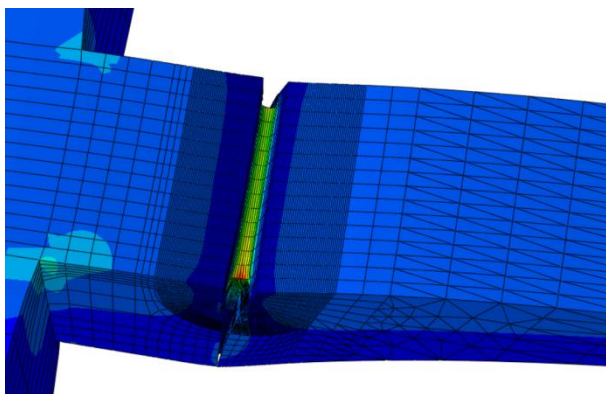
Figure 4.26: The maximum principal stress location.

74

5 Discussion

In this chapter, the results will be discussed and analysed. Important challenges and observations will be addressed and comparisons between previous testing and theory will be performed.

5.1 Geometry factor analysis

5.1.1 Convergence study, K_I and J-integral

As stated in section 3.1.2, the results obtained from the direct output request of the stress intensity factor and the J-integral differed greatly. The stress intensity factor varied with different sizes of the mesh, while the J-integral was found to be approximately independent of the mesh size. Larger elements than the ones used in the analyses would most likely have a greater impact on the J-integral as well. As seen in Figure 4.1, the stress intensity factor had a large spread in results for the coarse mesh, a good result for the finer mesh and four distinct results for the finest mesh. In the case of the coarse mesh, a poor result was expected, but the difference between the 2,6 nm element size and 1,6 nm element size was surprising. By looking at the contours generated by Abaqus, it was noted that the contour generating process for the finest mesh was not consistent, as depicted in Figure 5.1.
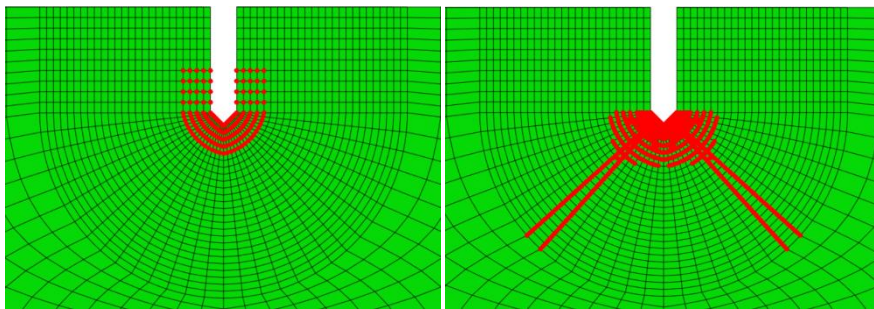
Figure 5.1: Two different series of contours generated by Abaqus, where one is normal (left) and the other is distorted (right).

A possible reason for the erratic behaviour for the test with the finest mesh is that the notch modelled was not represented as a thin line. This results in more elements not coming directly into contact with the crack front, which may cause issues for the mesh-sensitive stress intensity factor. The J-integral, being path independent, did not exhibit this behaviour. By comparing the upper curves of the stress intensity factor to the estimated J-integral, a good agreement was observed which resulted in the J-integral being used for the rest of the testing.

In the following convergence studies, it was found that the J-integral and deflection reached convergence immediately. For the deflection, this was expected, as the C3D20R elements will provide accurate results as long as there are two or more elements across the height of the cantilever. That the J-integral should converge in a similar fashion was unexpected, but this confirms why it is better than the stress intensity factor when using Abaqus. However, it is not without flaws, as it will produce different results at the very edges of the crack front, which must be discarded.

In both models, the stresses did not converge. This was expected, as the notch will form a stress singularity. The sharp notch resulted in the highest stresses, as the crack front is divided between two elements. The rounded notch, having multiple elements near the crack front, seemed to begin to

converge, but a very fine mesh would be required to verify this. Such an analysis would be extremely time consuming and would also not offer any important results.

5.1.2 Geometry factor

During the analyses, a notch element size of 4 nm was used, even though the convergence study showed that this was not needed. However, when extending the notch, the stress field could grow outside the mesh refinement area and yield poor results. By choosing a finer mesh, the elements in the surrounding areas would also decrease in size, which should partly secure the model against such effects. The results indicated that this was not necessary, as there were not any unusual deviations from the J-integral curves.

The result from the geometry factor analyses differs from the values given in literature by a large margin, as seen in Figure 5.2 and Table 5.1.[37, 39] The low geometry factor entails that the cantilever tested in this study will obtain a lower stress intensity factor when subjected to the same calculated stress values.
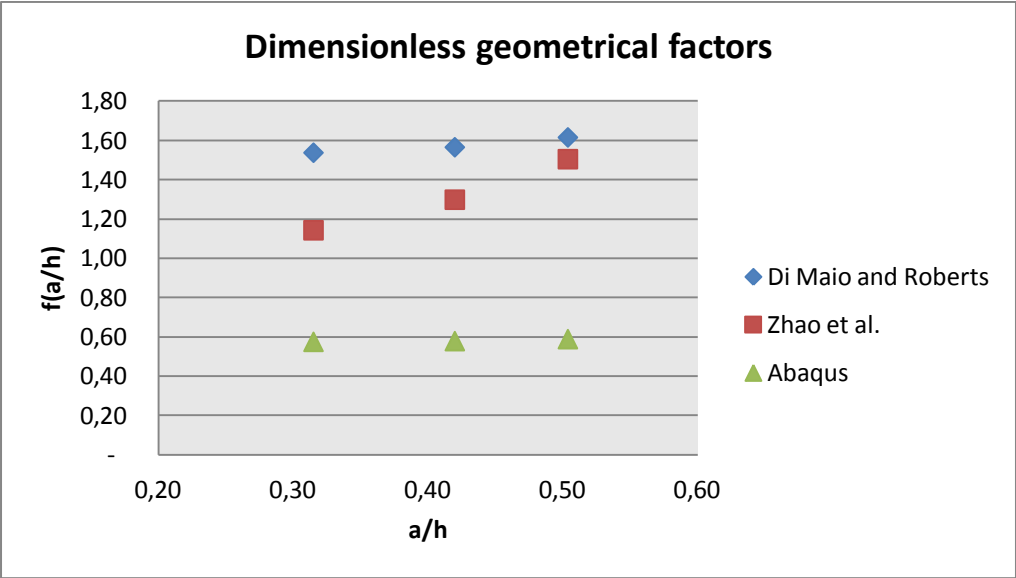
Figure 5.2: Comparison between the calculated geometry factor and those from other studies.

Table 5.1: Dimensionless geometry factors.

a/h	f(a/h) - Abaqus	f(a/h) – Di Maio and Roberts	f(a/h) – Zhao et al.
0,31	0,57	1,54	1,14
0,42	0,58	1,57	1,30
0,50	0,59	1,62	1,50

This may indicate that the model is inaccurate or improperly executed, but the convergence study indicates that this is not the case. A weakness with these results is that they are not based on experimental fracture tests with the same geometry, but were created with a material data from previous experiments. However, as the geometry factor modifies the relation between the applied force and the stress intensity factor, the results should be accurate if the material data is correct. These were collected from the analyses of the cantilever bending tests performed by Thaulow and shows almost idealised linear elastic behaviour, which means that only the Young's modulus should

76

be a limiting parameter when the material is not close to the point of fracture. The relatively small deflection ensures that this is not the case and should result in a high degree of accuracy.

A more reasonable explanation for the deviation is that the difference between the cross section shapes results in different stresses affecting the critical areas. A comparison can be made between two cantilever cross sections with identical widths but varying lengths of the rectangular sections, as depicted in Figure 5.3.
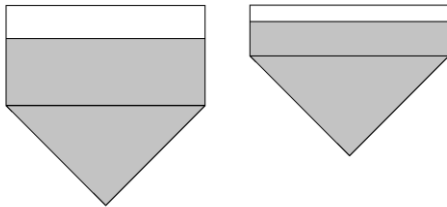
Figure 5.3: Two cantilever cross sections with the same width, but different lengths of the vertical sides.

The notch length is 30 % of the vertical side for both cross sections, but height of the vertical side is 50 % smaller on one of them. The reduced rectangular height results in a ratio of notch area to total area of 0,15 while the cross section with larger rectangular height has a ratio of 0,2. Thus, if the width is kept constant, an identical *a/h* ratio will have a greater negative impact on the cross section with the longest vertical sides. This fits well with the results from the analyses, since the geometry used in literature is more squarely shaped than the geometry used in this study. This also shows the difference between rectangular and pentagonal cross sections, as the study performed by Iqbal et al. on cantilevers with rectangular cross sections concluded that the dimensionless geometry factor was largely unaffected by a change in the *w/h* ratio.

Another possibility is that the valve's layered structure will deform during loading, which will reduce the strain on the cantilever. A solid supporting structure, which is used in literature, will have negligible yielding, thus increasing the cantilever stresses. The size of the surrounding structure may also have been modelled too small, resulting in an overly stiff reaction due to the boundary conditions, but this does not appear to be the case, as the model only has a small area of displacement around the cantilever.

5.2   Cantilever geometry and fabrication process

Due to material properties of the biosilica, there are a lot of uncertainties regarding the cantilever dimensions. The vertical sides of the cantilevers were almost indistinguishable from the top due to the small size, having a height in the range of only 100 to 150 nm. Therefore, a lot of faith had to be placed in the ability of the FIB to accurately produce the desired geometry. By incrementally patterning the structure, the process could be more accurately controlled, but other effects like charging of the material, beam shifting, noise generated by the ion beam and material bending would often result in less accurate geometry. User imprecision was also an issue. Due to the patterns being placed manually with no reference system to guide the placements, one minor misalignment could result in a large deviation from the desired result. This is also reflected in the resulting dimensions, especially regarding Cantilevers 4-6. These were produced with the intention of having as similar dimensions as possible, but difficulties with creating equally long vertical sides proved to

be challenging. As the milling process is time consuming and the amount of time available to use the FIB was limited, every cantilever fit for testing was accepted.

Another source of inaccuracy is the redeposition of material during milling. On nearly all cantilevers, the bottom is covered with redeposited material. While this should not have any effect on the notch and the development of the stress field around the crack initiation area, it might add extra strength to the cantilever as a whole, increasing the effective stiffness. Ion implementations may also affect the result, but as the cantilevers are relative small and the exposure time to the ion beam was kept at a minimum between the milling steps, it should not have a very large impact on the results.

The produced notch is also very uncertain. Apart from the depth, which was measured post-testing, the effective sputtering rate is dependent on the available free edges. Close to the free edges such as the sides, the material easily escapes, resulting in a deeper notch at these locations compared to the centre of the cantilever. This was also observed in the post-fracture study. An assumption that the ion beam produces rounded edges at the notch end was also made. This may not be accurate, but the experiences with all the other edges created with the FIB supports this assumption.

Lastly, the coating will be a part of the dimensional value of the height of the cantilever, but it should be negligible due to the layer only being 10 nm thick. Later, another layer of 10 nm thick coating was applied to reduce the charging effects. This may have affected the notch or the mechanical properties of the cantilever, as this additional coating may have covered the entire structure and not just a thin layer on the top of the beam. Another issue is that it may have filled the notch, resulting in extra forces needed to reopen it during testing.

5.3   Cantilever bending test

Out of the two cantilevers tested, only one yielded usable results, but the behaviour of Cantilever 3.2 is nonetheless interesting. The fact that contact was achieved between the indenter side surface and the cantilever during loading indicated that the cantilever was too slender, yet still having a large enough cross section to withstand considerable forces. When comparing the dimensions, Cantilever 3.2 had an aspect ratio of $L{:}w{:}h_{tot}{:}h = 3{:}0{,}93{:}0{,}93{:}0{,}40$ while Cantilever 4 had an aspect ratio of $L{:}w{:}h_{tot}{:}h = 3{:}1{:}0{,}89{:}0{,}29$. As seen, Cantilever 3.2 had a greater loading length, but also a larger cross section, so this should not be the cause of the behaviour. On the other hand, the fact that Cantilever 4 had an initial sloping may have prevented it from having the same issues. Unfortunately, due to only two bending test results, there is not enough data to confirm this theory.

Another source of this issue may be the redeposited material. As observed, this material make up a significant part of the cantilever volume and will affect the behaviour of the cantilever during testing. As this may come from both the aluminium stub and the rest of the frustule, it is hard to say how the mechanical properties will be altered. If the layer of redeposited material had been thinner, the effect would not be noticeable, but with a thick enough layer, it may stabilise the cantilever and prevent fracture at the correct loading level. The redeposited material is also the most likely cause of failure at the base of the cantilever instead of at the notch, as the non-uniform shape and nature of the material may cause local failures. The notch may also have been too small. Since this cantilever had been exposed to the FIB for a considerably longer time than the rest of the beams, there is also the possibility that the material have had its properties changed. This would at least partially explain

the apparent increase in stiffness, as ion implementation was shown to have this effect in the study performed by Orso.[26]

There are also uncertainties surround the testing of Cantilever 4. One of the main concerns is that the entire frustule may have been pushed downwards during testing, resulting in an invalid load-displacement curve. The recording of the SEM-generated images during loading shows that the structure is moving slightly upwards prior to the fracture, but this may be caused by the charging effects. The recording also shows that the entire structure is violently moving both when the indenter makes the initial contact and when the cantilever breaks. This is also caused by the charging effect, as proved by the shifting of the entire image and not one of the two components. Apart from the small "pop-in" at the very start of the testing, the curve is very smooth, which also indicates that the frustule did not move at the start.

The pop-in may be caused by several factors. The most likely explanation is that the additional layer of coating sealed the notch, resulting in a slight loss in stiffness when it was reopened. Another possibility is that this is the initial slipping of the indenter, but this should result in an increase in the load level as the indenter moved closer to the notch. Lastly, a local yielding at the tip of the indenter may also result in a pop-in, but this is not very likely considering the further movement of the tip.

Prior to the calculations and analyses, the load-displacement curve was adjusted by a linear factor based on the slope of the unloading line. The adjustment should be accurate, considering that the unloading curve behaves in a very consistent manner. The test performed on Cantilever 2 also suggests that the recording of forces will decrease over time, as the recorded points declined in value, even though contact had been made.

The load-displacement curve is mostly linear, indicating elastic behaviour, but prior to fracture, it starts to curve. This may indicate crack initiation or growth, the formation of plastic zones or both. Previous experiments, both by Hamm and at NTNU indicate that the material behaves in an elastic manner, so the formation of plastic zones is not very likely. The effect may also be caused by the picoindenter movement during testing. Said movement also means that approximately every point on the curve has a unique loading distance, which must be investigated if another values than the ones used in this thesis should be used.

The assumption that internal stresses dominate the cantilever before it had been straightened out may also not be entirely accurate. An increase in temperature during the fabrication process may have caused the deformation of the cantilever. The deformation was mainly observed during the milling of the sloped sides. By using equation (2.1) with material data for fused silica[61] and parameters for the Helios Nanolab FIB, the result shown in Table 5.2 was obtained.

Table 5.2: Calculated temperature increase of fused silica when exposed to the ion beam.

V [kV]	I [pA]	d [nm]	κ [W/m·K]	ΔT [K]
30	26	13	1,4	24,2

However, this is for bulk material. If the cantilever can be approximated as a pillar or a sheet structure, the effect is 4 times greater, resulting in a temperature increase of 96,8 K. Using the formula for thermal expansion, $\frac{\Delta V}{V} = \alpha \Delta T$, and the same material data for fused silica ($\alpha = 0,4 \cdot 10^{-6}$), the increase in volume will be 0,004 %. As such, the effects from the increased temperature are negligible, even when the beam current is ten times higher, as it was in the initial step. On the other

hand, the diatom biosilica may have different thermal properties than fused silica, meaning that the effect may be different from the calculated value.

Vebner also noted in his study that the cleaning process with centrifugation and chemical exposition had induced stresses into the frustules, which further reinforces the stress field theory.

When it comes to the charging effects, the most likely explanation is that the exposition to the ion beam had removed some of the protective layer during milling. As this only covered the foramen surface of the frustule, the sides of the crater created in the FIB would not be coated, leading to surfaces which would not be conductive. The same applies to the sides of the cantilever. Another possibility is that the coating was not applied properly, but such effects were not observed with the SEM mounted in the FIB. Image shifting was a problem with the FIB but whether or not this was caused by the material or the FIB system is not known, as similar effects had been reported by other users of the system with other material types, including iron and steel.

There are also some uncertainties surrounding the calculated values of the stress intensity factor. The loading distance was found to change during the bending tests, resulting in the need for post-test measurements. The study performed by Durst and Ahmad showed that the loading length has a great impact on the results, so extra efforts was made to have the measurements as accurate as possible. These would suffer because of the imperfect image quality during testing, as well as the perspective of the images, but they should be fairly accurate. The calculated values of the stress intensity factors would also be affected by this, as there is a linear relationship between the factors and the loading distance.

When comparing the calculated provisional fracture toughness values of 0,38 and 1,40 MPa√m to the ones from literature, they appear to match only partially. The highest value reaches 1,73 MPa√m, but this is from the testing of silicon nitride.[57] The most fitting materials, monolithic silicon and silicon oxide, have average toughness values of 1,1 and 0,68, respectively.[39, 57] The value of biosilica is thought to be in the same region. It is therefore logical to assume that the two analysed loading cases represent the extrema and that the real behaviour is somewhere in between.

The assumption that the fractured surface can be approximated as a rectangle will also affect the results, but the shape of the surface made such an assumption the most appropriate choice. The stress state calculated by the equations regarding a pentagonal shape would be less accurate, had those been used. The geometry factor employed was also reported by Matoy et al. to only be valid for an aspect ratio of $H: L: h: w = 2: 5: 2,1: 1,7$, which is different than the values of Cantilever 4. However, Durst and Ahmad concluded in their study that both the loading length and the ratio of width to height had no or negligible impact on the factor, which makes it valid for this case as well.

5.4 Study of the fractured surface

Due to the charging effects, there is little to be obtained from the SEM images of the fractured surface besides the dimensional values. The surface does seem smooth, which may indicate a brittle fracture, but without better images, no conclusions can be made. The AFM-study was also a failure, much due to the lack of adhesion between the frustule and the AFM-plate. In future studies, glue or carbon tape should be considered, even though the usage of these makes the sample preparation stage harder.

5.5   Finite element analyses

The model created is based on numerous approximations and is to some extent inaccurate. The assumed linear relationship between the fractured surface and the cantilever end may not be adequate to describe the cantilever properly, as the surfaces could have both been curved or irregular in nature. In addition, if the surrounding structure had yielded during testing, the vertical distances may also be inaccurate. The fact that the broken cantilever was not located also makes any modelling of the underside of the cantilever rather inaccurate by default.

In order to run the model in Abaqus, simplifications of the fracture surface had to be made. The most serious one is the straightening of the lines at the sides, as shown in Figure 3.22. To compensate for the loss in stiffness, the notch was lengthened so that the average value remained the same. While resulting in a correct Young's modulus, this may result in a lower stress intensity factor as the stresses will be distributed over a larger area. On the other hand, the increased distance from the neutral axis will increase the stresses at the area closest to the edge since the cantilever tilted sideways during loading. This may partly explain the curvature of the load-displacement graph from the bending test, as the sideways movement may have caused the displacement values to be slightly larger than they really should have been. The cantilever may also have become more affected by the load at this point, due to the neutral axis of the cantilever changing location, resulting in an additional moment being created.

The way the load was applied should be accurate. Since the indenter moved during loading, only the end value was used as the loading location. This should provide the right deflection value for the applied load, but the resulting load-displacement curve will not be the same as the one obtained in the experiments. Since the model was purely described by elastic material behaviour, the curve would nonetheless be linear, but by moving the load in the horizontal direction, a curved graph could be obtained.

The mesh also proved difficult to apply due to the advanced geometry. The structural mesh at the notch is adequate, but the surrounding areas suffered due to the transitions between the different shapes. As such, the mesh may not be optimal, as proven by the fact that tetrahedral elements had to be applied. However, the convergence study indicates that the mesh is good enough. The deflection had a minor change when refining the mesh, but this was only an increase of 0,10 %, which can be considered negligible. The difference in the J-integral is somewhat larger, having a decrease of 1,39 %. This may be caused by the extra displacement, but also by the refinement of the mesh. However, since these values are so small compared to the Young's modulus, the difference in the calculated fracture toughness is minor, decreasing only by 0,7 % between the two analyses. The model, as well as the pre-deformed model that was created from the finest mesh, should therefore be correct.

When comparing the fracture toughness values to that from literature, the same trend as observed with the purely calculated values can be seen, only by an even greater extent. The pre-deformed model yielded a value of 0,31 MPa√m while the full model achieved a value of 2,03 MPa√m. Not surprisingly, the pre-deformed value is closest to the corresponding calculated value, as the formula used becomes less accurate with large deformations. As such, the purely calculated value for the full model, is very inaccurate. The Young's moduli for the two models ended up at 27,8 and 62,2 GPa, with the former belonging to the pre-deformed model. From theory, the modulus should be in the

range of approximately 30 to 35 GPa. This indicates that the result should lie in the area between the two load cases, reinforcing the theory formed from the calculated fracture toughness values. If one assume that the relationship between the Young's modulus and the fracture strength is linear, the fracture toughness at a Young's modulus of 35 GPa ends up at 0,66 MPa√m. This is comparable to the values calculated from testing of silicon oxide.[57]

6   Conclusion

A way to test the fracture properties of the foramen has been developed and tested. By producing nanoscale cantilevers with the FIB and loading them to fracture with a picoindenter, a value of the fracture toughness could be calculated. It was found that the small dimensions created an extra challenge and that the nonconductive nature of the material resulted in issues during the testing. As such, it may be more productive to produce cantilevers with larger dimensions.

One cantilever was successfully loaded to fracture at the notched area using the picoindenter. Due to the complicated geometry and the unexpected fracture surface, the result was not conclusive. The fracture toughness was calculated both directly and by the use of finite element analyses and possible values were identified. However, in order to obtain a more conclusive result, additional tests needs to be performed.

In order to interpret the results, two load cases were analysed; one where the entire load-displacement curve was representative of the material behaviour and one where compressive internal stresses dominated the structure. The latter entailed that the crack-inducing stress field would begin later in the bending test. As the cantilever was sloped upwards at the initiation of the test, this was assumed to happen from the stage where it was horizontally aligned. These two models yielded considerably different results, as the Young's modulus was found to be 27,8 and 62,2 GPa, with the latter belonging to the full model. The provisional fracture toughness ended up at values of 0,31 MPaVm and 2,03 MPaVm. As the Young's modulus is supposed to be at in the range of approximately 30-35 GPa, the real fracture toughness should be somewhere between the calculated values.

A dimensionless geometry factor for the optimal cantilever geometry was also obtained. This was shown to be considerably lower than the values from theory, much due to the smaller vertical sides of the pentagonal cross section.

7 Further work

7.1 Adjustment of the cantilever dimensions

Based on the excessive deflection of Cantilever 3.2 and possibly Cantilever 4 if it had not been initially curved upwards, the aspect ratio of the cantilevers may need to be changed. During testing the ratio of width to length was set to 3, but it may need to be reduced to 2 in order to prevent the specimen from achieving contact with the side surfaces of the indenter tip. Cantilever with larger dimensions should also be considered. These would be less prone to inaccuracies in the dimensions and would also be less affected by material redeposition. The usage of coating will also be more effective, as the ratio of coated surface to uncoated surface will be greater due to the larger cantilever top area. This may prevent the charging effects experienced during testing.

However, the areola layer will remain on the underside of the cantilever during milling, which may worsen the effect of redeposition as there will be more hollowed areas to fill. The cantilever geometry would also need to be analysed post-fracture which may not always be possible, and finite element modelling and analysis must be applied instead of the traditional stress intensity factor equations.

7.2 Ion implementation from the FIB

The effect of ion implementation into the material should also be investigated. While usually not a problem since the FIB more often than not will just mill away the material instead of implementing ions into it, exposure to low beam currents over an extended period of time may result in the material properties being changed. In the fabrication process, exposure time to the ion beam was limited as much as possible, but it is conceivable that the material was affected during the milling process. By performing traditional indentations on unexposed frustules as well as frustules being subjected to the ion beam, the possible effect can be measured. The ion beam exposure can be varied both in duration and in intensity in order to simulate the different milling steps, and frustules with milled patterns could also be examined.

References

1. Round, F.E., R.M. Crawford, and D.G. Mann, *The diatoms: biology & morphology of the genera*. 1990, Cambridge: Cambridge University Press. 747 s. : ill.
2. Parkinson, J. and R. Gordon, *Beyond micromachining: the potential of diatoms.* Trends in Biotechnology, 1999. **17**(5): p. 190-196.
3. Liu, D., et al., *Metal-Organic Frameworks Reactivate Deceased Diatoms to be Efficient CO2 Absorbents.* Advanced Materials, 2014. **26**(8): p. 1229-1234.
4. Heggem, O.M., *NANOMECHANICAL TESTING OF DIATOMS*. 2014, Institutt for produktutvikling og materialer.
5. Cox, E., *Morphology, Cell Wall, Cytology, Ultrastructure and Morphogenetic Studies*, in *The Diatom World*, J. Seckbach and P. Kociolek, Editors. 2011, Springer Netherlands. p. 21-45.
6. Townley, H., *Diatom Frustules: Physical, Optical, and Biotechnological Applications*, in *The Diatom World*, J. Seckbach and P. Kociolek, Editors. 2011, Springer Netherlands. p. 273-289.
7. Losic, D., et al., *Atomic force microscopy (AFM) characterisation of the porous silica nanostructure of two centric diatoms.* Journal of Porous Materials, 2007. **14**(1): p. 61-69.
8. Gebeshuber, I.C. and R.M. Crawford, *Micromechanics in biogenic hydrated silica: Hinges and interlocking devices in diatoms.* Proceedings of the Institution of Mechanical Engineers, Part J: Journal of Engineering Tribology, 2006. **220**(8): p. 787-796.
9. Mann, D., *Size and Sex*, in *The Diatom World*, J. Seckbach and P. Kociolek, Editors. 2011, Springer Netherlands. p. 145-166.
10. Reimann, B.E.F., J.C. Lewin, and B.E. Volcani, *STUDIES ON THE BIOCHEMISTRY AND FINE STRUCTURE OF SILICA SHELL FORMATION IN DIATOMS : I. The Structure of the Cell Wall of Cylindrotheca fusiformis Reimann and Lewin.* The Journal of Cell Biology, 1965. **24**(1): p. 39-55.
11. Nakajima, T. and B.E. Volcani, *3,4-Dihydroxyproline: A New Amino Acid in Diatom Cell Walls.* Science, 1969. **164**(3886): p. 1400-1401.
12. Hecky, R.E., et al., *The amino acid and sugar composition of diatom cell-walls.* Marine Biology, 1973. **19**(4): p. 323-331.
13. Kröger, N., R. Deutzmann, and M. Sumper, *Polycationic Peptides from Diatom Biosilica That Direct Silica Nanosphere Formation.* Science, 1999. **286**(5442): p. 1129-1132.
14. Kröger, N., et al., *Species-specific polyamines from diatoms control silica morphology.* Proceedings of the National Academy of Sciences, 2000. **97**(26): p. 14133-14138.
15. Schmid, A.-M. and D. Schulz, *Wall morphogenesis in diatoms: Deposition of silica by cytoplasmic vesicles.* Protoplasma, 1979. **100**(3-4): p. 267-288.
16. Crawford, S.A., et al., *NANOSTRUCTURE OF THE DIATOM FRUSTULE AS REVEALED BY ATOMIC FORCE AND SCANNING ELECTRON MICROSCOPY.* Journal of Phycology, 2001. **37**(4): p. 543-554.
17. Brandon, D. and W.D. Kaplan, *Scanning Probe Microscopy and Related Techniques*, in *Microstructural Characterization of Materials*. 2008, John Wiley & Sons, Ltd. p. 391-421.
18. Haugstad, G., *Atomic Force Microscopy : Understanding Basic Modes and Advanced Applications*. 2012, Wiley: Hoboken.
19. *Schema MEB*. 2010, Wikipedia: http://commons.wikimedia.org/wiki/File:Schema_MEB_(en).svg.
20. *Electron gun*. 2014, Seal Labs: http://www.seallabs.com/cmss_files/imagelibrary/egun.jpg.
21. Khursheed, A., *Scanning Electron Microscope Optics and Spectrometers*. 2010, River Edge, NJ, USA: World Scientific Publishing Co.
22. Hjelen, J., *Scanning elektron-mikroskopi*. 1989: Metallurgisk institutt, NTH.
23. Goodhew, P.J., F.J. Humphreys, and R. Beanland, *Electron Microscopy and Analysis*. 2000, London, GBR: Taylor & Francis.

24. Stokes, D., *Principles and Practice of Variable Pressure : Environmental Scanning Electron Microscopy (VP-ESEM)*. 2009, Chichester, GBR: John Wiley & Sons.
25. Yao, N., ed., *Focused Ion Beam Systems*. 2007: Cambridge University Press.
26. Orso, S., *Structural and mechanical investigations of biological materials using a Focussed Ion Beam microscope*. 2005, Univ.: Stuttgart. p. 172.
27. Ishitani, T. and H. Kaga, *Calculation of Local Temperature Rise in Focused-Ion-Beam Sample Preparation.* Journal of Electron Microscopy, 1995. **44**(5): p. 331-336.
28. Oliver, W.C. and G.M. Pharr, *An improved technique for determining hardness and elastic modulus using load and displacement sensing indentation experiments.* Journal of Materials Research, 1992. **7**(06): p. 1564-1583.
29. Fischer-Cripps, A.C., *Nanoindentation*. 2011: Springer.
30. Ghisleni, R., et al., *In situ SEM indentation experiments: Instruments, methodology, and applications.* Microscopy Research and Technique, 2009. **72**(3): p. 242-249.
31. *PI 85 SEM PicoIndenter Information Sheet*. [cited 2. December 2014]; Available from: http://hysitron.com/products/pi-series/pi-85-sem-picoindenter.
32. Nowak, J.D., et al., *In-situ nanoindentation in the SEM.* Materials Today, 2010. **12, Supplement 1**(0): p. 44-45.
33. Hamm, C.E., et al., *Architecture and material properties of diatom shells provide effective mechanical protection.* Nature, 2003. **421**(6925): p. 841-843.
34. Bjørnøy, S.H., *NANOMECHANICAL TESTING OF DIATOMS*. 2012, Institutt for produktutvikling og materialer.
35. Vebner, M.J., *Nanomechanical Testing of Diatoms*. 2013, Institutt for produktutvikling og materialer.
36. Morland, M., *Diatoms in new design*. 2014, Institutt for produktutvikling og materialer.
37. Zhao, X., et al., *Mechanical properties of SiC coatings on spherical particles measured using the micro-beam method.* Scripta Materialia, 2008. **59**(1): p. 39-42.
38. Chan, Y.L., A.H.W. Ngan, and N.M. King, *Use of focused ion beam milling for investigating the mechanical properties of biological tissues: A study of human primary molars.* Journal of the Mechanical Behavior of Biomedical Materials, 2009. **2**(4): p. 375-383.
39. Di Maio, D. and S.G. Roberts, *Measuring fracture toughness of coatings using focused-ion-beam-machined microbeams.* Journal of Materials Research, 2005. **20**(02): p. 299-302.
40. Greina, K., *IN-SITU FRACTURE MECHANICAL TESTING OF MICROSIZED CANTILEVERS*. 2014, Institutt for produktutvikling og materialer.
41. Motz, C., T. Schöberl, and R. Pippan, *Mechanical properties of micro-sized copper bending beams machined by the focused ion beam technique.* Acta Materialia, 2005. **53**(15): p. 4269-4279.
42. Massl, S., et al., *Investigation of fracture properties of magnetron-sputtered TiN films by means of a FIB-based cantilever bending technique.* Acta Materialia, 2009. **57**(6): p. 1768-1776.
43. Darnbrough, J.E., D. Liu, and P.E.J. Flewitt, *Micro-scale testing of ductile and brittle cantilever beam specimens in situ with a dual beam workstation.* Measurement Science and Technology, 2013. **24**(5): p. 055010.
44. McCarthy, J., et al., *FIB micromachined submicron thickness cantilevers for the study of thin film properties.* Thin Solid Films, 2000. **358**(1–2): p. 146-151.
45. Wurster, S., C. Motz, and R. Pippan, *Characterization of the fracture toughness of micro-sized tungsten single crystal notched specimens.* Philosophical Magazine, 2012. **92**(14): p. 1803-1825.
46. Wurster, S., et al., *Micrometer-Sized Specimen Preparation Based on Ion Slicing Technique.* Advanced Engineering Materials, 2010. **12**(1-2): p. 61-64.
47. Griffith, A.A., *The Phenomena of Rupture and Flow in Solids*, in *Philosophical Transactions*. 1921. p. 163-198.

48. Anderson, T.L., *Fracture mechanics: fundamentals and applications*. 2005, Boca Raton, Fla.: Taylor & Francis. 621 s. : ill.

49. Irwin, G.R., *Fracture Dynamics*, in *Fracturing of Metals*. 1948, American Society for Metals: Cleveland, OH. p. 147-166.

50. Westergaard, H.M., *Bearing pressures and cracks*, in *Journal of Applied Mechanics*. 1939. p. 49-53.

51. Irwin, G.R., *Onset of Fast Crack Propagation in High Strength Steel and Aluminum Alloys*, in *Sagamore Research Conference Proceedings*. 1956. p. 289-305.

52. Irwin, G.R., *Analysis of Stresses and Strains near the End of a Crack Traversing a Plate*, in *Journal of Applied Mechanics*. 1957. p. 361-364.

53. Cherepanov, G.P., *Crack propagation in continuous media: PMM vol. 31, no. 3, 1967, pp. 476–488.* Journal of Applied Mathematics and Mechanics, 1967. **31**(3): p. 503-512.

54. Rice, J.R., *A Path Independent Integral and the Approximate Analysis of Strain Concentration by Notches and Cracks.* Journal of Applied Mechanics, 1968. **35**(2): p. 379-386.

55. Murakami, Y., *Stress intensity factors handbook. 1 (1987)*. 1987: Elsevier Science Limited.

56. Durst, K. and S. Ahmad. *Fracture simulations of micro-cantilever beams using Finite element modeling.* [Mini-project; Friedrich-Alexander-Universität Erlangen-Nürnberg] [cited 2015 6. May]; Available from: http://elite-map.tf.uni-erlangen.de/documents/Fracture%20simulations%20of%20micro-cantilever.pdf.

57. Matoy, K., et al., *A comparative micro-cantilever study of the mechanical behavior of silicon based passivation films.* Thin Solid Films, 2009. **518**(1): p. 247-256.

58. Iqbal, F., et al., *In situ micro-cantilever tests to study fracture properties of NiAl single crystals.* Acta Materialia, 2012. **60**(3): p. 1193-1200.

59. Rasband, W., *ImageJ*. 1997: National Institutes of Health.

60. *DAIM.* [cited 5. June 2015]; Available from: https://daim.idi.ntnu.no/.

61. *Silica - Silicon Dioxide (SiO2)*. [cited 25. November 2104]; Available from: http://www.azom.com/article.aspx?ArticleID=1114#_Fused_Silica.

Appendix

A. Additional results from the geometry factor analysis
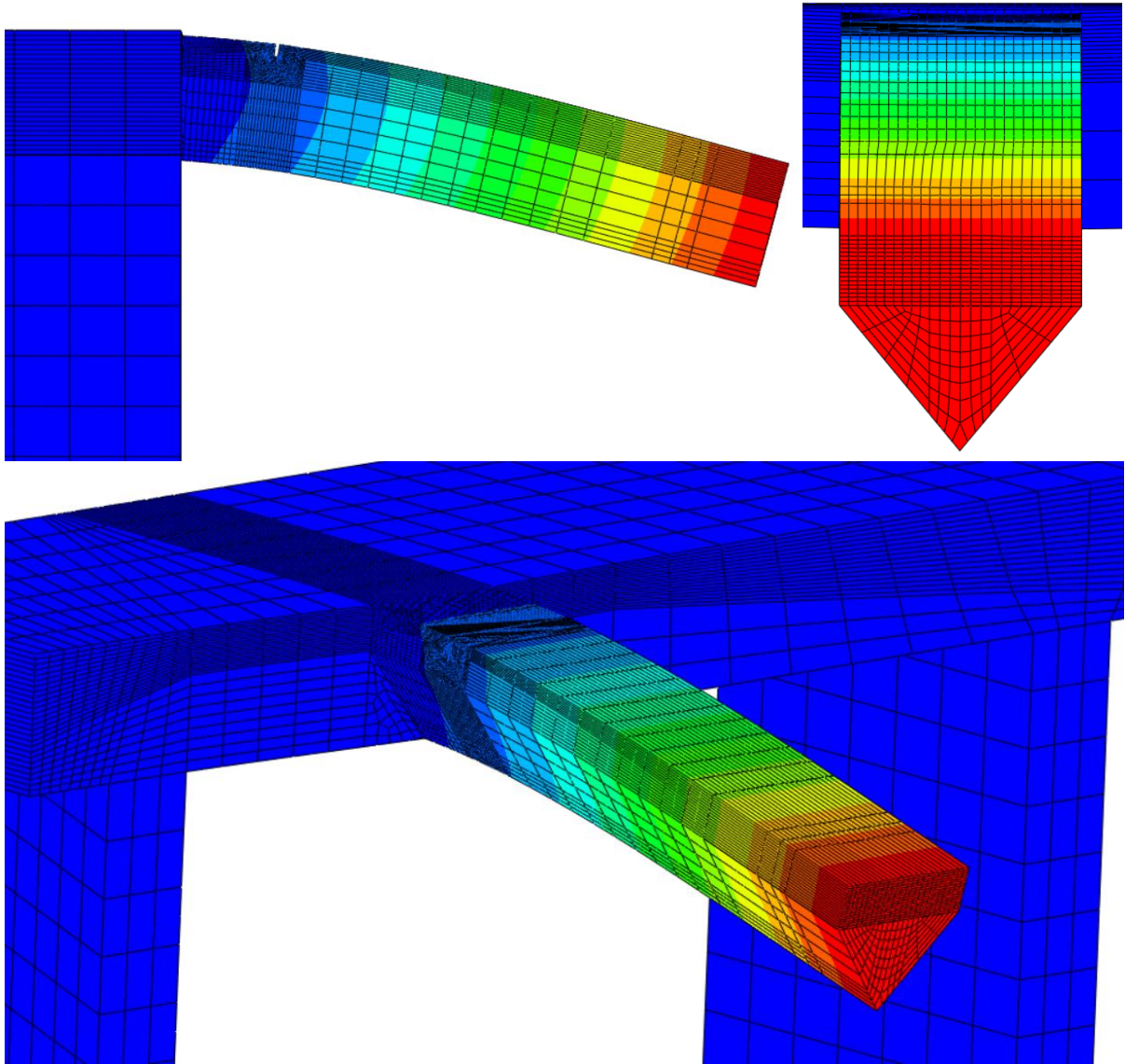
Figure A1: The deformed cantilever. As one can see, the deformations are concentrated around the actual cantilever and not the surrounding structure.
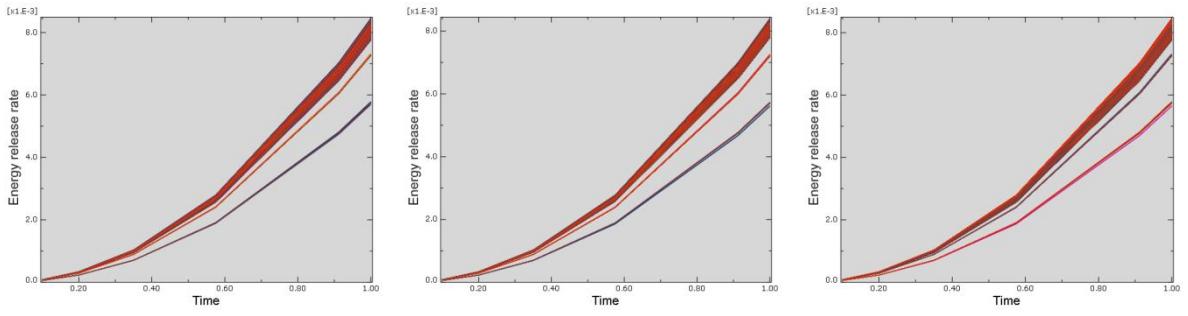
Figure A 2: The J-integral curves for the rounded notch. From left to right: mesh size of 6,6, 3,9 and 3 nm.
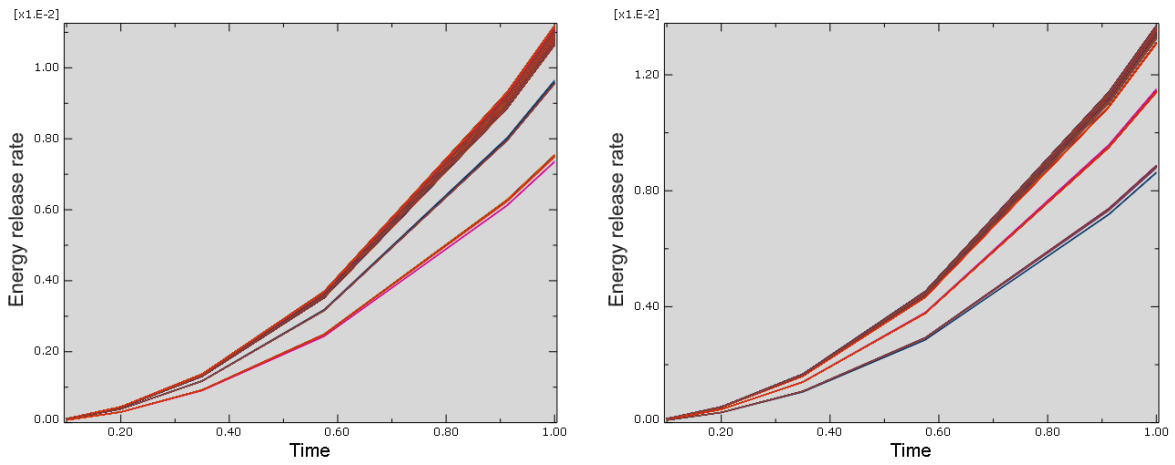
Figure A 3: The J-integral curve for a/h ratios of 0,42 (left) and 0,50 (right). The corresponding figure for the a/h ratio of 0,31 can be seen in the centre plot of Figure A 2.

B. Produced cantilevers that were scheduled for testing

Cantilever 1
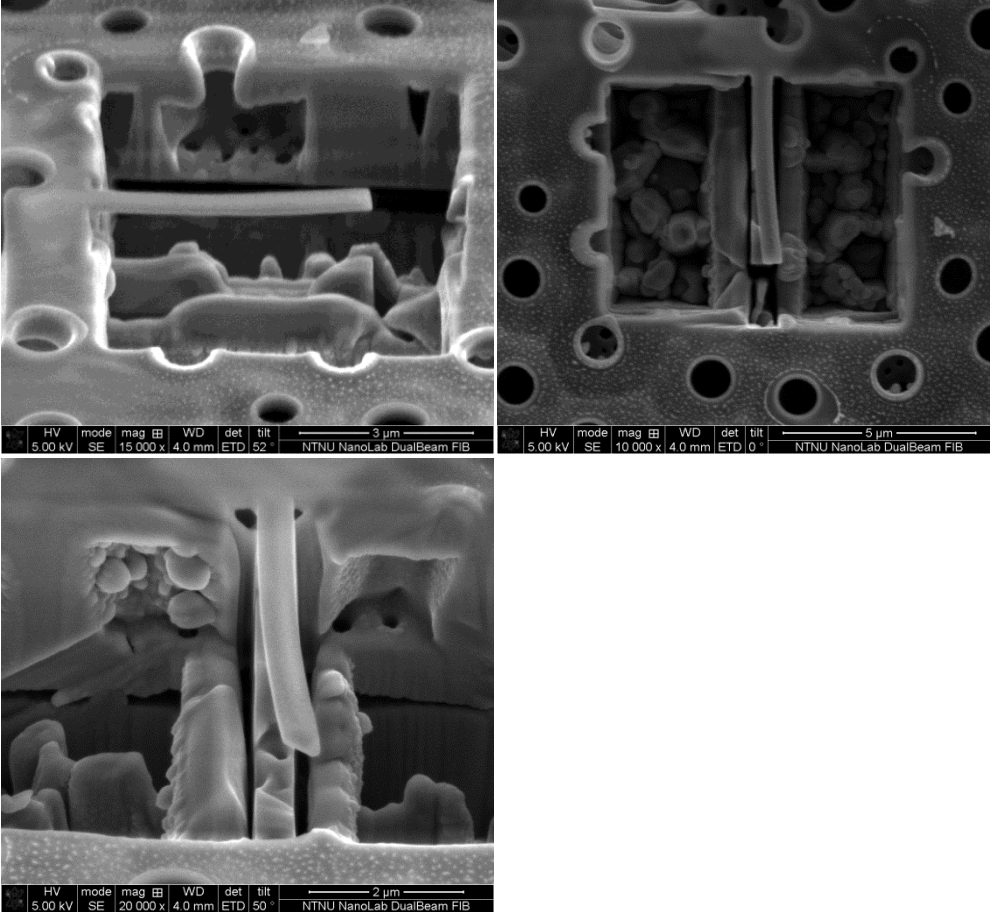
Figure A 4: Cantilever 1. During the fabrication process, the beam started to curve, resulting in bad geometry. The cantilever was therefore used as practice in the picoindenter.

Cantilever 2
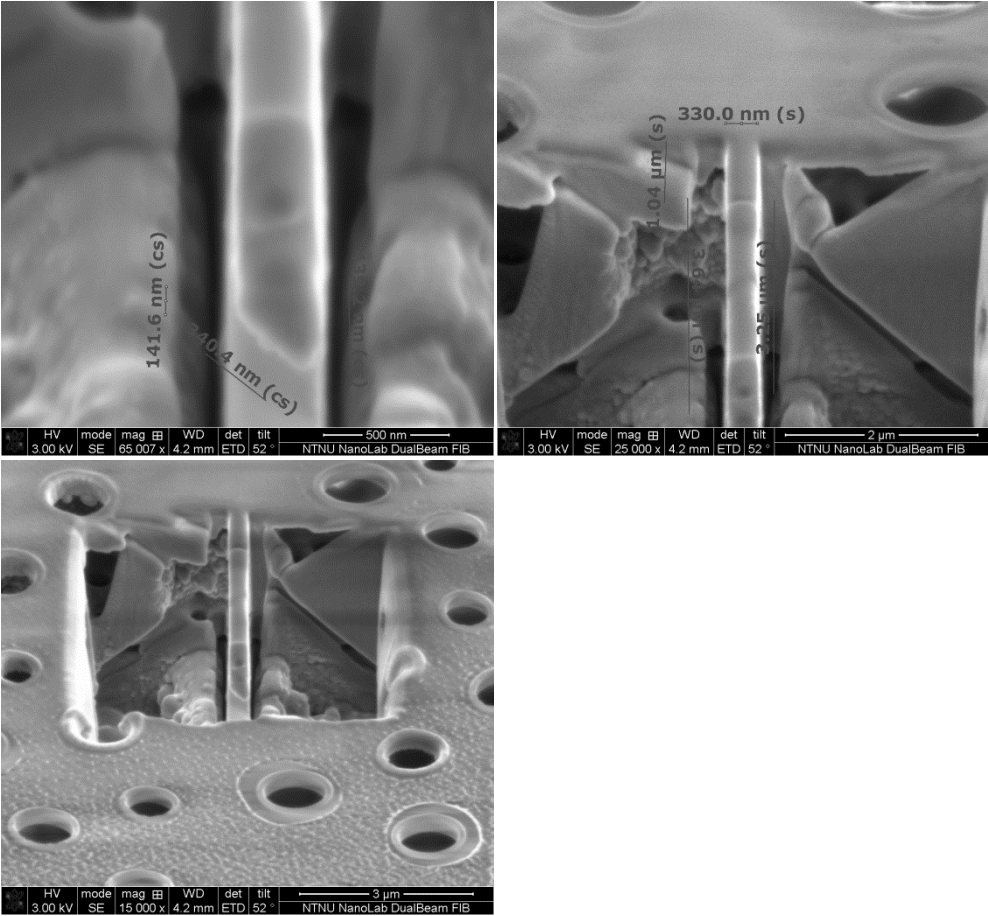
Figure A 5: Cantilever 2. Issues with the ion beam, both user- and instrument-induced, resulted in poor geometry. The cantilever was therefore used as practice in the picoindenter.

Cantilever 3.1
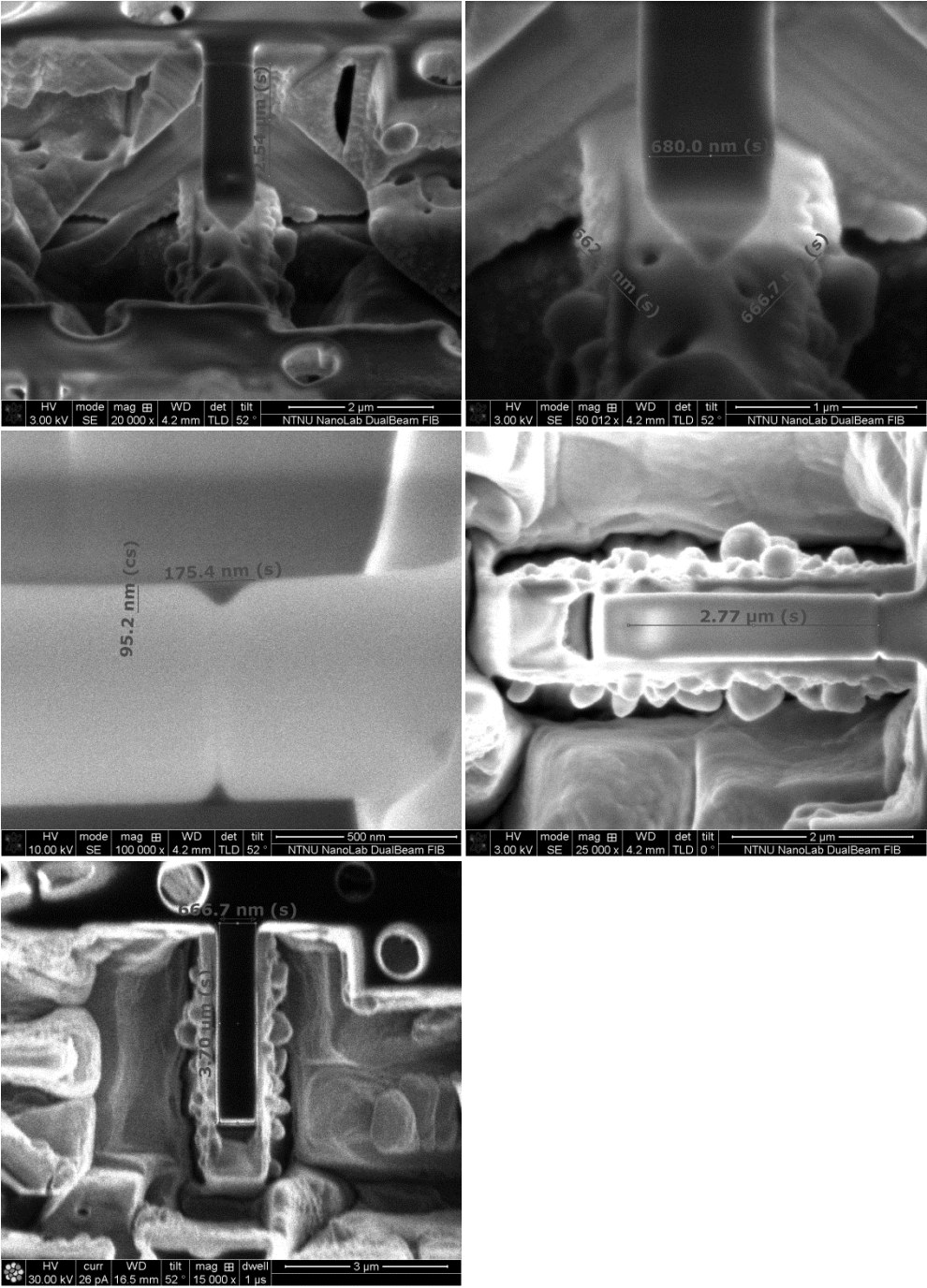
Figure A 6: Cantilever 3, pre-adjustments. During testing, the cantilever touched the bottom of the crater and had to be corrected before further tests could be performed.

Cantilever 3.2
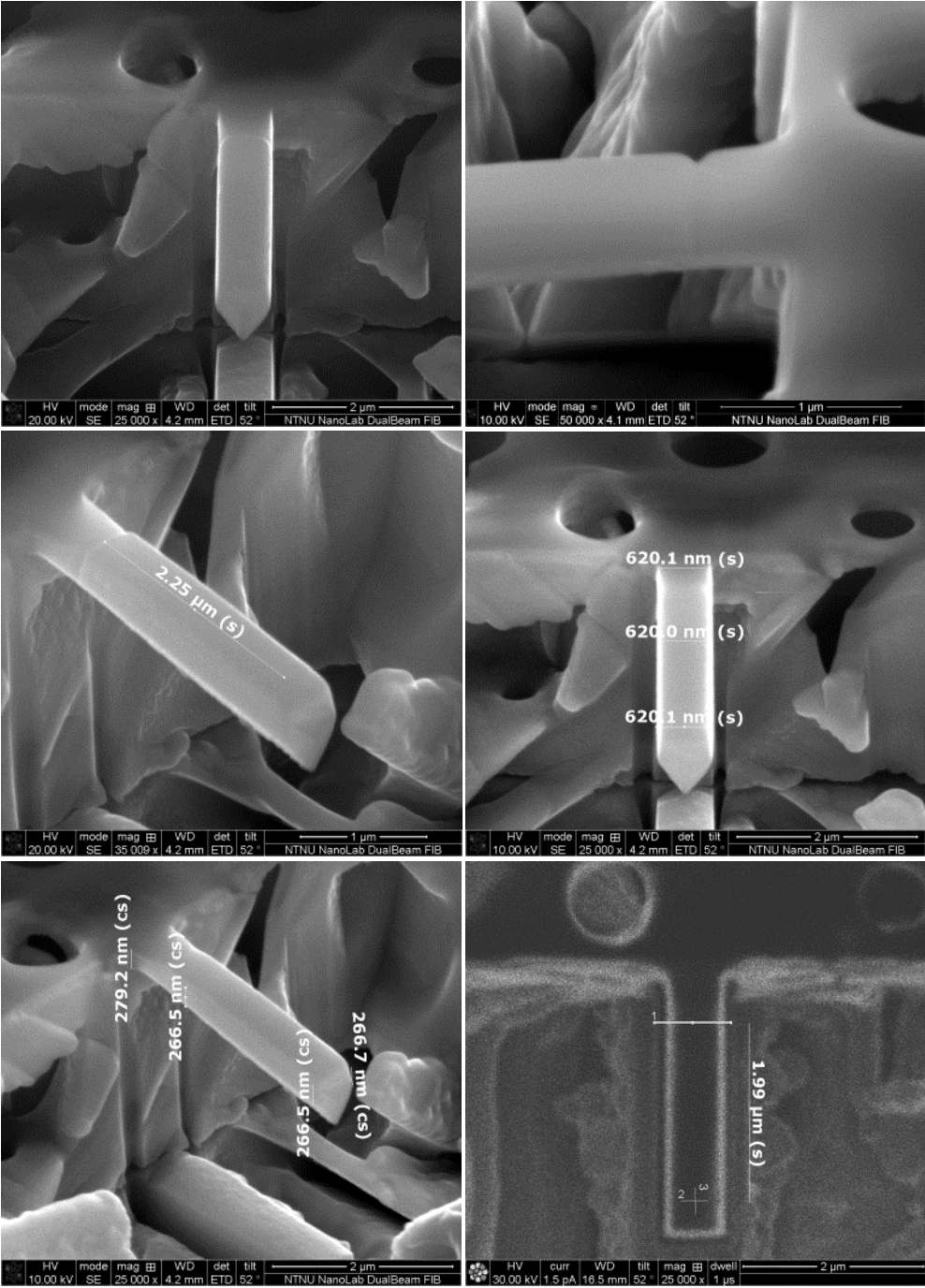
Figure A 7: Cantilever 3, post-adjustments. The crater was expanded, but redeposition on the cantilever resulted in the need of redefining the geometry with the ion beam.

Cantilever 4
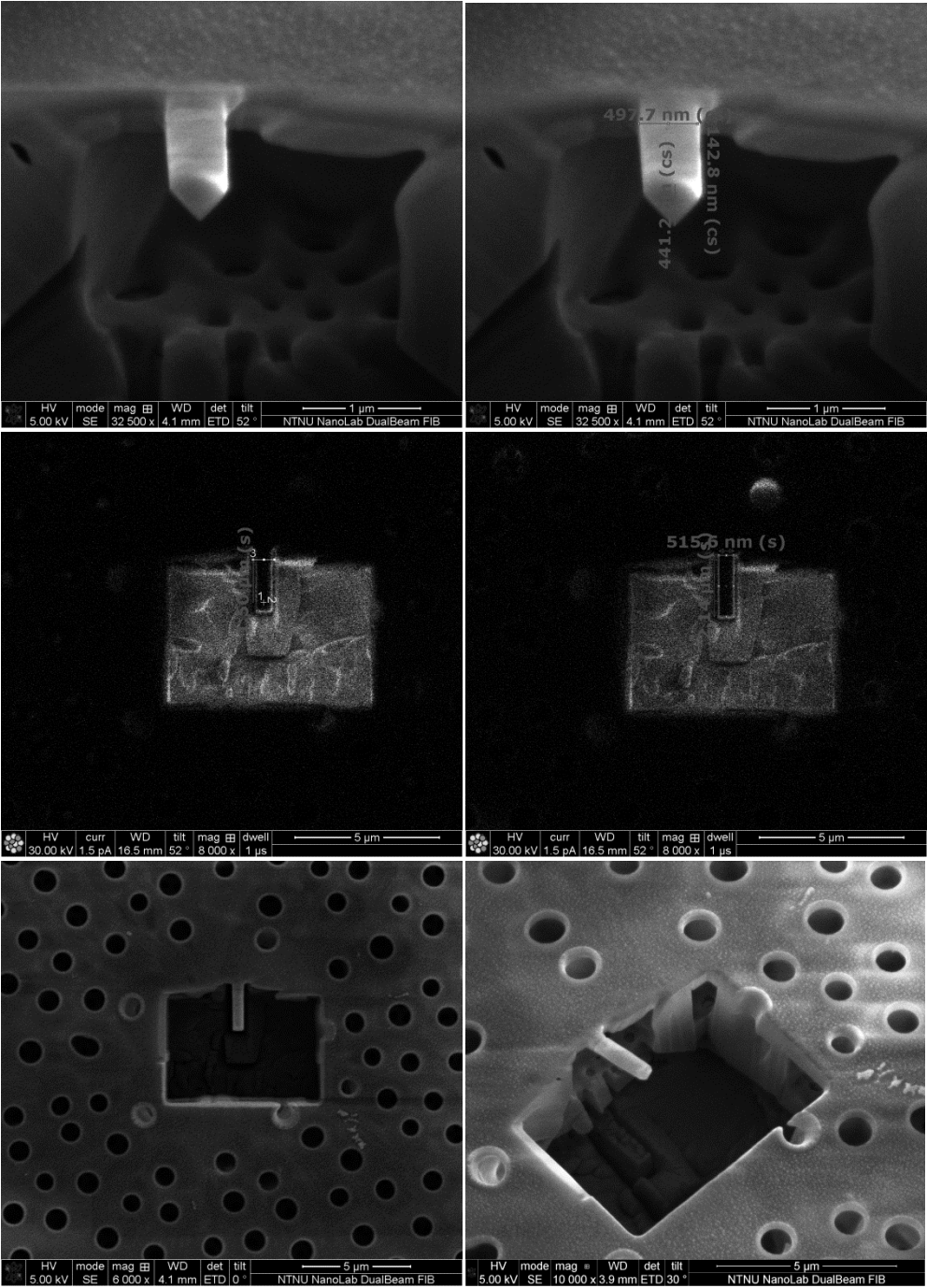
Figure A 8: Cantilever 4.

Cantilever 5
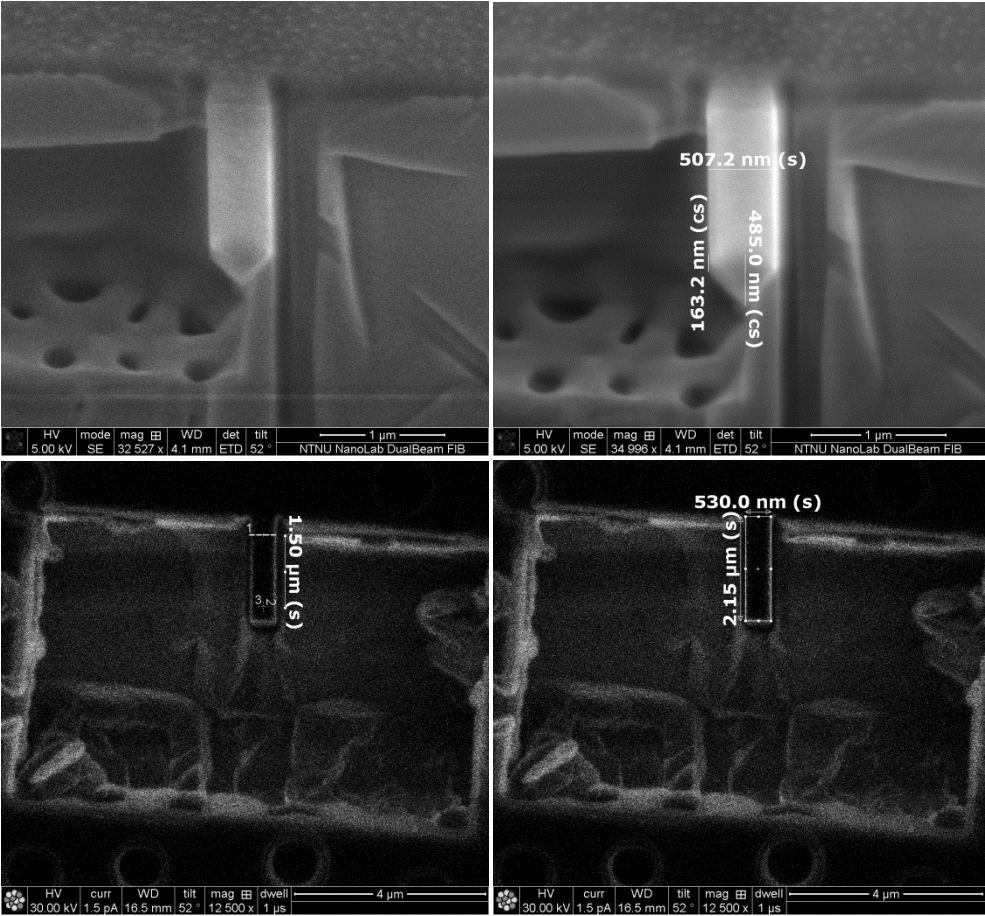
Figure A 9: Cantilever 5.

Cantilever 6
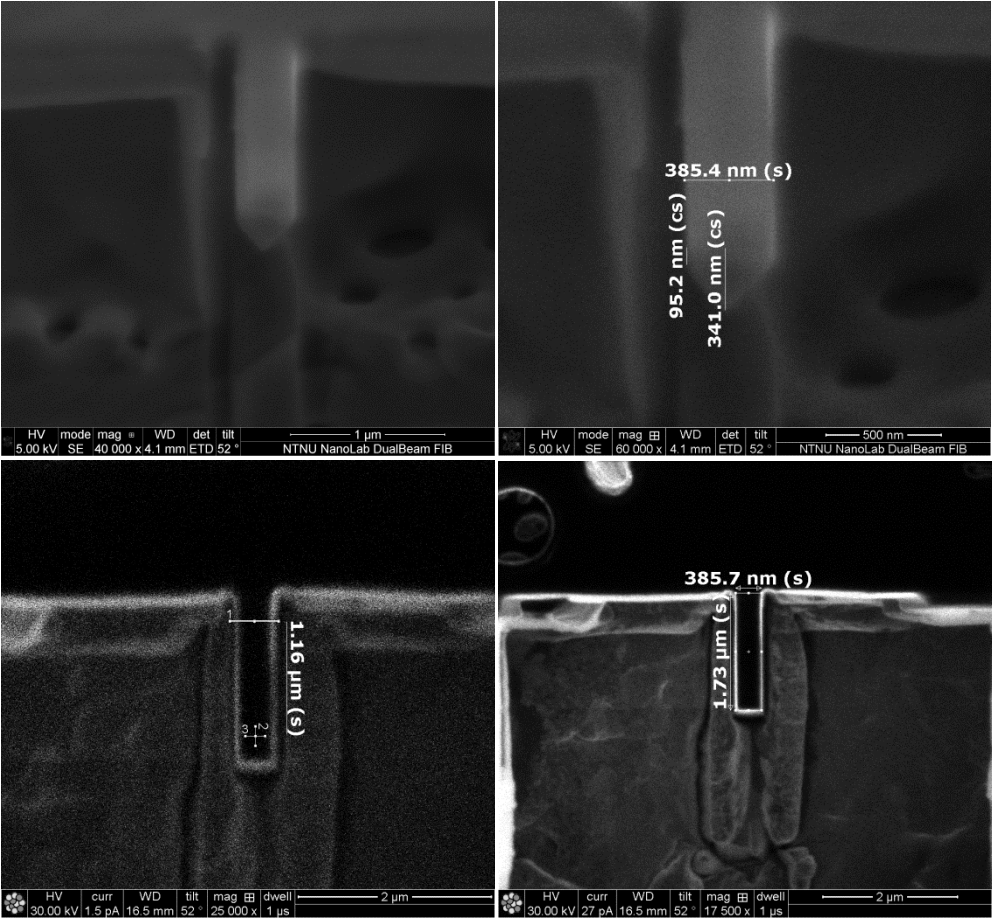
Figure A 10: Cantilever 6.

C.   Produced cantilevers that were not tested

Cantilever I
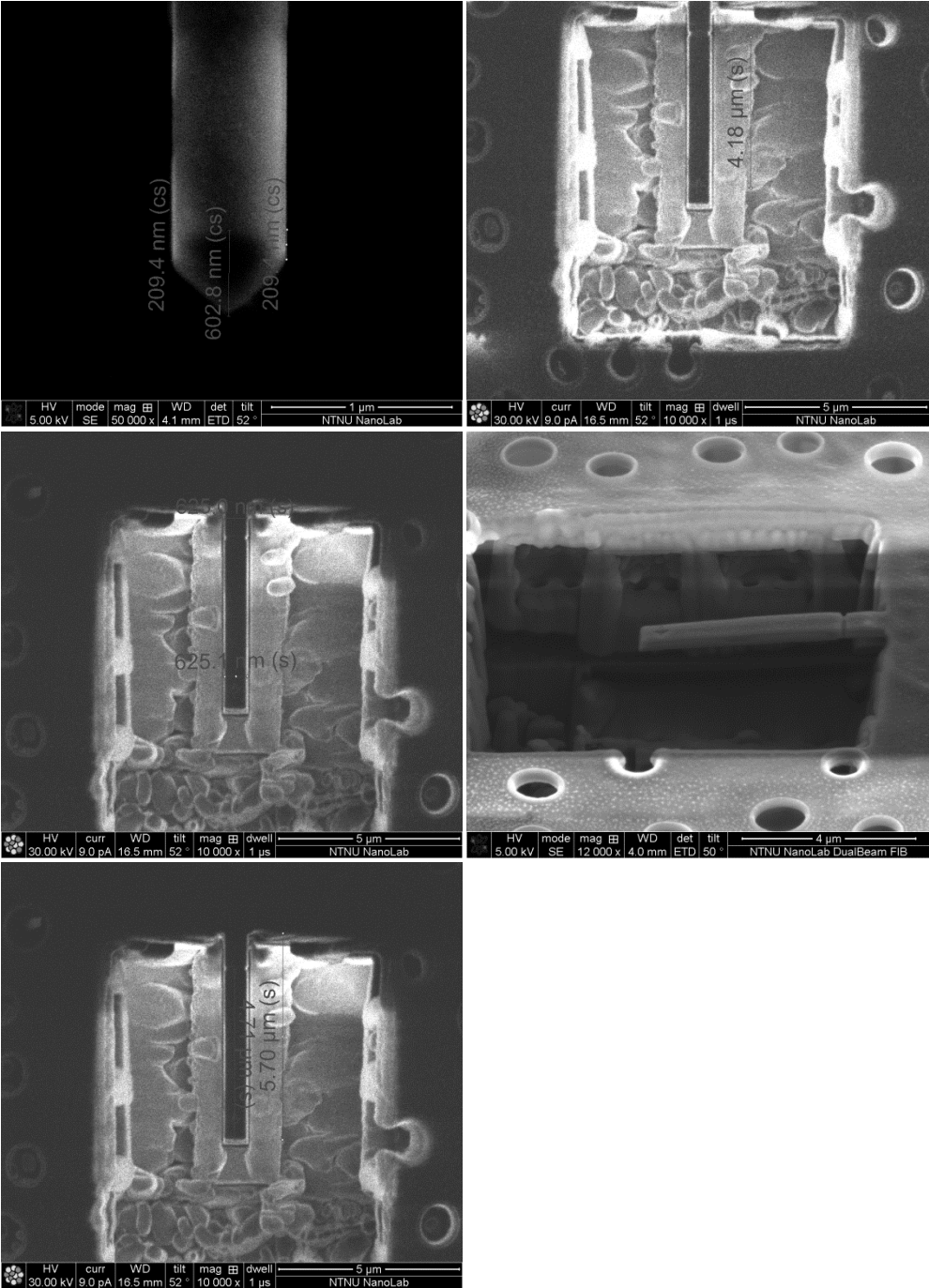
Figure A 11: Cantilever I. The cantilever was produced too far away from the centre of the stub, resulting in it being just out of reach of the picoindenter.
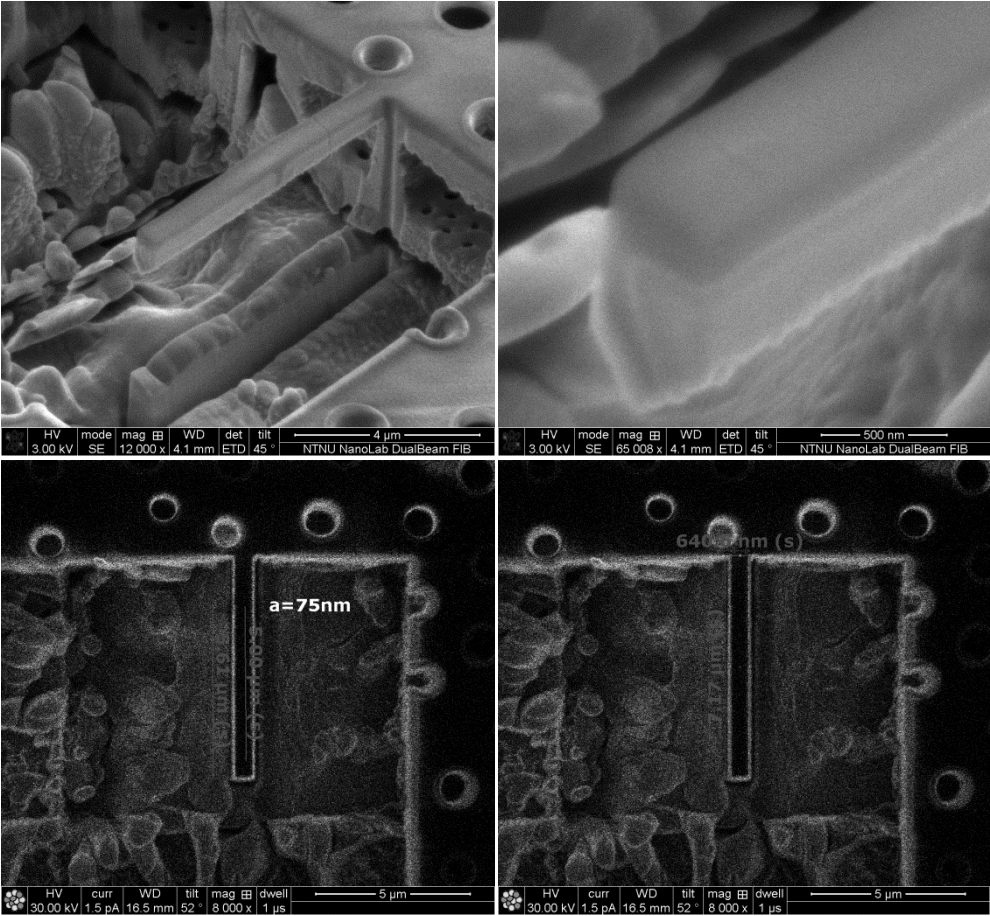
Cantilever II

Figure A 12: Cantilever II. Excessive redeposition made this cantilever unfit for testing. Adjustments could have been made, but the small size made such a procedure unlikely to succeed.

Cantilever III
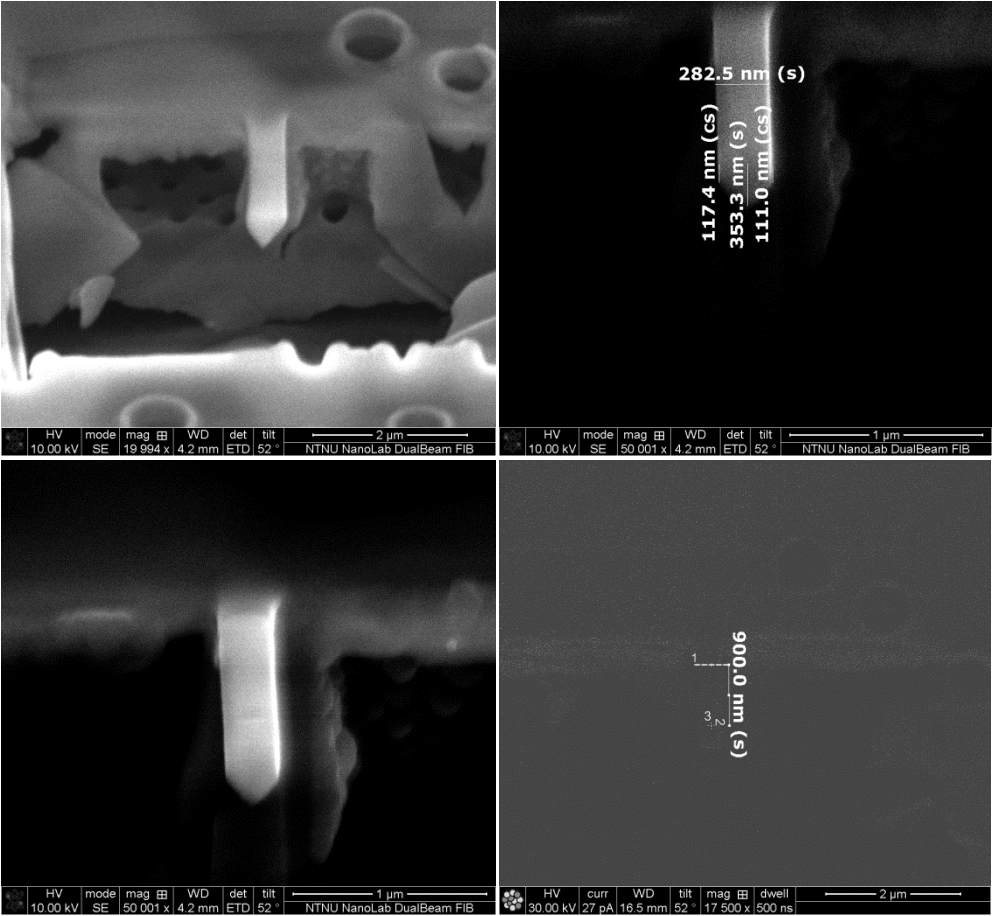
Figure A 13: Cantilever III. The last milling operation with the ion beam resulted in poor geometry. Adjustments were made, but the beam ended up being too small and would have been extremely difficult to hit with the indenter tip.

D.   Results from practice cantilevers
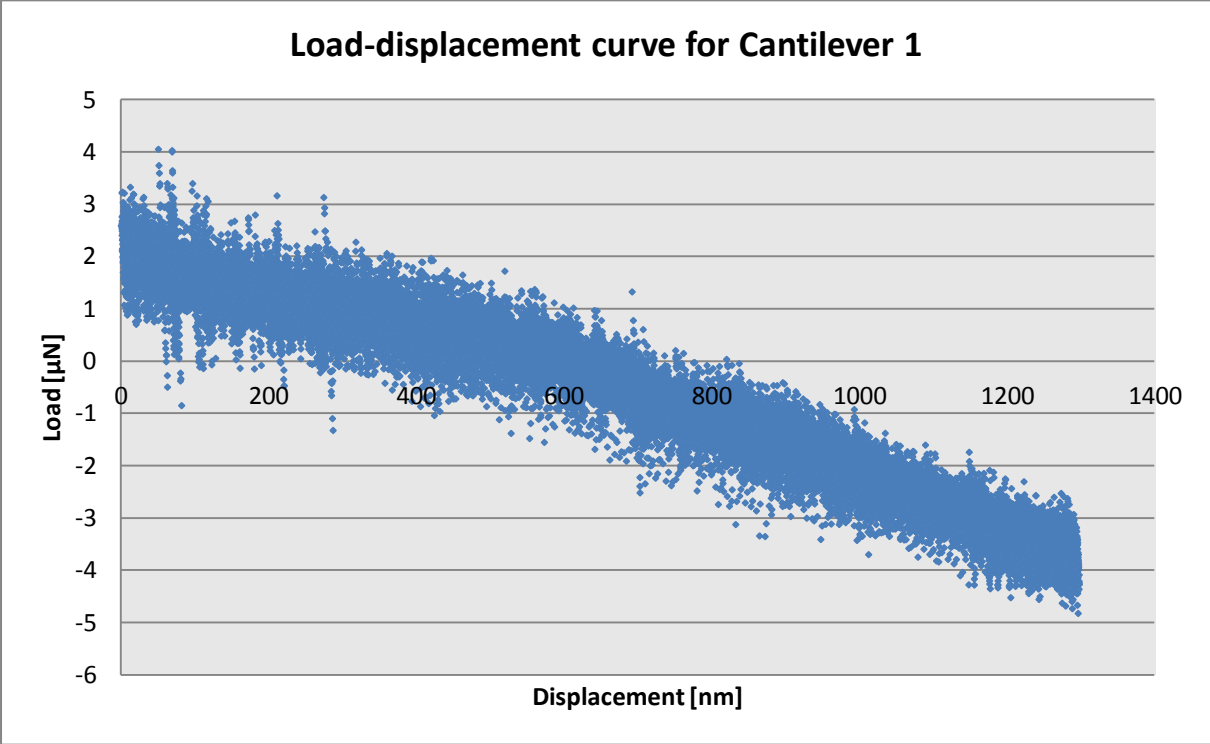
Figure A 14: Load-displacement curve for Cantilever 1
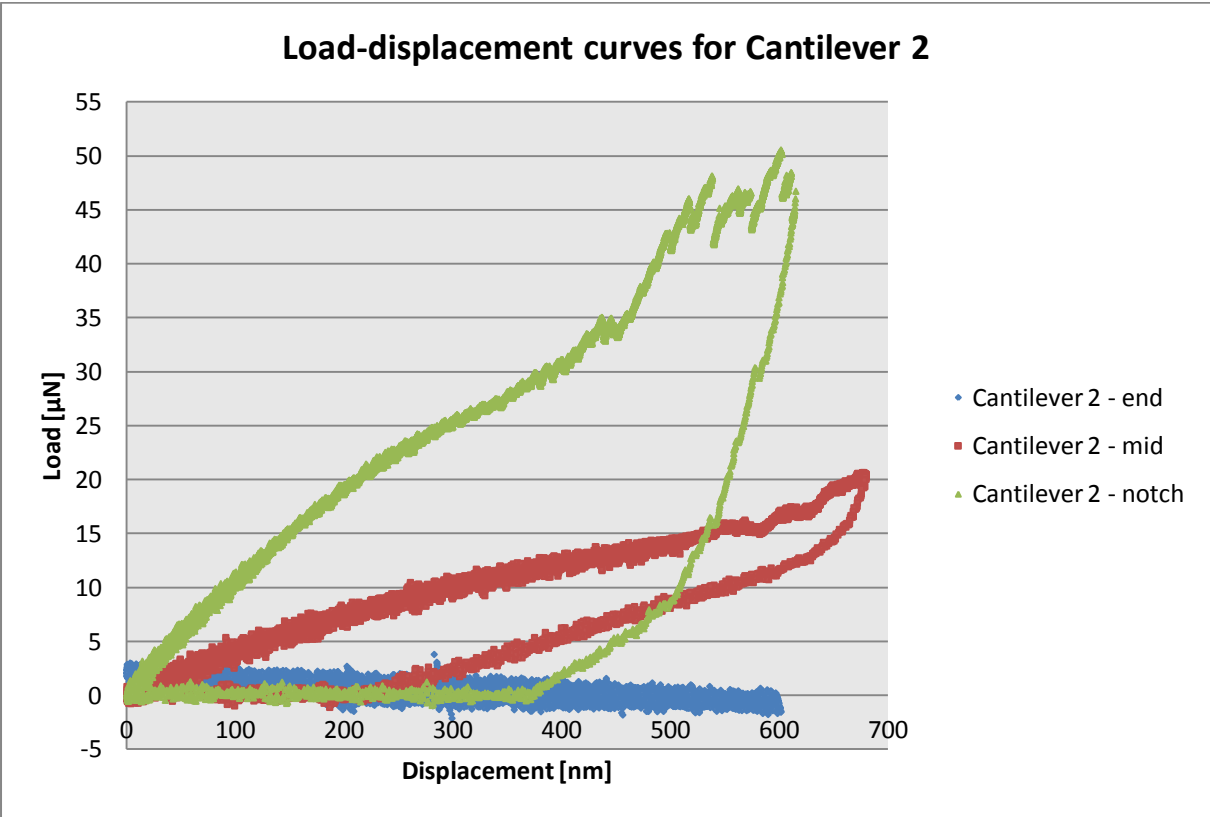
Figure A 15: Load-displacement curves for Cantilever 2.
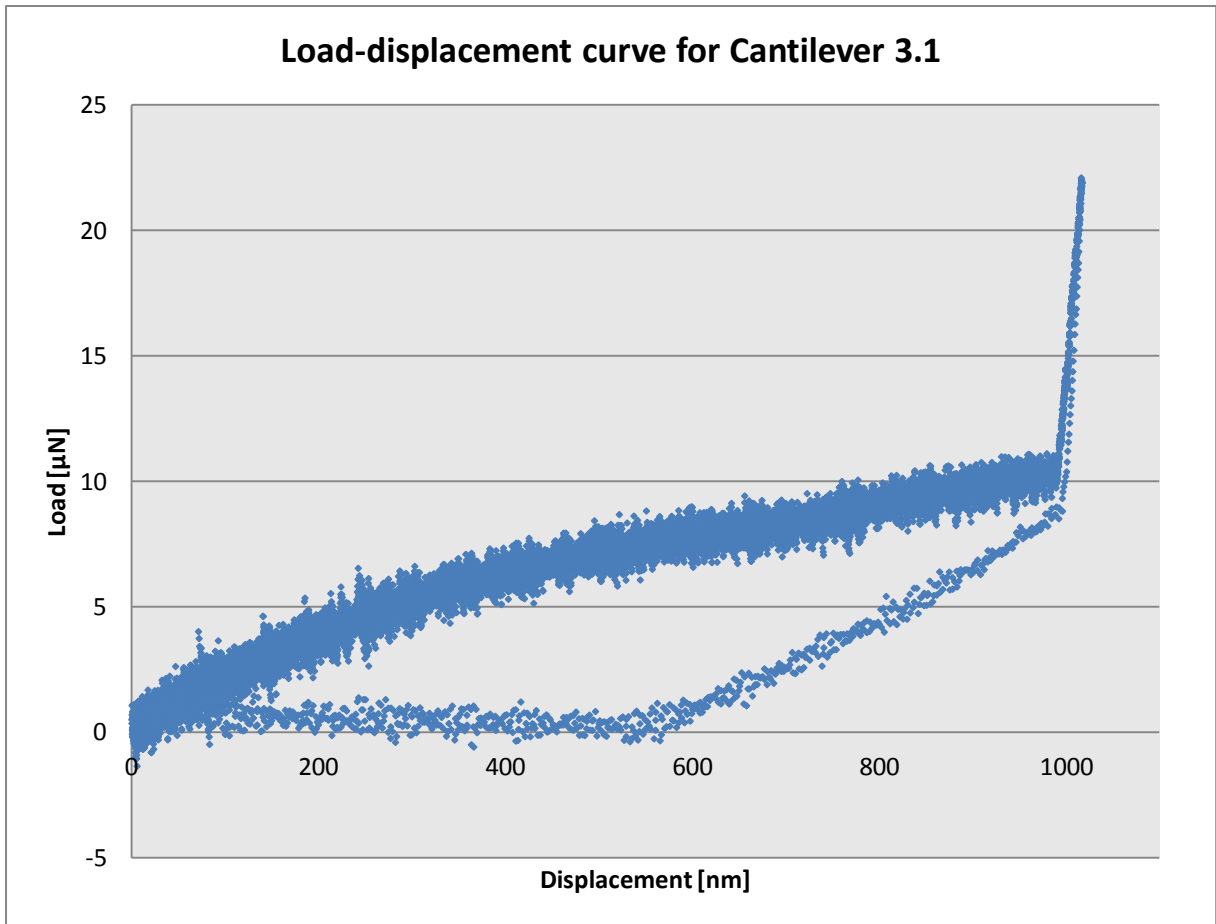
Figure A 16: Load-displacement curve for Cantilever 3.1

E.   Effect of the Q-parameter and logging rate
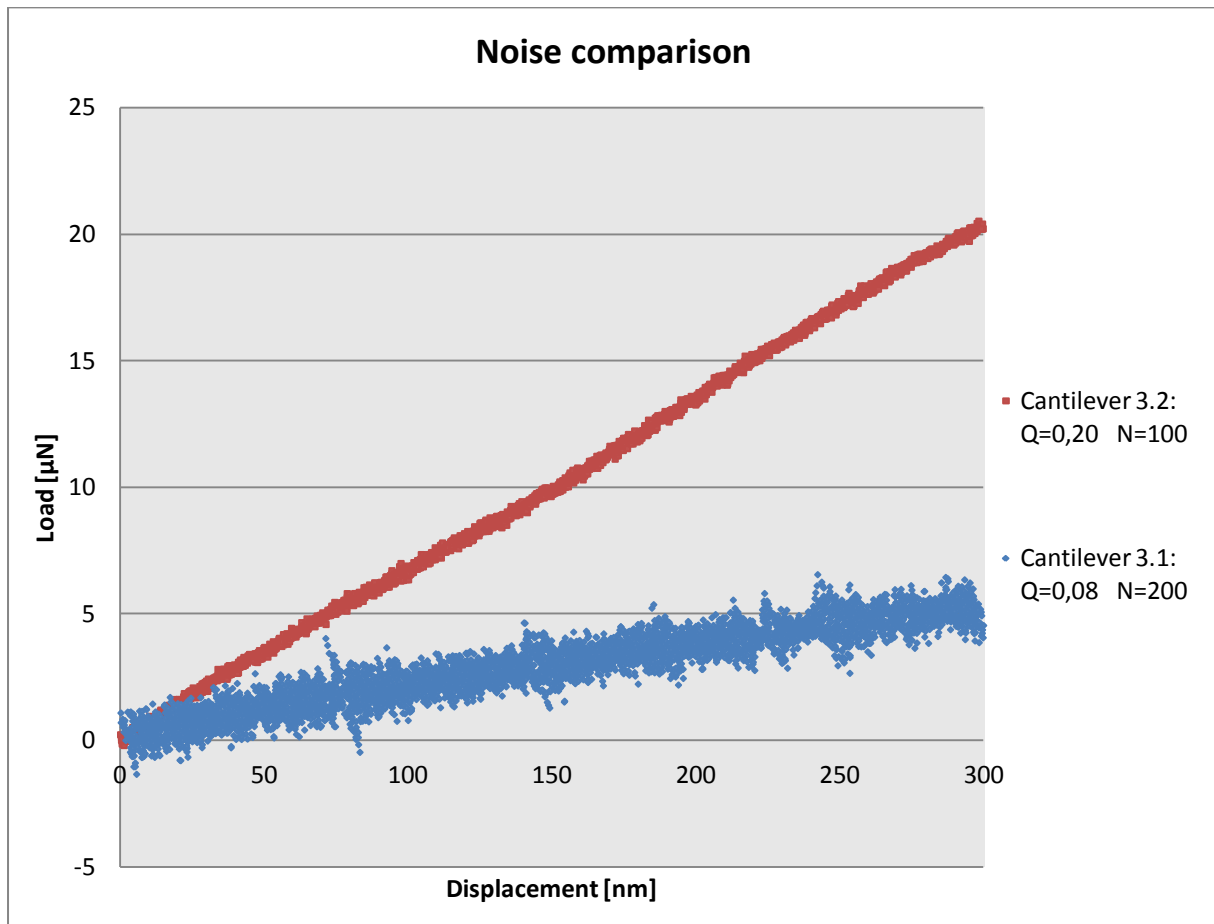
Figure A 17: Comparison between the different parameters used during the indentation tests.

As seen from Figure A 17, the reduced logging rate, N and the increased Q-parameter seem to greatly reduce the noise. This may also be a consequence of the greater stiffness observed during the Cantilever 3.2 indentation test, but the data points have less spread in general. For instance, the deviating lines around the 80 nm displacement was not observed during the second test and is most likely caused by the increase in the Q-parameter as it reduces the vibrations of the indentation tip.

Another contributing factor is that the reduced logging rate means that less deviating points get recorded and as such, the spread in the data points per time increment will be reduced.

F.   Additional SEM images of the fractured surface
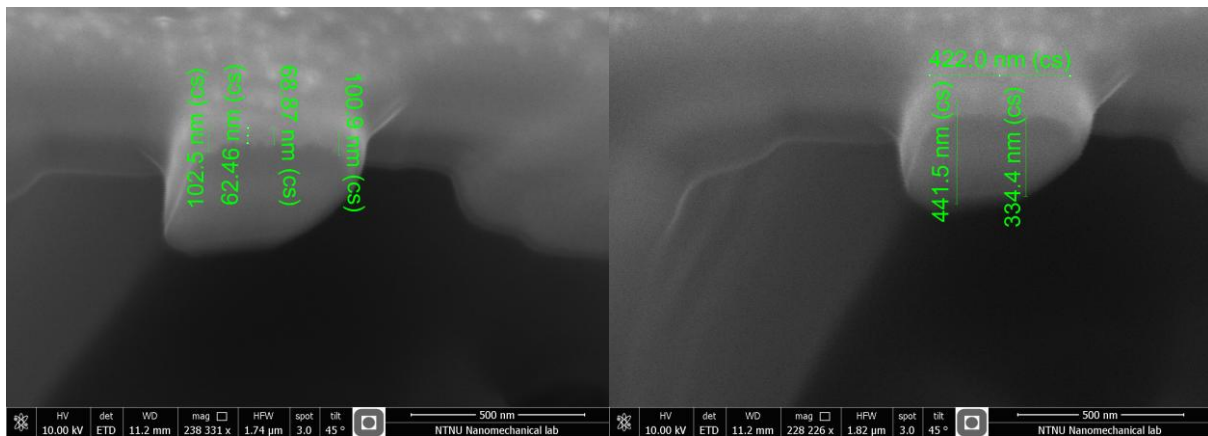

Figure A 18: Dimensions measured during the analysis of the fractured surface. These were used during the creation of the FE-model of the cantilever, as well as measurements collected with ImageJ.
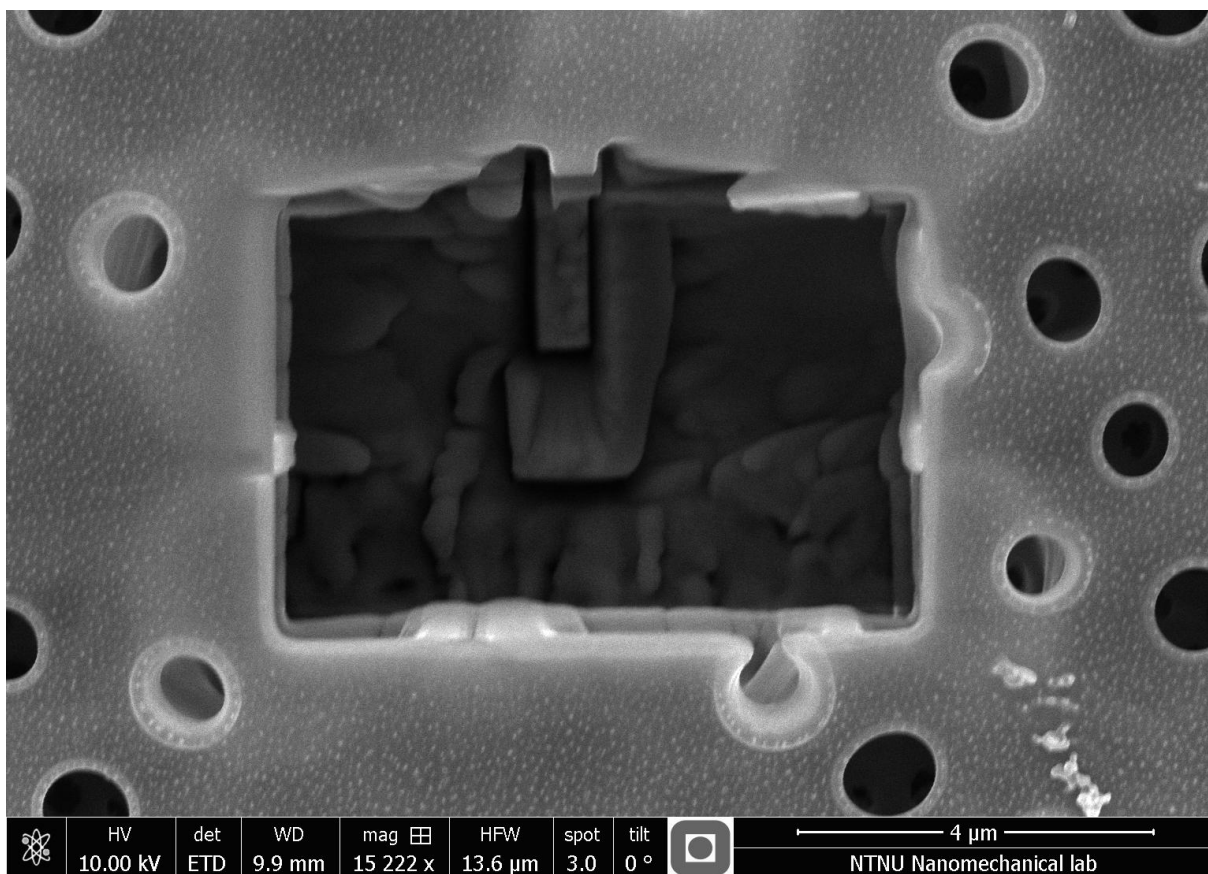

Figure A 19: The remains of the cantilever and the crater, as seen from above. The other end of the fractured cantilever could not be located.
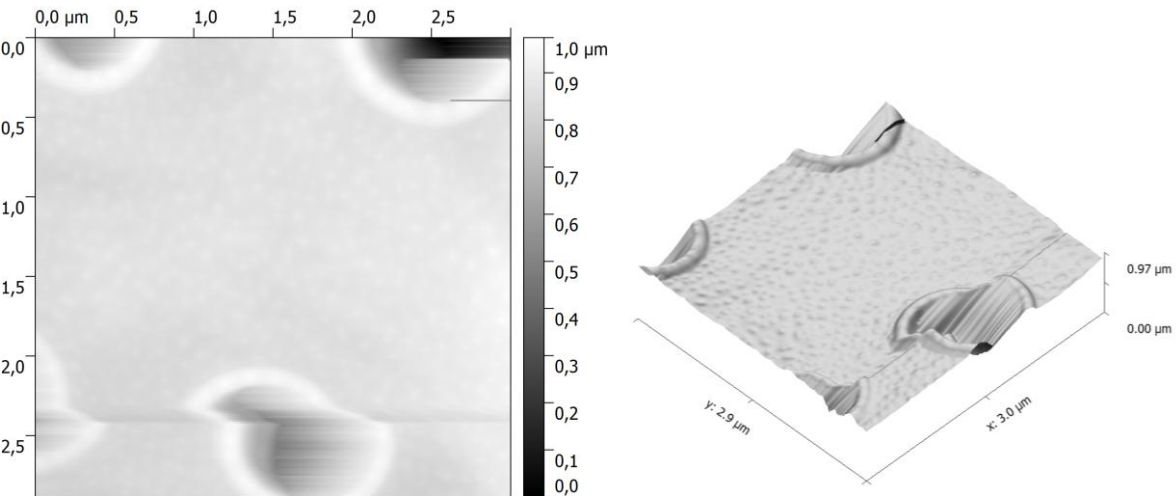
G.   Results from the AFM study

Figure A 20: The initial scan of the foramen surface, with corresponding 3D image.
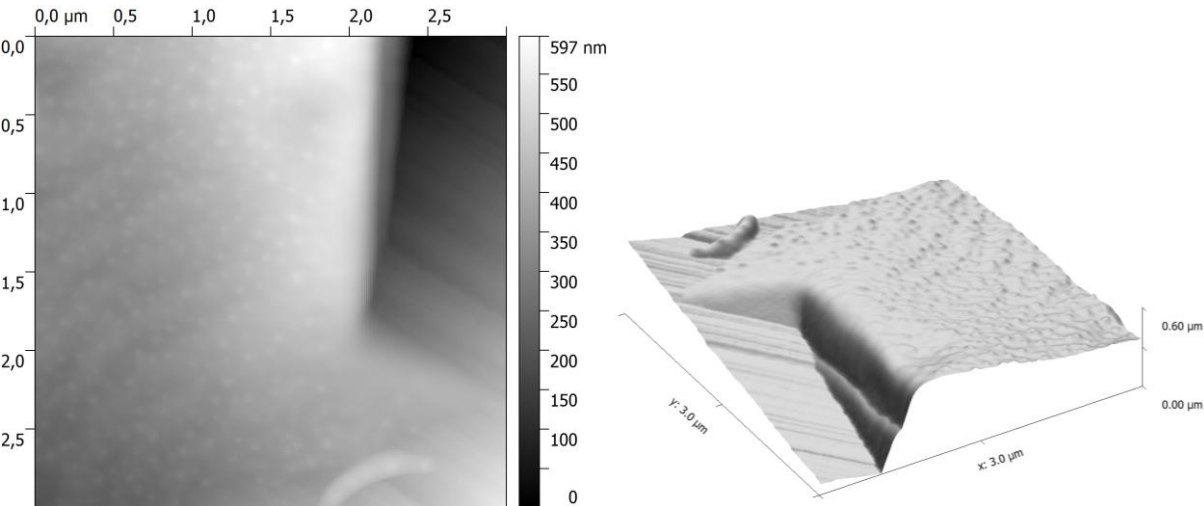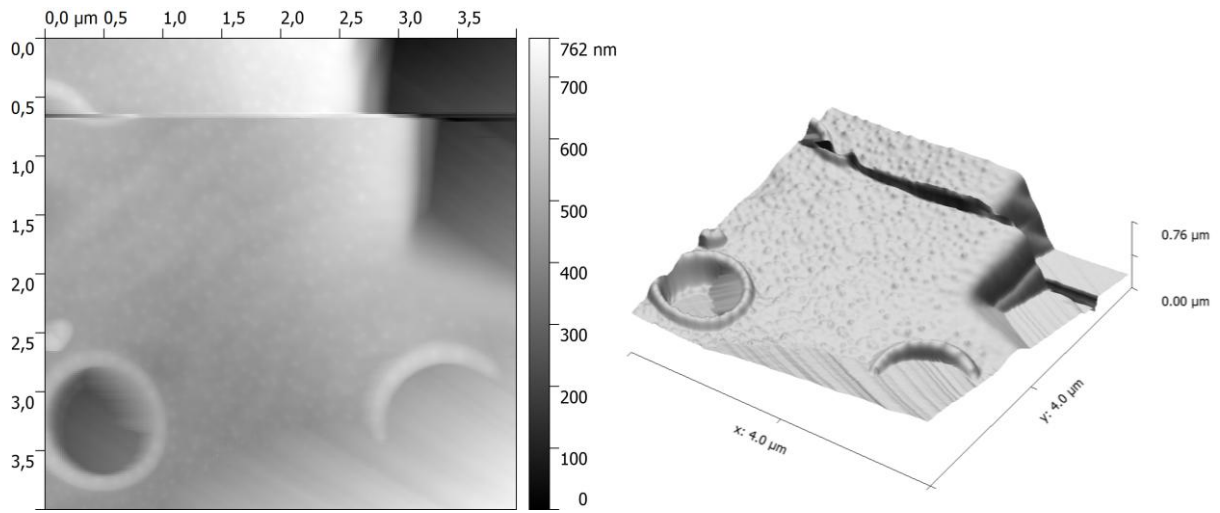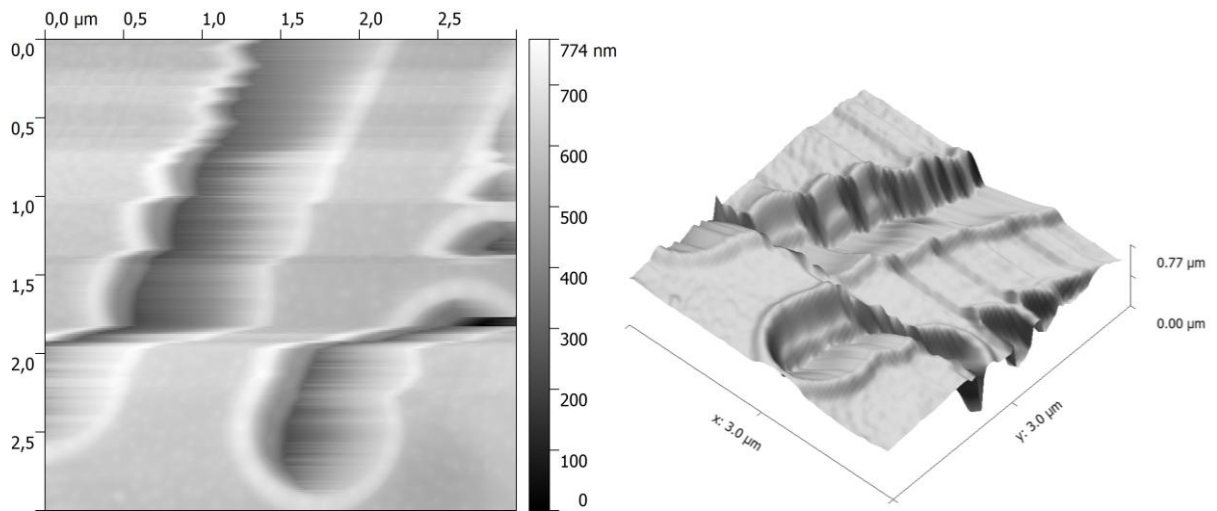

Figure A 21: The following scan when the crater was located, with corresponding 3D image.

Figure A 22: Another attempt at locating the cantilever, with corresponding 3D image.

Figure A 23: The tip appears to "dragging" the foramen hole along with the scan, with corresponding 3D image.

H. Risk assessment

A copy of the risk assessment report has been uploaded to DAIM.